EXPERIMENTAL SEISMIC SURVEYS OF THE TRANS-HUDSON OROGEN

A Thesis Submitted to the College of

Graduate Studies and Research

in Partial Fulfillment of the Requirements

for the Degree of Doctor of Philosophy

in the Department of Geological Sciences

University of Saskatchewan

Saskatoon

By

Sandor Bezdan

Spring 1998

PERMISSION TO USE

In presenting this thesis in partial fulfillment of the requirements for a Postgraduate degree from the University of Saskatchewan, I agree that the Libraries of this University may make it freely available for inspection. I further agree that permission for copying of this thesis in any manner, in whole or in part, for scholarly purposes may be granted by the professor or professors who supervised my thesis work or, in their absence, by the Head of the Department or the Dean of the College in which my thesis work was done. It is understood that any copying or publication or use of this thesis or parts thereof for financial gain shall not be allowed without my written permission. It is also understood that due recognition shall be given to me and to the University of Saskatchewan in any scholarly use which may be made of any material in my thesis.

Requests for permission to copy or to make other use of material in this thesis in whole or part should be addressed to:

Head of the Department of Geological Sciences
University of Saskatchewan
114 Science Place
Saskatoon, Saskatchewan
S7N 5E2 CANADA

ABSTRACT

Two experimental seismic surveys were collected in the 1991 LITHOPROBE Trans-Hudson Orogen (THO) data acquisition program. The purpose of the coincident dynamite and vibroseis reflection surveys was to compare crustal images obtained using high-fold low-energy and low-fold high-energy sources. On single-fold field records, signal amplitudes from explosive sources are consistently 50 dB higher than on the corresponding vibroseis records. The vibroseis final stack exhibits better defined upper-crustal reflectivity due primarily to the higher fold. However, at lower-crustal and Moho levels, the dynamite data provides images which are equal or superior to those obtained from the vibroseis data. The dynamite source not only allowed deeper signal penetration but also succeeded in mapping of a number of subcrustal reflections not identified in previous vibroseis data. These new seismic images indicate that the crustal root is not a simple depression on the upper-mantle as was inferred initially but a broad (3 s) zone of reflectivity that dips west and extends more than 10 km below the younger regional Moho. Moreover, the dynamite data also indicates that diffraction patterns, detected at lower crustal and Moho depths, have large apertures which permitted proper migration of these lower crustal events.

Four vibroseis expanding spread profiles (ESP) were also acquired during the data acquisition program to obtain more detailed and accurate velocity structure. These profiles, with a maximum offset of 18 km, were centered on areas where prominent crustal reflectivity was detected by the regional vibroseis survey. The small source stepout distance (100 m) generated high-fold (>30) data.

Extensive modeling was carried out to estimate the offset range within which each traveltime approximation and velocity analysis technique may be implemented. The results reveal that velocity estimation becomes more robust and accurate when crustal seismic surveys utilize longer offsets than commonly used. These larger source-receiver separations, however, must be generally limited to offset/depth ratios not exceeding 1.5 when conventional velocity analysis techniques, based on the hyperbolic moveout assumptions, are implemented. Besides the semblance method, two velocity estimators adapted to crustal studies, namely the covariance and the τ - p techniques, were tried. The former yielded the highest resolution followed by the semblance and the τ - p methods. Resolution of the semblance estimator for a maximum offset of 36 km is equal to that of the covariance method with a corresponding offset of 18 km for mid-crustal reflectors.

The advantages provided by the long-offset data acquisition include increased S/N ratio and a greater number of traces with sufficiently large moveouts which improved velocity resolution, especially below mid-crustal depths. To achieve similar advantages in a regional crustal reflection survey would require the adoption of longer spread lengths than those presently implemented in standard data acquisition procedures.

ACKNOWLEDGMENT

I would like to express my deepest gratitude to my thesis supervisor, Professor Zoli Hajnal, for his guidance, encouragement, support, and especially, patience. He was always available for consultation and provided excellent work environment at every level.

I also would like to thank my advisory committee members, Professors J.F. Basinger, D.J. Gendzwill, J. Merriam, K.V. Paulson, G.J. Sofko, and M.R. Stauffer, for their advice during many stages of the study and for their critical comments on the thesis.

Dr. A. Prugger helped to motivate me at critical times and reviewed the first draft for which I am extremely grateful. I am also indebted to Drs. B. Pandit and B. Carr for numerous suggestions related to data processing. I thank B. Nemeth and B. Reilkoff for assistance in both software and hardware aspects of the project. I also would like to acknowledge my fellow graduate students, C. Hooge, R. Francese, P. Redly, L. Ruo, and D. Schmidt, for discussing various geological/geophysical and other topics.

This research project was partly funded by LITHOPROBE and the University of Saskatchewan Graduate Scholarship.

TABLE OF CONTENTS

LIST OF FIGURES

LIST OF TABLES

LIST OF ABBREVEATIONS

AGC	Automatic Gain Control
CI	Contour Interval
CMP	Common Midpoint
COCORP	Consortium for Continental Reflection Profiling
COS	Common Offset Stack
CRP	Common Reflection Point
DNMO	Differential Normal Moveout
DMO	Dip Moveout
ESP	Expanding Spread Profiles
LGL	Log-generalized Likelihood ratio
NACP	North American Central Plains
NMO	Normal Moveout
S/N	Signal to Noise ratio
THO	Trans-Hudson Orogen
TWT	Two-Way Traveltime
X/Z	Offset to Depth ratio

CHAPTER 1

INTRODUCTION

1.1 Outline of thesis

In essence, the contents of the thesis may be described as follows. In Chapter 1 a brief overview of the geological and geophysical settings in the area under study is given. In the same chapter, a rationale for this study is put forward in the context of 1991 LITHOPROBE Trans-Hudson Orogen seismic experiment. The acquisition and processing of the experimental seismic survey data are fully described in Chapter 2. The comparative synthesis of the regional vibroseis and the dynamite data is presented in Chapter 3. The new discovery of subcrustal reflectivity zones on the dynamite based section is described here. Descriptions of the mathematical foundations and techniques developed and used to extract velocity information from reflection seismic data are given in Chapter 4. This chapter thus serves as a technical introduction for the subsequent chapters. The velocity analysis methods adapted to crustal studies are elaborated in Chapter 5. This chapter is exclusively dedicated to numerical modeling to establish optimum offset range in view of the resulting errors and resolutions of the estimated parameters by the different techniques. The results of velocity analysis of the expanding spread profiles (ESP) are described in Chapter 6. Results of the

interpretation of the ESP data compared to the regional vibroseis data are presented in second part of this chapter. Concluding remarks are given in Chapter 7.

1.2 Geological setting

The Paleoproterozoic Trans-Hudson Orogen (THO), one of the most recently defined major orogenic belts in North America (Hoffman, 1989; Lewry and Stauffer, 1990), extends from South Dakota through to the exposed Shield in Saskatchewan-Manitoba and across Hudson Bay to northern Quebec; branches may continue through Labrador, central Greenland and even Scandinavia (Fig. 1.1). The orogen is part of a greater "Pan-American" Early/Middle Proterozoic system whose evolution involved assembly of dispersed Archean microcontinents and accreted juvenile Early Proterozoic terranes during this major episode of North American continental assembly. The THO represents a continent-continent collision with a collage of oceanic rocks sandwiched between the Archean Rae-Hearne and Superior cratons. The orogenic segment exposed in northern Saskatchewan and Manitoba (Fig. 1.2) is composed of four major lithotectonic domains (Lewry, 1981; Lewry and Collerson, 1990):

(1) The Churchill-Superior Boundary Zone is a narrow southeastern ensialic foreland zone bordering Superior craton, which is segmented into the Thompson belt, Split Lake block and Fox River belt. Together these units form a dogleg extending from the southwest to east along the edge of the Superior craton. Petrochemistry of volcanic rocks in this zone suggests that these units, and associated metasediments, formed in a rift setting (Baragar and Scoates, 1981).

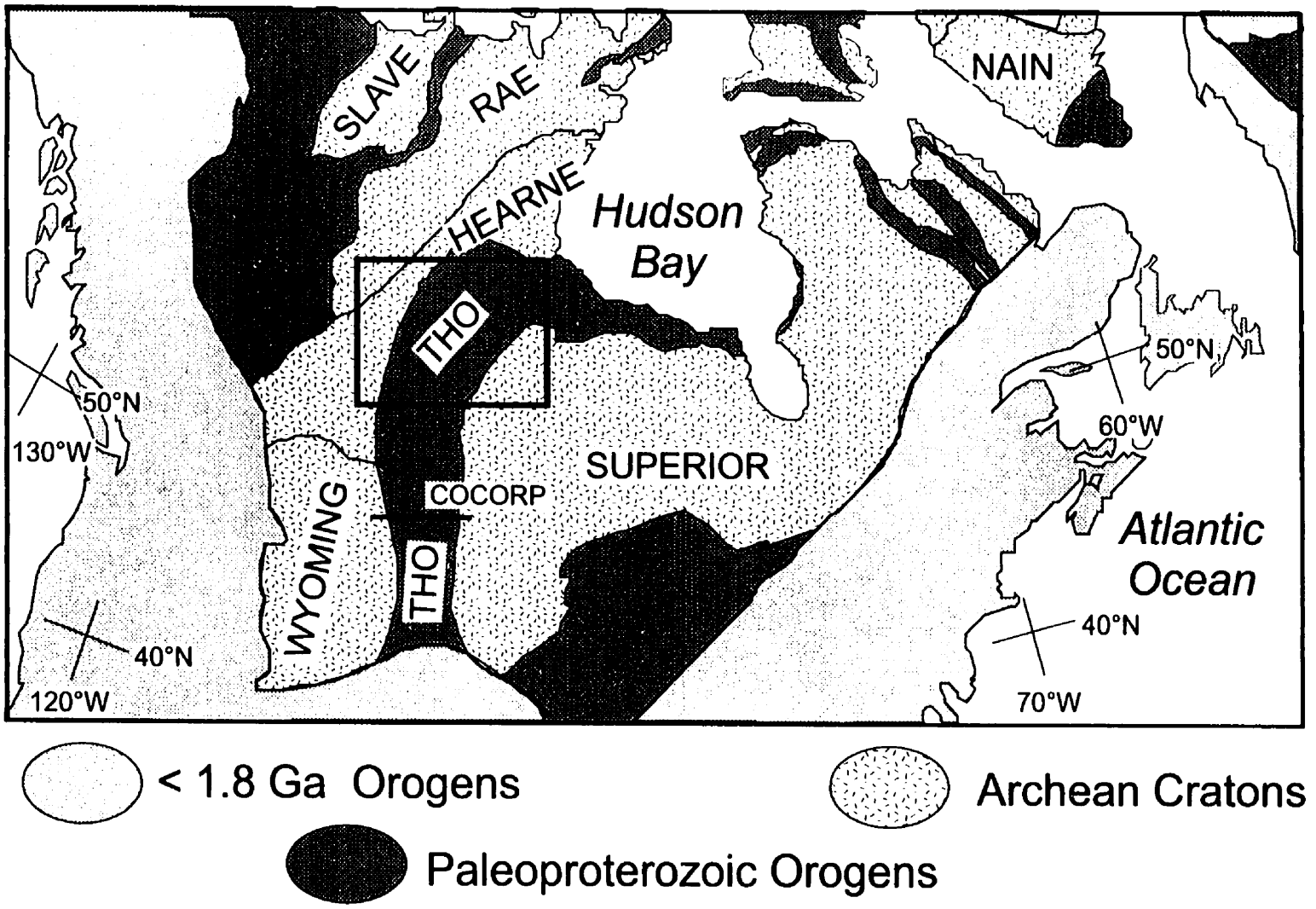

Fig. 1.1 Geological domains of North America. Box indicates the area investigated by the LITHOPROBE Trans-Hudson Orogen Transect. Black line marks the location of COCORP seismic reflection survey.

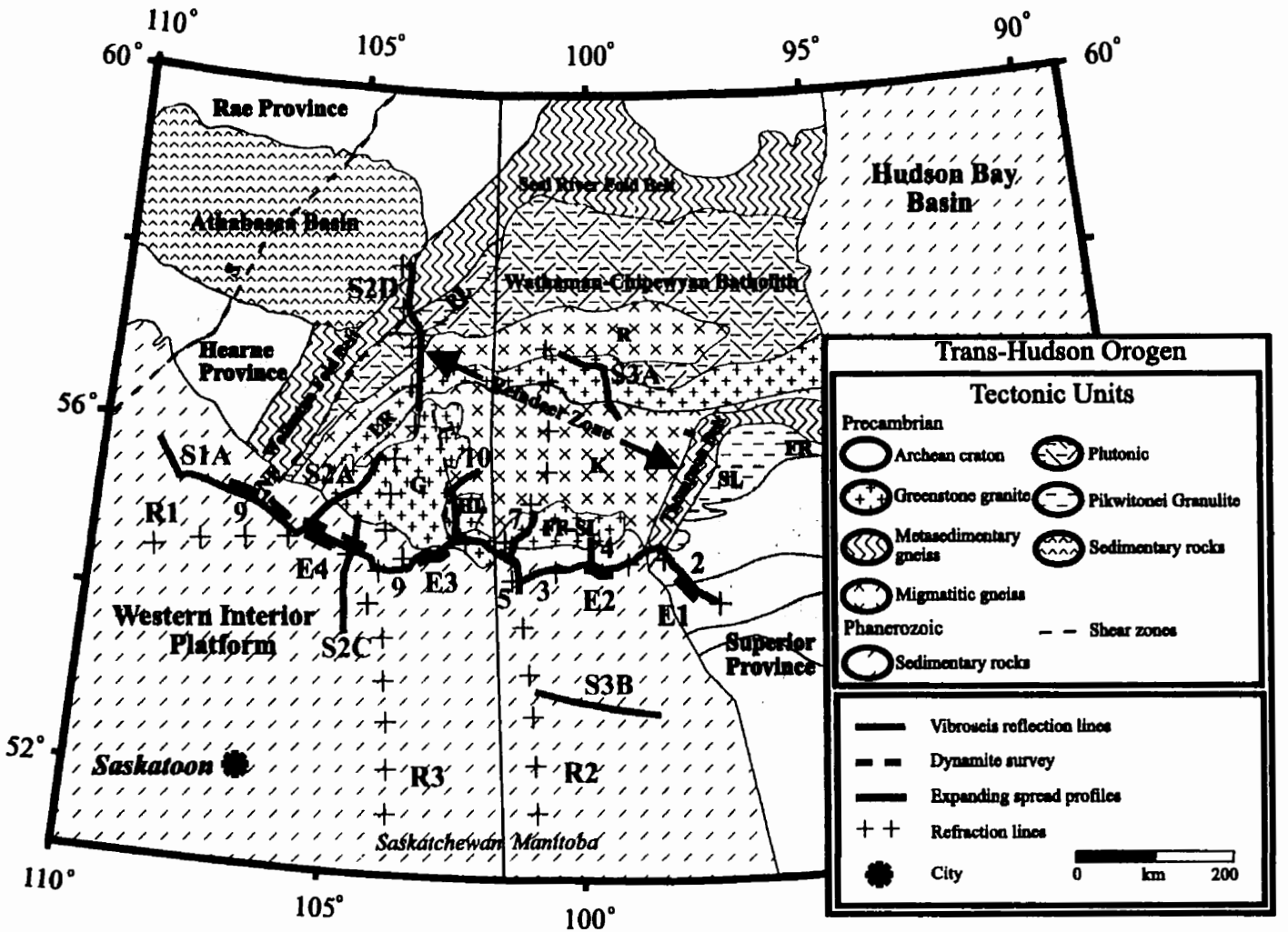

Fig. 1.2 Geological map of the Trans-Hudson Orogen showing the location of seismic lines. R: Rottenstone domain; LR: La Ronge belt; PL: Peter Lake domain; G: Glennie domain; HL: Hanson Lake block; K: Kisseynew domain; FF-SL: Flin Flon-Snow domain; SL: Split Lake block; FR: Fox River belt; S: Snowbird tectonic zone; NF: Needle Falls shear zone; T: Tabbernor shear zone.

(2) The internal Reindeer Zone (Stauffer, 1984) is a 400 km-wide collage of Early Proterozoic (ca. 1.9 to 1.8 Ga) arc volcanics, plutons, volcanogenic sediments and younger molasse, which is divisible into several lithostructural domains. Geochemical and Nd and Pb isotopic data indicate that most of the rocks evolved in an oceanic-to-transitional, subduction-related arc setting, with increasing influence of Archean crustal components to the northwest. The Early Proterozoic arc terranes were severely deformed and are preserved as refolded nappes and imbricate thrust sheets. The Flin Flon-Snow Lake domain, for example, is interpreted as an imbricated thrust wedge overthrust by higher grade Kisseynew gneisses and carried on a lower detachment zone (Lewry et al., 1990). In total, Lewry et al. (1990) suggest that the juvenile rocks of the internal zone are entirely allochthonous and were tectonically emplaced across reworked Archean lower plate extensions of Superior craton.

(3) An Andean-type continental margin magmatic arc, represented by the Wathaman-Chipewyan batholith, was emplaced at about 1855 Ma (Van Schmus et al., 1987). This mostly granite, granodioritic, calc-alkaline plutonic complex is situated between reworked Archean continental rocks to the northwest and accreted arc terranes to the southeast. In Saskatchewan, its northwest margin is defined by the Needle Falls-Parker Lake shear zone, a major crustal break with oblique, east-side-up dextral displacement.

(4) A complexly deformed northwestern hinterland zone incorporates the Peter Lake domain, Wollaston and Seal River fold belts and the Rae-Hearne Province (Hoffman, 1989). The Peter Lake domain is characterized by abundant mafic-ultramafic plutons. Felsic gneisses/granitoids comprising most of the domain include Archean basement predating the mafic plutons and later Hudsonian granites. In the Wollaston and Seal River domains, highly deformed and metamorphosed Early Proterozoic rifted margin, miogeoclinal and foredeep sediments are complexly interfolded with Archean basement and intruded locally by ca. 1855 Ma synorogenic and 1760 Ma anorogenic granites. The western part of the Archean Hearne Province appears to have undergone Proterozoic multiphase deformation and high-grade reworking. Sm-Nd data yield Archean crustal residence ages of over 3.0 Ga, whereas nothing older than 2.8 Ga has been obtained from the Peter Lake domain (Bickford et al., 1990).

The history of plate convergence, collision, and subsequent intracontinental deformation in the THO spans 1.9 to 1.7 Ga. In summary, the rocks of the Reindeer Zone were accreted to the Rae-Hearne cratonic margin during successive arc-continent collisions prior to the terminal collision with the Superior craton at ca. 1.8 Ga. The more detailed information concerning the tectonostratigraphy, structure and geochronology of the tectonic units are summarized by Lewry and Stauffer (1990). One important feature is that previous workers (e.g. Green et al., 1985; Lewry et al., 1990) suggested 'thin-skinned' imbrication of Paleoproterozoic rocks against the

cratonic margins and predicted a continuation of Archean continental crust beneath the internal zone of the orogen.

1.3 Previous geophysical studies

Deep crustal seismic reflection data in the THO region consist of a few short reconnaissance profiles across the Superior margin of the craton (Green, 1981; Green et al., 1985). They indicate a consistent west-dipping pattern of reflections on the west side of the Churchill-Superior boundary zone, where refraction results also indicate the presence of a low-velocity zone.

Prior refraction work pertinent to the THO was conducted across the subsurface southern extension of the orogen, rather than the exposed part of it (e.g. Hajnal et al., 1984; Kanasewich et al., 1987; Morel-à-l'Huissier et al., 1987). The data were acquired with an older acquisition methodology which did not provide the degree of resolution available with current methods. In general, the upper crust is laterally heterogeneous with P-wave velocities varying from 5.2 to 6.5 km/s. Some indications of low velocity zones were found in the upper to mid-crustal regions in the southern segment of the Reindeer zone. Upper crustal velocities appear to change near projected tectonic boundaries. All southern extensions of the lithotectonic zones have a distinctive lower crustal discontinuity across which the P-wave velocity increases abruptly to values >7 km/s. The depth of the crust-mantle boundary varies from a minimum of 37 km, at the western margin of the Superior craton, to 50 km under the central portion of the Williston Basin.

Green et al. (1985) and Klasner and King (1986) analyzed aeromagnetic and gravity data across, and adjacent to the Williston Basin. The gravity compilation was subsequently extended by Thomas et al. (1987). Continuity and consistency of patterns on both maps permit extrapolation of Precambrian domains and structural elements beneath Phanerozoic cover into the central parts of the North American craton. A new detailed gravity survey, with station spacing of 1-2 km, was completed along the 1991 LITHOPROBE seismic reflection lines. The gravity data show a number of associations with the local surface geology. For example, a positive anomaly is associated with the Rottenstone domain along the Needle Falls shear zone, and the Sturgeon Weir thrust at the eastern boundary of the Hanson Lake block coincides with a gravity low. Some of the largest gravity anomalies in the Canadian Shield are associated with the Churchill-Superior boundary zone; a large negative anomaly straddles the boundary and overlies the Kisseynew gneiss and Thompson belts.

Discovery of a major kimberlite field above subsurface southern continuation of the Glennie domain suggested anomalous lithospheric conditions beneath internal lithotectonic domains of the orogen (Collerson et al., 1990). The refraction survey program was altered in anticipation of these anomalous results: source charge-sizes were increased, spacing between shot locations were redesigned, and profile lengths were extended.

A crustal-scale electrical conductor, the North American Central Plains (NACP), was recognized beneath Williston Basin (Alabi et al., 1975). A major LITHOPROBE EM investigation was planned to delineate the most northerly position NACP conductivity anomaly and to characterize the electrical conductivity structure of the

lithosphere. The NACP anomaly is the largest, most enigmatic continental-scale conductor yet delineated by electromagnetic induction studies. However, its precise location relative to lithotectonic elements of the exposed THO is ill defined.

Investigation carried out along THO Transect provides an important opportunity to correlate and compare seismic and other indirect geophysical data obtained in a region of good surface exposure with data previously obtained from southern extensions of the orogen beneath Phanerozoic cover. Through cooperation with COCORP (Consortium for Continental Reflection Profiling), interpretation of the Williston Basin deep seismic profiles from North Dakota and northeastern Montana are being correlated with data from the north (Fig. 1.1).

1.4 The 1991 Trans-Hudson Orogen seismic experiment

The THO Transect provides an opportunity to investigate the deep crustal properties, geometry, structural setting, and petrophysical characteristics of one of the best preserved and exposed Paleoproterozoic orogenic belts in the world. The broad objective is to understand better the tectonic development of this collisional zone and the geodynamic processes involved in its evolution by determining crustal structure and other lithospheric characteristics of its primary constituent components.

The first stage of LITHOPROBE's deep seismic reflection profiling of the THO was undertaken in the summer of 1991. As part of LITHOPROBE's Phase III THO Transect, this marked the beginning of the multi-disciplinary probing of the crust in northern Saskatchewan and Manitoba to study the origin of the continent. In total, >1000 km of near vertical incidence vibroseis reflection data were collected, traversing

the entire orogen and the margins of the bounding cratons (Fig. 1.2). In addition to the E-W trending main profile, reflection data were also acquired along cross lines running roughly perpendicular to the main transect in order to provide 3-D control. Simultaneously, with the acquisition of the regional reflection profiles, two special seismic experiments were conducted. In addition to the vibroseis data, the westernmost 200 km of line 9 was also surveyed utilizing explosive sources (Fig. 1.2). The purpose of this dual approach was to compare deep crustal images obtained using high-fold low-energy vibroseis and low-fold higher energy sources along the same survey line. The choice of the location for the dynamite survey was governed by two factors:

(1) earlier crustal models (Hajnal et al., 1984; Green et al., 1985) predicted crustal thickening westward which might not have been properly imaged by the limited 16-second recording time of the vibroseis survey, and

(2) the western flank of the THO is covered by a sufficient thickness of glacial till making shothole drilling economically feasible.

The second experiment consisted of acquisition of four expanding spread profiles (E1-E4 Fig. 1.2) designed to measure crustal velocities from the surface to the Moho in the various lithotectonic domains. The locations of the ESP studies were not determined before the start of the data acquisition program. They were based on the high crustal reflectivity areas identified during the regional survey. These innovative studies were conducted to complement the regular 2-D reflection profiling and were in

the nature of experiments to ascertain the feasibility of extending different seismic reflection techniques to crustal studies.

CHAPTER 2

SEISMIC DATA ACQUISITION AND PROCESSING

Investigation of the efficiency of vibroseis and explosive sources, as techniques of data acquisition in crustal seismology, still has global interest as indicated by several recent studies (e.g. Damotte and Bois, 1990; Valasek et al., 1991; Steer at al., 1996). Similarly, numerous ESP experiments are regularly executed to record specially designed longer offset data to reach a better insight about crustal velocity-depth variations and more comprehensive interval velocity resolution.

2.1 Data acquisition

2.1.1 Dynamite survey

The 1991 phase of the LITHOPROBE seismic data acquisition program included the standard regional vibroseis survey, an additional experimental dynamite based program along a segment of one profile and a set of four ESP spreads in different geological settings of the transect.

The acquisition parameters of the different deployments are listed in Table 2.1. Identical instrumentation and receiver arrays were used in all three surveys. Recording was accomplished with MDS-18 telemetry system by Enertec Geophysical Services of

Calgary. Anti-alias and 60 Hz notch filters were applied to the data during data acquisition. To eliminate unusually high noise levels the vibroseis survey used diversity stack (Sheriff, 1991, p. 87). The dynamite experiment was designed to be coincident with the major program. When the vibroseis survey reached a shothole location an additional recording was introduced in the data acquisition sequence by detonation of the explosive charge.

Table 2.1 Acquisition parameters

	Vibroseis	Expanding Spread	Dynamite
Energy source	4 Hemi-50 vibrators		50 kg Geogel
Source interval	100 m		600 m and 1500 m
Sweep	12-56 Hz linear		N/A
Number of sweeps	8		N/A
Receivers	Oyo 20D, 9 per group		
Station interval	50 m		
Number of stations	240		
Spread geometry	Asymmetric	End-on	Symmetric
Maximum offset	9 km	18 km	6 km
Record length	16 s		30 s
Sampling interval	4 ms		
Nominal fold	60	31-64	4-10

2.1.2 Expanding spread profiling technique

The ESP data were acquired during the normal recording of the regional reflection profiles. When the regular profiling encountered areas with prominent reflectivity, the

vibrators would move up to the appropriate ESP vibration point. After recording the one side of the ESP, the vibrators would then move back to continue the standard CMP profiling until the spread reached the appropriate location to record the opposite side of the ESP (Fig. 2.1). In case of E1 and E3 only one side of the ESP were collected. The THO experiment had a unique approach with its small source stepout distance (100 m). This configuration generated high-fold (>30) data which permits direct comparison with the regional profiles.

Figure 2.1 shows the source-receiver configuration (Musgrave, 1962) used in two of the ESP surveys. The energy source moves in one direction while the spread rolls back by the same amount in the opposite direction to ensure the same set of midpoints for each record. This acquisition scheme also permits the data to be processed in the CMP domain (Stoffa, et al., 1992) if the nominal fold is sufficiently high. This is in contrast to the low-fold wide-angle ESP (Fowler et al., 1989; DEKORP Research Group, 1990; Damotte and Bois, 1990; Wright et al., 1990; Minshull et al., 1991) wherein most of the data analysis is implemented in the composite shot gather domain. In these cases inversion of traveltime picks for refracted, reflected and diffracted phases is used to obtain a velocity model. Alternatively, a starting velocity model can be obtained by slant stacking the binned seismograms (Stoffa and Buhl, 1979), picking an envelope function in τ-p domain, and applying the τ-sum recursion scheme (Diebold and Stoffa, 1981).

The ESP acquisition geometry is very favorable for velocity analysis, since for a given reflector the events recorded at different offsets originate within a narrow subsurface zone assuming marginal structural disturbance. Consequently, wavefield

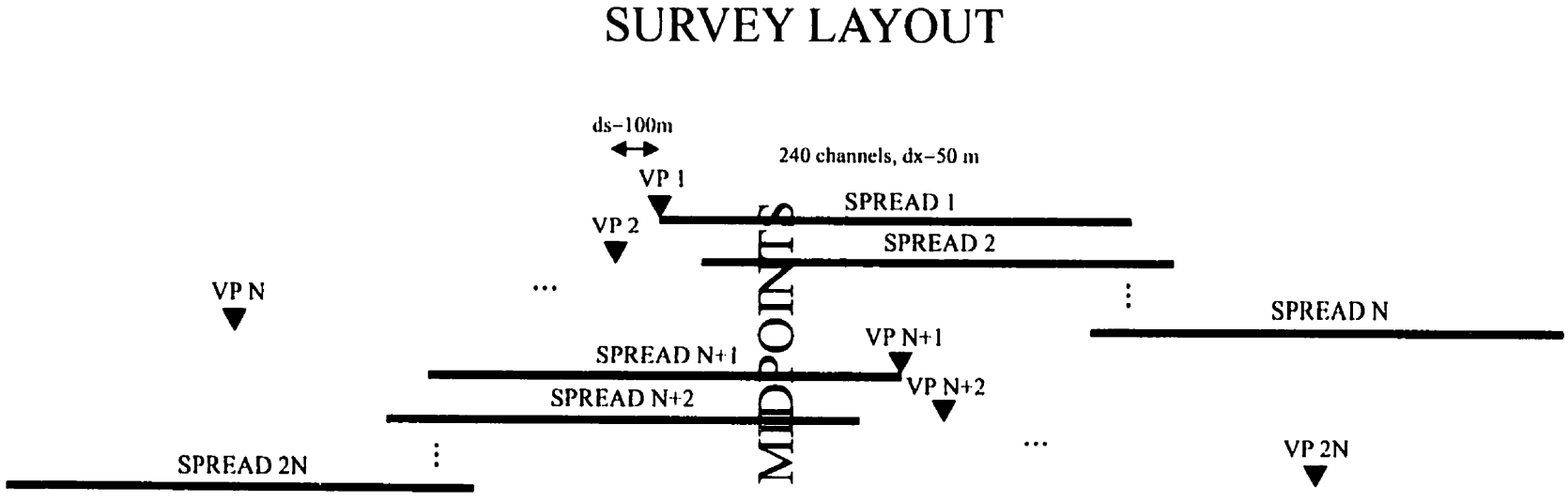

Fig. 2.1 Source-receiver locations for expanding spread profiling. The triangles denote vibration points and the corresponding spreads use the same numbering. N = the number of records in one survey direction.

distortions due to lateral inhomogeneities are minimized, and the reflection events are often clearly identifiable and continuous (Stoffa et al., 1992). In addition, the ray parameter averaging inherent in CMP data minimizes the effects of dip and lateral velocity variations (Diebold and Stoffa, 1981). The two-sided survey layout of these experimental profiles contributes to a better delineation of dipping and complex structures, and to a more reliable analysis of the errors in the velocity estimates. Furthermore, the larger offsets of the surveys permit recognition of undetected reflection phases, as source generated coherent noise patterns do not mask weak events, and generally the signal amplitudes increase with increasing angle of incidence. These types of data should also be more reliable for advanced amplitude-versus-offset analysis. Detailed and more accurate velocity structure, obtained in an ESP survey, will improve the performance of the migration process and thus leads to better images of complex tectonic domains.

2.2 Data quality

2.2.1 Dynamite versus vibroseis signals

Both energy sources provided high quality shot records (Figs. 2.2 and 2.3). Distinct reflections are clearly visible on both shot records in the zone from 2 s to 13 s. M1 marks a well-defined Moho reflection at ~13 s. A dipping subcrustal reflection event (L, Fig. 2.3) indicates excellent energy penetration for the explosive source. Vibroseis field data generally have better defined reflections than the equivalent dynamite records between 2 and 4 s. Below this zone, however, the quality of the explosive records is equal or superior to that of the vibroseis data. Some explosive records,

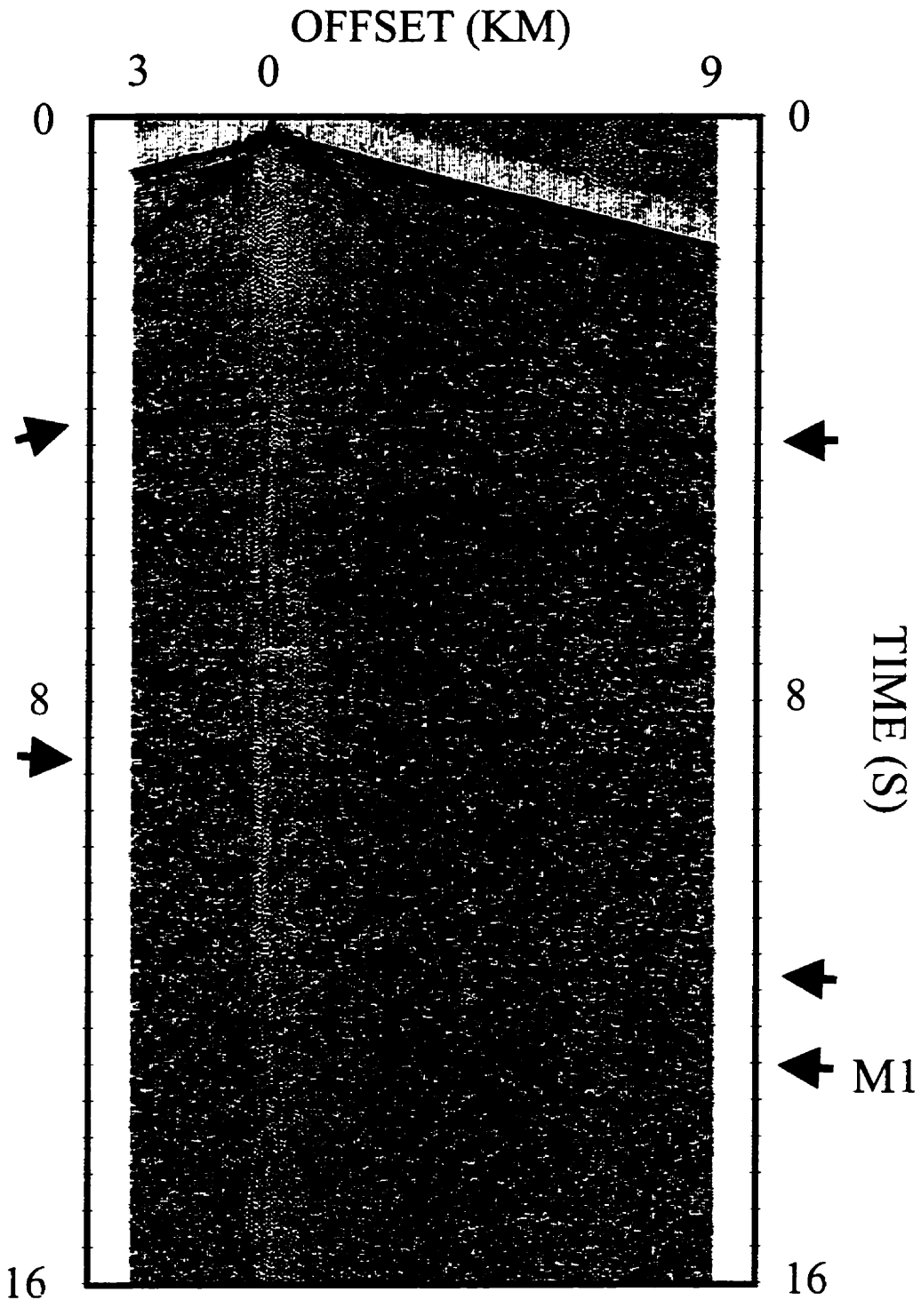

Fig. 2.2 Vibroseis field record with AGC applied.

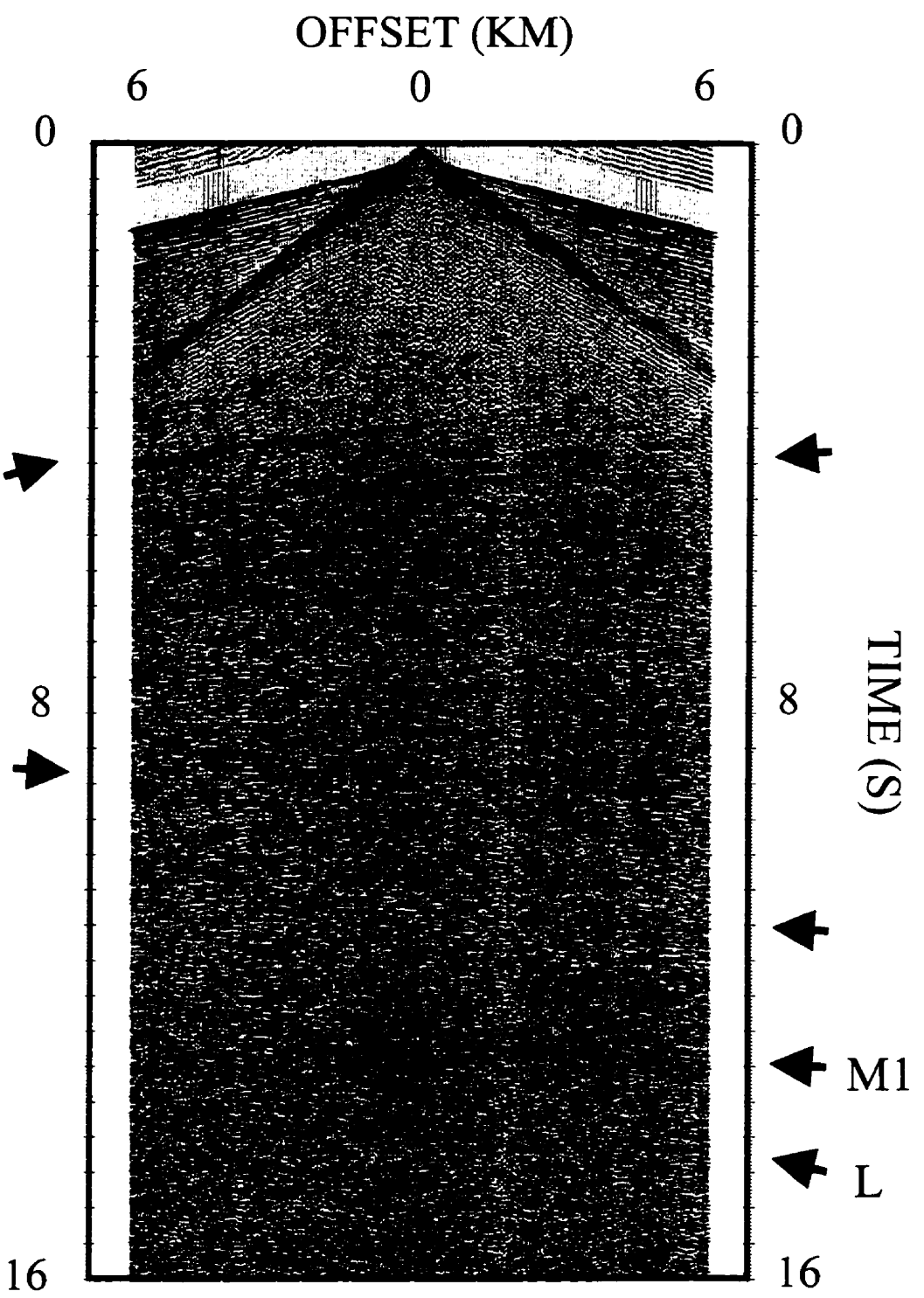

Fig. 2.3 Dynamite field record with bandpass filtering (8/12-56/60 Hz) and AGC applied.

however, were contaminated by strong ground-roll and air-wave coupled ground roll (Fig. 2.4). Throughout the THO survey, the ground roll is controlled by the overburden, or "weathering layer", which is largely composed of various glacial deposits. Ground roll tends to be strong where the overburden is thin and tends to be weak where the overburden is thick. Geophone arrays are designed to attenuate ground roll and to ensure against aliasing of seismic waves reflected from steep structures. The 50 m array length used in the surveys attenuates ground roll energy of wavelength ≤56.25 m. The ground roll velocities in the overburden are generally less than 700 m/s, and so the arrays largely cancelled out all ground roll energy with frequencies >12 Hz. Consequently, the ground roll posed a more serious problem for the explosive source since it effectively generated signals with frequencies lower than the cut-off frequency of the vibroseis source (Fig. 2.5).

In order to compare efficiency of the signal penetration generated by the two sources, amplitude decay curves were calculated from the data before stack. The signal penetration is limited because seismic energy decreases in both amplitude and frequency content as it propagates (due to absorption, scattering and wavefront spreading), at some point becoming too weak to be discerned above the prevailing noise. Signal penetration is a key issue for deep reflection seismology because the goal is to image structure as deep as possible. Insufficient signal penetration can cause a die-out of reflections that resembles a lack of reflectors. The amplitude decay calculation was implemented as follows. Five traces centered on the 3-km offset were summed together and root-mean-square amplitudes were calculated in 100-millisecond windows. The curves were then normalized relative to the ambient noise

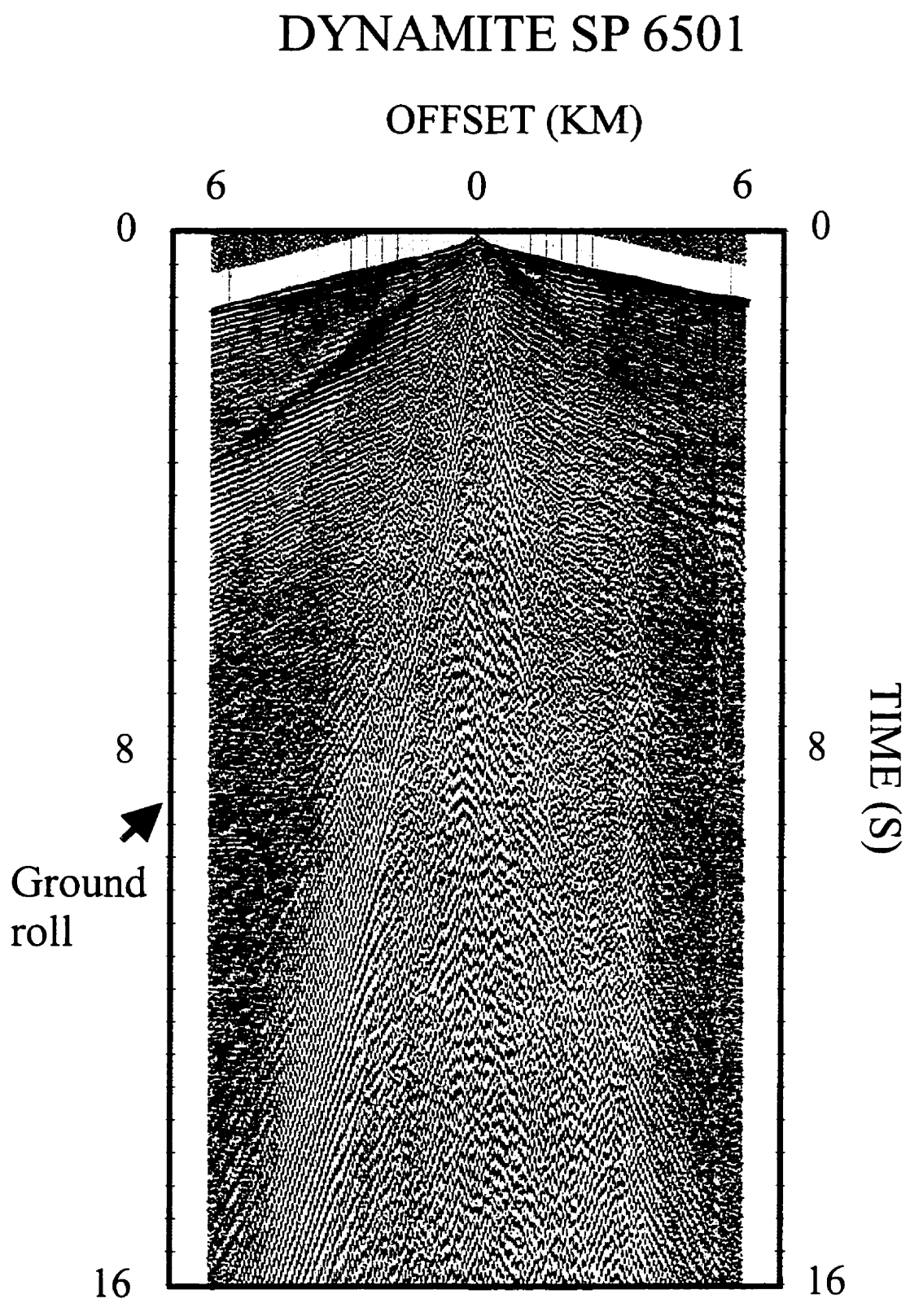

Fig. 2.4 Dynamite field record with AGC applied.

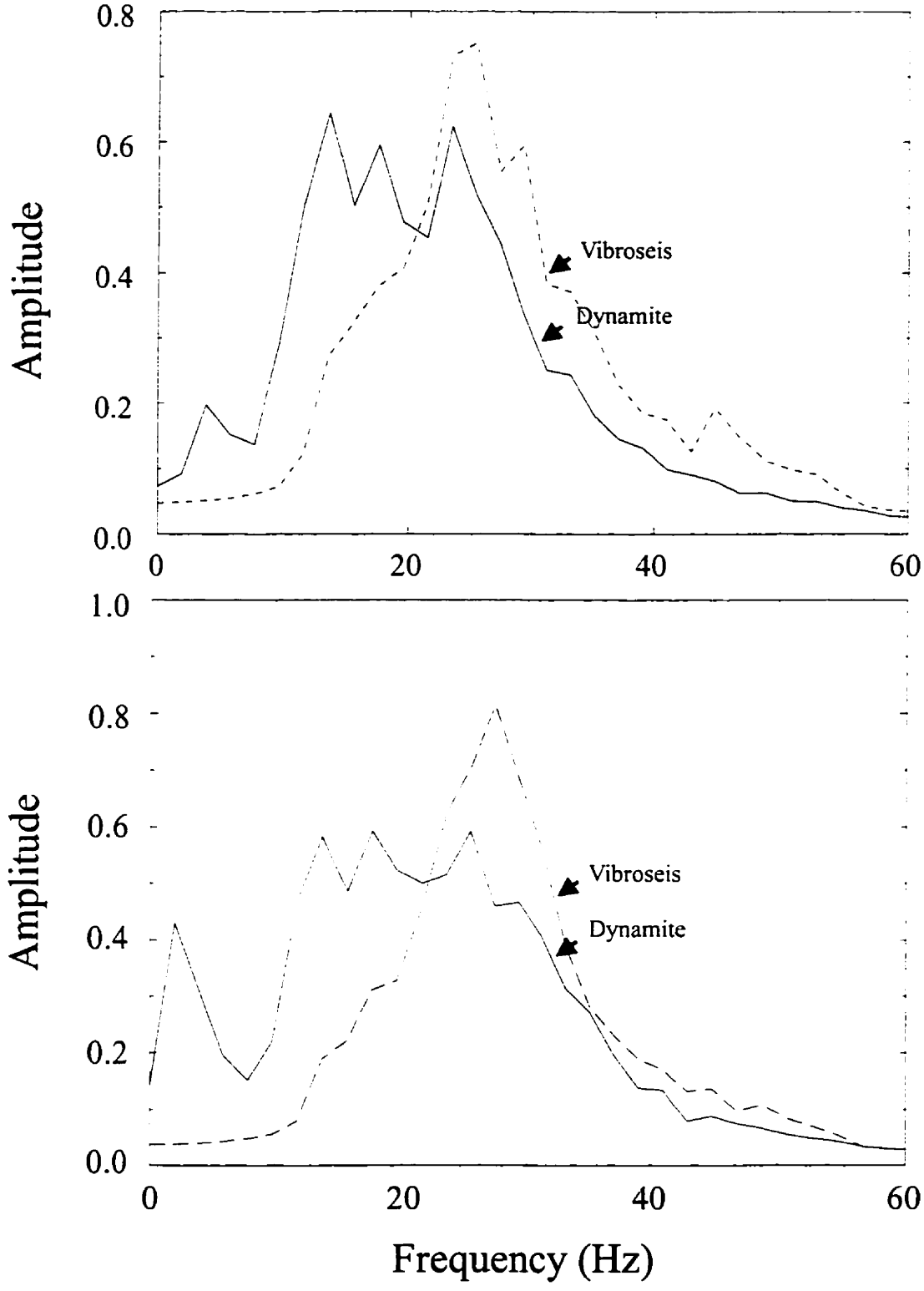

Fig. 2.5 Average amplitude spectra of field shot records in the time window (12.3-12.8 s) at 0.6 km (top) and 3 km (bottom) offsets.

level recorded prior to the first break. Figure 2.6 reveals that the amplitude level of the dynamite records is at least 50 dB higher than that of the vibroseis records. These results agree with similar amplitude relations established by other studies (e.g. Barnes, 1994; Steer et al., 1996). Characteristically, it is important to note that the amplitude of the THO vibroseis field records are near or just above the ambient noise level at 16 s while the dynamite records remain above ambient noise levels throughout the full recording length of 30 s.

Frequency content is arguably the most important of the acquisition parameters, because it determines the resolution. Ideally, the frequency content reflects that of the seismic source, but local variations in geology, noise and recording conditions cause significant differences in the final frequency content. The average frequency spectra of the two data sets at Moho level are displayed in Fig. 2.5. The explosive source generated signal appears to have broader bandwidth and stronger frequency content below 20 Hz than that of the vibroseis source. Even if some of these low frequencies can be attributed to ground roll components, they are extremely beneficial in imaging lower-crustal and subcrustal structures. The vertical resolution of the wavelets can be quantified by the Rayleigh resolution limit (Sheriff, 1991, p. 241). It is approximately 70 m at Moho levels:

$$\lambda / 4 = \frac{V}{4 f_D} \approx \frac{7000 m/s}{100 Hz} = 70 m \qquad (2.1)$$

where λ is wavelength, V is velocity and f_D is the dominant frequency.

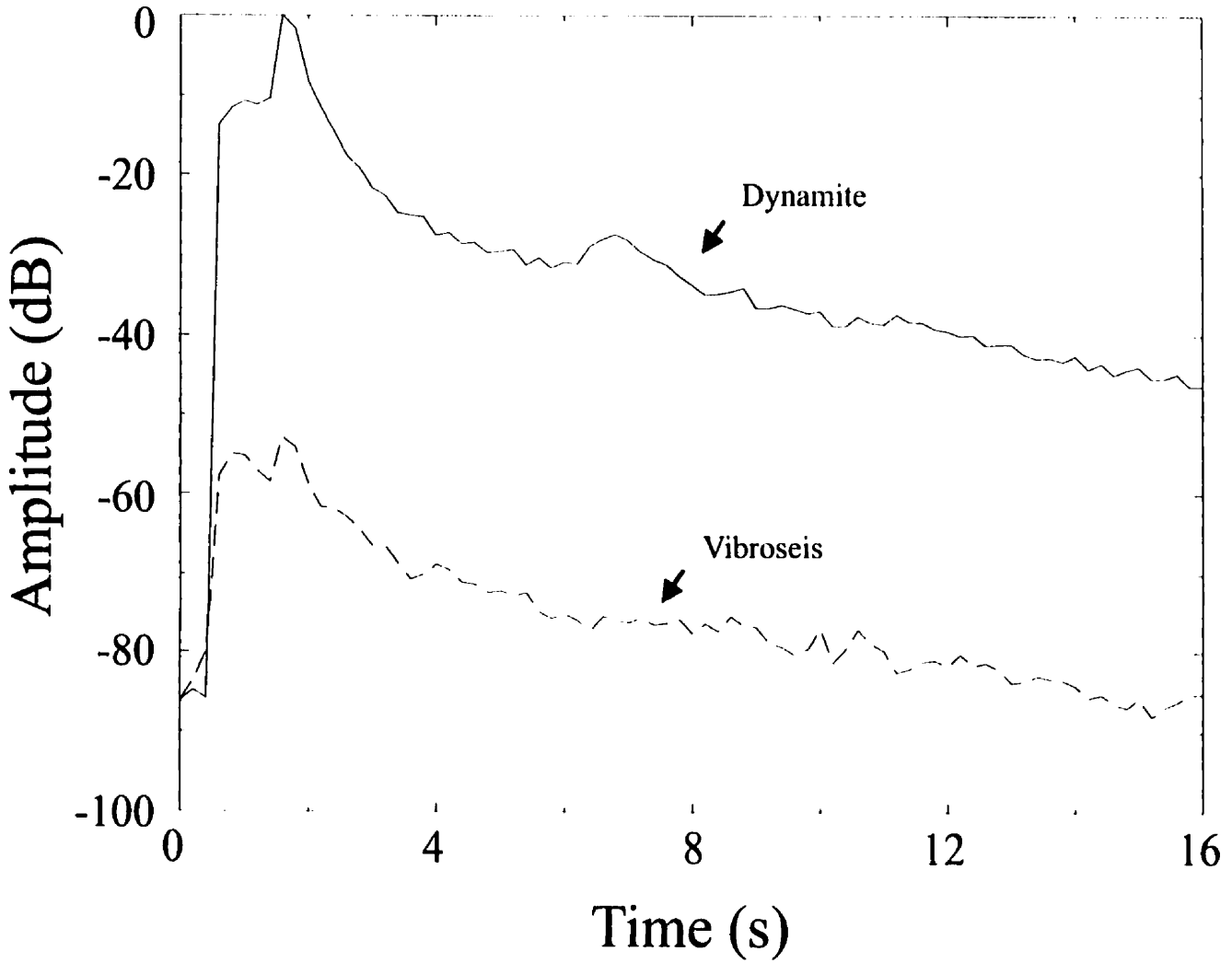

Fig. 2.6 Average amplitude decay curves of field shot records at 3 km offset.

2.2.2 Signal characteristics of the expanding spread profiles

The data quality is excellent with the exception of the records of E1. As in the case of the DEKORP Experiment (DEKORP Research Group, 1990), signals from a vibrator source were successfully recorded over an extended range. The amplitude level of observed reflections remains above the ambient noise level throughout the 16s recording length at all source-receiver separation. First arrivals are visible out to maximum offset (Fig. 2.7). On single-fold ESP field records, coherent reflections are clearly identifiable even at offsets around 18 km. Considerable reflectivity can also be seen throughout the records, including Moho reflection at ~12.5 s (Fig. 2.7).

2.3 Data processing

2.3.1 Dynamite and regional vibroseis data

The regional vibroseis data were processed by Western Geophysical Ltd. of Calgary. The essential parameters, however, had to be selected or approved by LITHOPROBE personnel in order to maximize the quality of the final sections. In general, the processing schemes of the dynamite and the vibroseis data sets are comparable (Table 2.2). However, the nature of the explosive source data required some modification to certain processing parameters. For example, more severe mutes were required to eliminate strong direct arrivals, and different cutoff frequencies were used in designing time-variant bandpass filtering to attenuate the air-wave coupled ground roll and retain frequencies below 12 Hz at subcrustal levels. Furthermore, a very effective noise suppression routine (Random Noise Attenuation) was employed to improve the *S/N* ratio in the vibroseis data. Lastly, *f-k* migration (Sheriff, 1991, p.

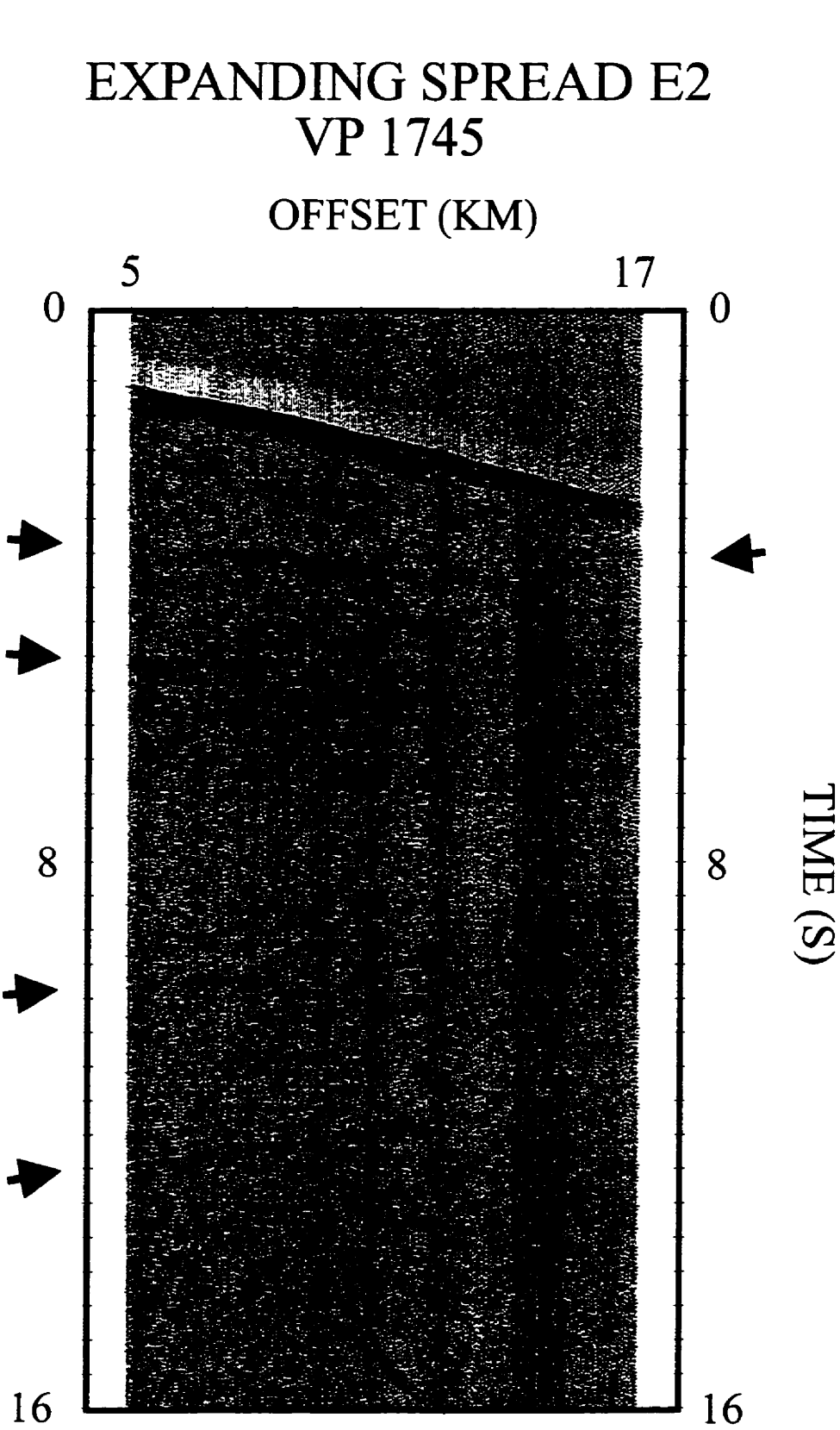

Fig. 2.7 Expanding spread field record with AGC applied.

119) was applied to the vibroseis data and due to the limitation of this routine, phase-shift migration (Sheriff, 1991, p. 193) with constant velocity (6000 m/s) was used for the dynamite data. Final interpretations were based on coherency-filtered (Sheriff, 1991, p. 42) migrated sections.

Table 2.2 Processing sequences

Vibroseis	Dynamite
Geometrical spreading correction	
Crooked line binning: 25 m x 2000 m	
Refraction statics: 400 m datum, 6000 m/s replacement velocity	
CMP sorting	
Deconvolution: minimum phase, 24 ms Lag, 180 ms operator	Deconvolution: minimum phase, Multi-windowed
Residual statics: maximum shift +/- 24 ms	
Velocity analysis	
NMO correction	
First break mute	
Trim statics: maximum shift +/- 20 ms	
Stack	
Random Noise Attenuation	f-x deconvolution
Time-variant bandpass filtering	
Time-variant scaling	Multi-windowed scaling
f-k migration	Phase-shift migration
Coherency filtering	

2.3.2 Expanding spread profiles

The overall processing sequence was similar to that of listed in Table 2.2. Although the ESP, having identical VP and spread sites as the regional profiling, could have used the earlier derived static correction directly, new solutions were calculated. Considerable variation in the thickness of the overburden (Fig. 2.8) required special attention during first break picking. To take advantage of the longer-offset recording various velocity extraction techniques were applied to the data. These results will be discussed in detail in Section 6.1.

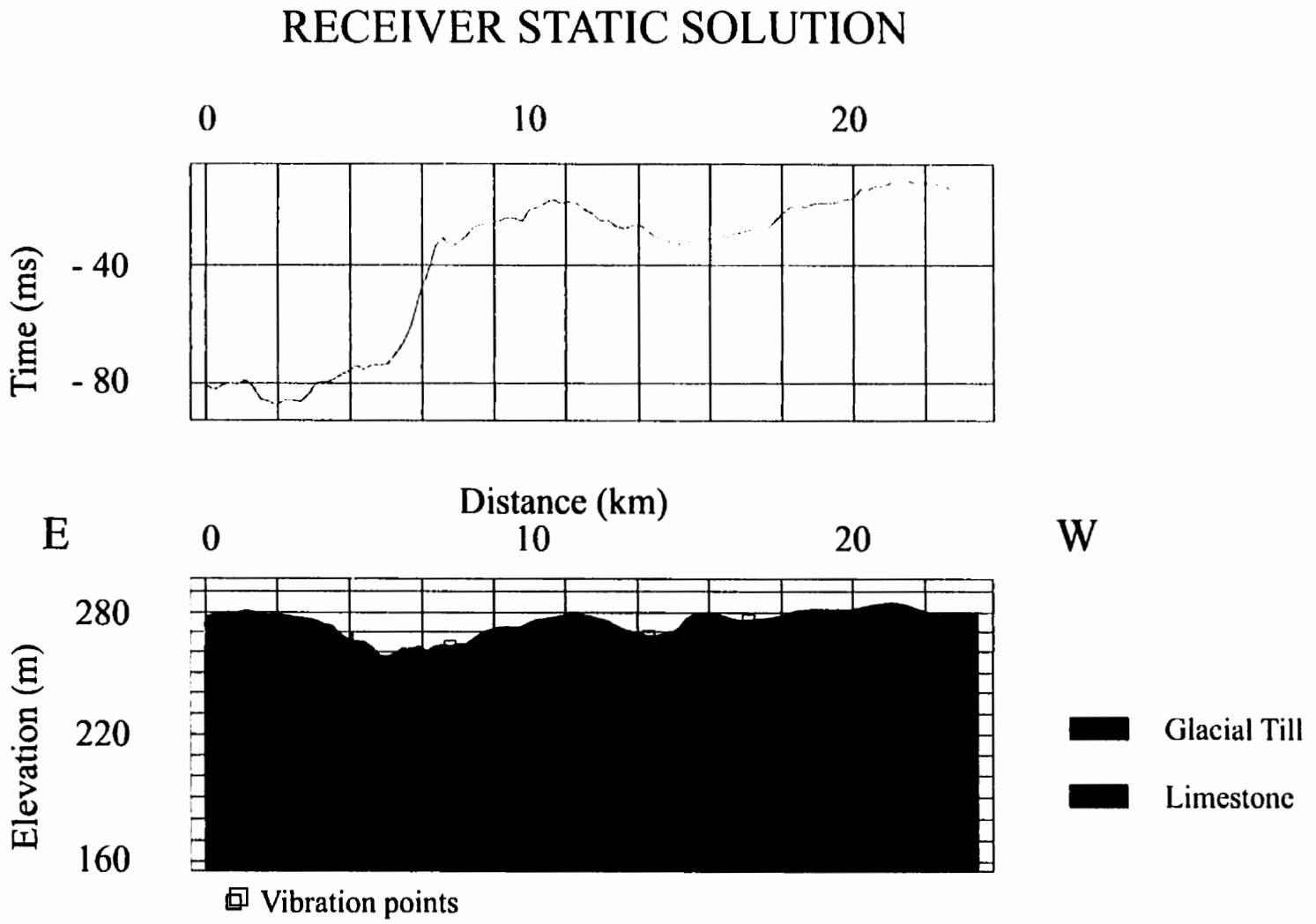

Fig. 2.8 Receiver static solution of expanding spread profile E2. The location of the first and last vibration points are indicated in each direction.

CHAPTER 3

COMPARATIVE SYNTHESIS OF THE REGIONAL VIBROSEIS AND EXPERIMENTAL DYNAMITE DATA

3.1 Vibroseis data

The >1000 km reflection profile across the THO provided unprecedented high quality images of the Paleoproterozoic crustal accretion and continent-continent collisional tectonism. The only comparable transects of orogens of similar age are the Babel marine survey of the Svecofennian orogen (BABEL Working Group, 1991) and a COCORP transect across the sub-Phanerozoic extension of the THO in North-Dakota and eastern Montana (Nelson et al., 1993). The results of the first phase of reflection seismic investigation were presented in a number of recent publications (Lucas et al., 1993, 1994; Lewry et al., 1994; White et al., 1994; Hajnal et al., 1996).

In summary, the reflection data immediately yielded new, unexpected insights into deep crustal structure below major zones of THO in the region of the experimental seismic surveys. A first-order characteristic of this new information was that well-defined packages of Proterozoic rocks dip to lower crustal depths beneath Archean cratons on both the west and east sides of the orogen. In the western part of the main transect line, reversed dips of a number of reflections, within the domal

feature of the Glennie domain (Lucas et al., 1993), outlined a major crustal scale culmination. Geological and geochronological data suggest that it may be cored by Archean rocks. Beneath this culmination, the well-defined reflection Moho marked a crustal root extending to at least 6-9 km.

The overall structural history appears to be marked by large-scale deformation along crustal-penetrating faults which bound sheets of mid- to lower-crustal rocks. An important consequence of the interpretation is that the seismic images mostly represent structures generated during the terminal continent-island arc-continent collision rather than structures related to pre-collisional subduction processes.

3.2 Comparison of the dynamite and the vibroseis data

Inspection of the stacked sections (Figs. 3.1 and 3.2) reveals, that the 60-fold vibroseis data provide higher quality images within the upper half of the crust. However, the dynamite data reveal comparable or better images below 8 s two-way traveltimes (TWT). The overall quality of the section derived from the explosive data improves as the nominal fold increases from 4 to 10 (approximately west of CMP location 7000, Fig. 3.1). Several major features, first reported by Lucas et al. (1993), can be correlated on both profiles. These include:

(1) strong reflections dipping westward beneath the bounding Hearne craton (A, Figs. 3.1 and 3.3);

(2) a well-defined, laterally continuous reflection Moho (M1, Figs. 3.1 and 3.4); and

(3) a crustal root (M2, Figs. 3.1 and 3.5).

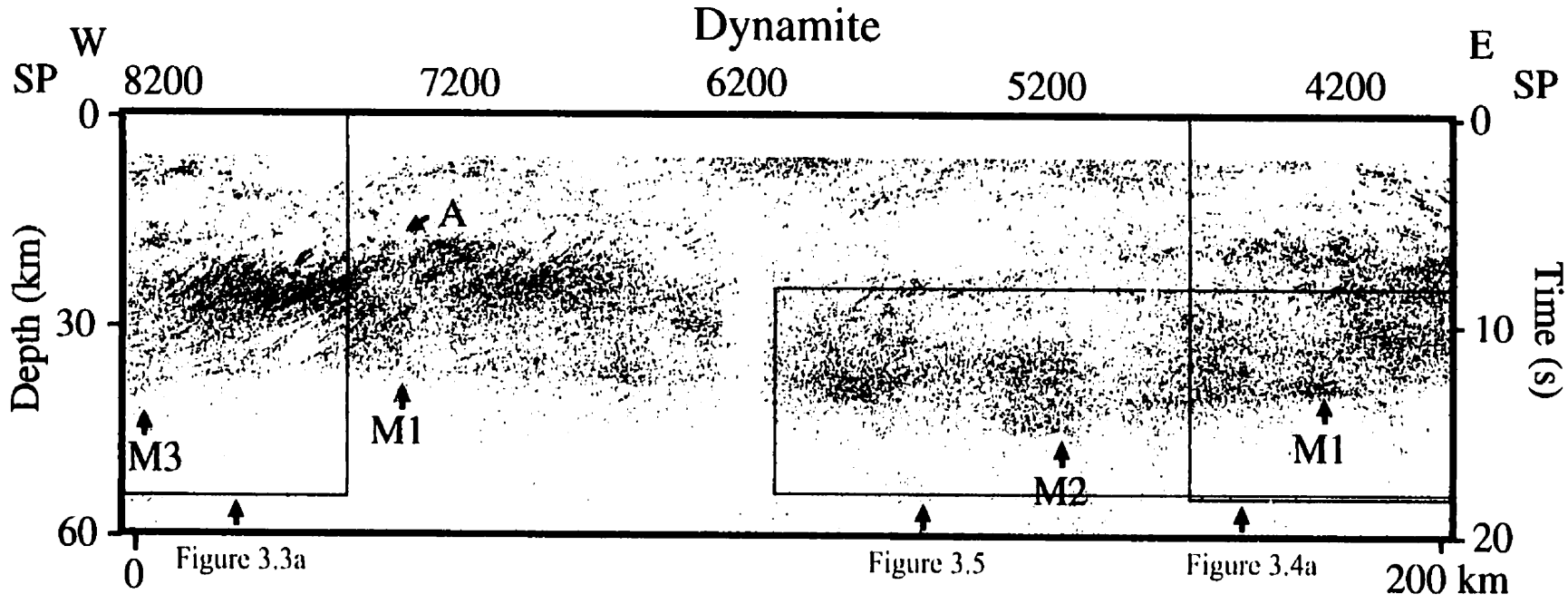

Fig. 3.1 Migrated dynamite section. Boxes indicate data segments shown in Figs. 3.3 - 3.5. Vertical exaggeration is 1:1 @6 km/s.

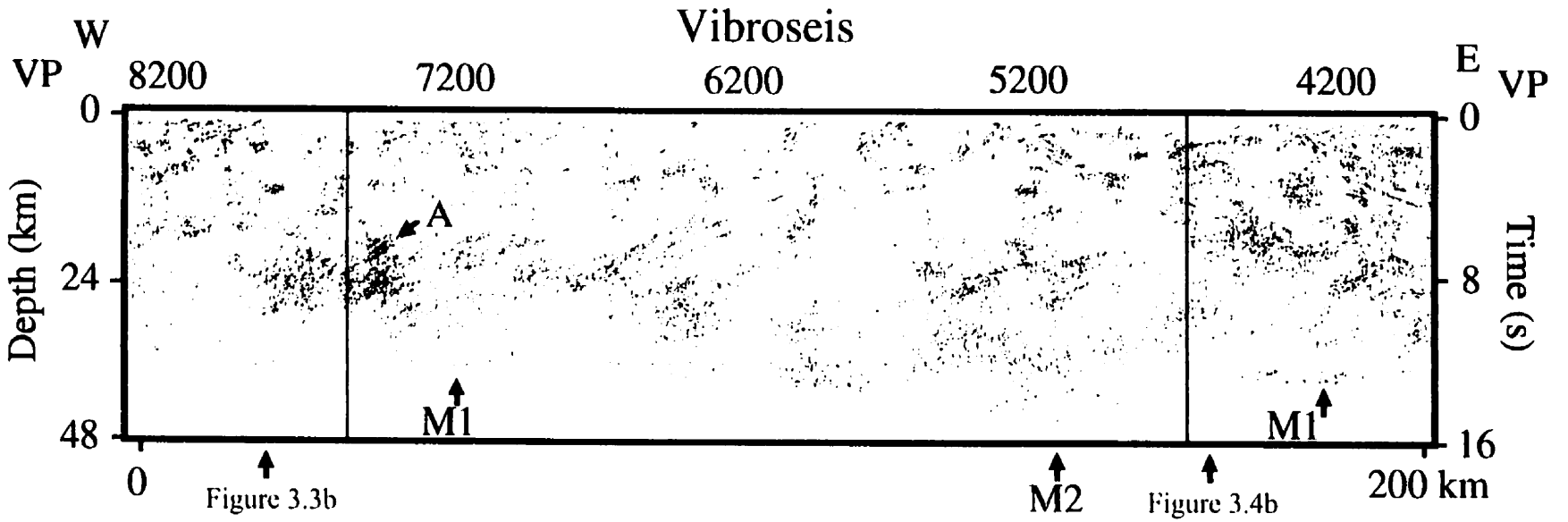

Fig. 3.2 Migrated vibroseis section of the westernmost 200 km of line 9. Boxes indicate data segments shown in Figs. 3.3 - 3.4. Vertical exaggeration is 1:1 @6 km/s.

The mid-crustal west-dipping reflections (A, Fig. 3.3) have more prominent seismic signatures on the dynamite based sections. This approximately 4 s thick, west-trending reflectivity zone is a well-defined characteristic feature of the western margin of the THO. Beneath the Williston Basin, 700 km to the south, recent COCORP deep seismic reflection probing (Baird et al., 1995) also mapped the presence of similar west-dipping reflection sequences that extend from the lower crust into the upper mantle. This southern coherent zone is interpreted as an indication of west-northwest dipping subduction polarity beneath the western craton during the Paleoproterozoic Trans-Hudson orogeny. In addition, the explosive source section shows that some mid-crustal diffractions have much larger apertures (e.g. greater lateral extent of K, Fig. 3.3) than were imaged by the vibroseis data. Consequently, the extended recording time of the dynamite data allows more accurate migration of these events.

The Moho, as a zone of subhorizontal reflectivity (M1), is evident throughout the entire 200 km length of the profile (Figs. 3.1 and 3.2) and separates highly reflective crust from largely transparent (devoid of coherent events) mantle. This reflector, however, is more distinct and clearly more continuous on the dynamite section (Figs. 3.1 and 3.4). The crustal root underlying the Archean domal structure beneath the Glennie domain (Lucas et al., 1993) is defined by deepening of the Moho (M2, Figs. 3.1 and 3.5) by 6-9 km to about 45 km depth (>15 s TWT). The structural detail of this deep feature is only marginally recognizable on Figure 3.2 but it is evident on Figures 3.1 and 3.5, further illustrating the improved imaging power of the explosive sources with increasing depth. In addition, a west dipping extension of this structure was also discovered in the upper mantle and traced to approximately 18 s TWT (N, Fig. 3.5).

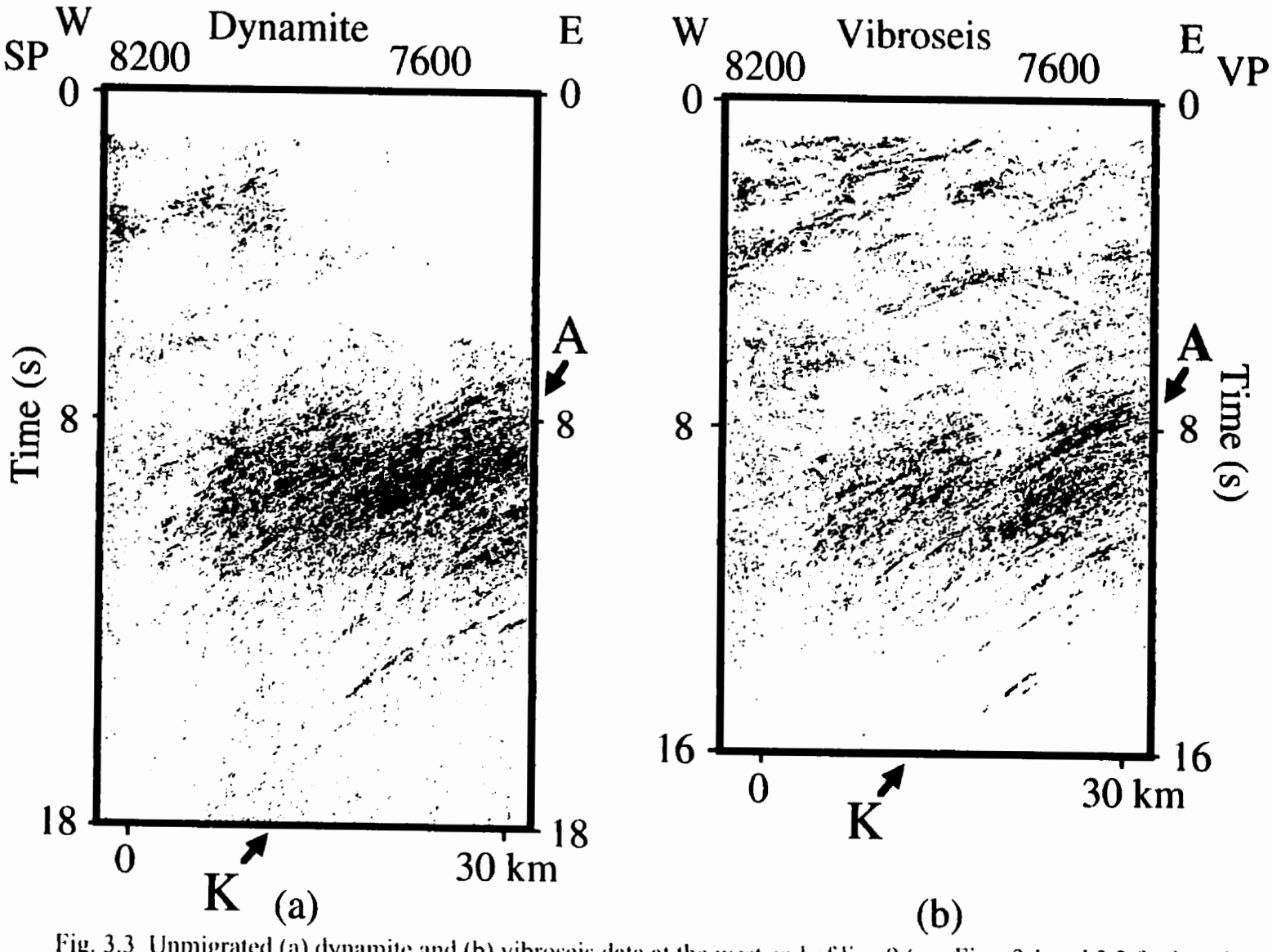

Fig. 3.3 Unmigrated (a) dynamite and (b) vibroseis data at the west end of line 9 (see Figs. 3.1 and 3.2 for location).

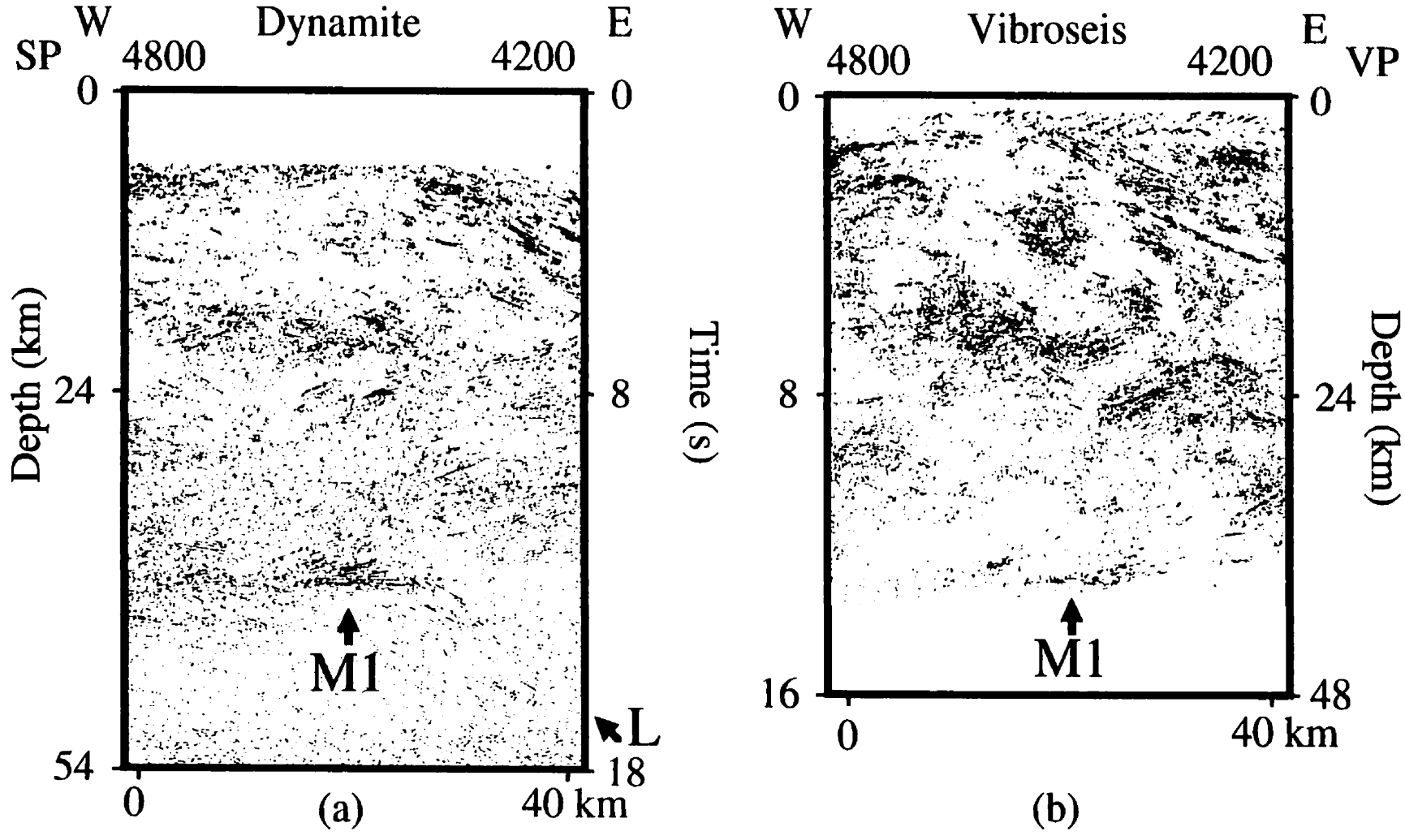

Fig. 3.4 Migrated (a) dynamite and (b) vibroseis data on the eastern flank of the culmination (see Figs. 3.1 and 3.2 for location).

These new seismic images indicate that the structure is not a simple depression on the upper-mantle as was inferred previously (Lucas et al., 1993), but a broad (3 s) zone of reflectivity that dips westward and extends more than 10 km below the younger regional Moho.

Two previously unrecognized structures (M3, Fig. 3.1; and L, Figs. 3.4, 3.5) were also revealed at or beneath the base of the crust, by the seismic images of the dynamite data. The M3 reflectivity maps westward deepening of the Moho beneath the eastern edge of the Wollaston Fold belt. This feature and its further westward extent were also recognized by wide-angle reflections of the 1993 refraction survey (Németh et al., 1996). L is an east-dipping zone of reflections originating below the Moho extending from 13 s to 16.5 s TWT and located beneath the eastern flank of the crustal root. The age and origin of the mantle reflections (L and N) are difficult to assess as the region has been subjected to several episodes of collisional deformation. Analogous events were observed in a number of recent studies from different tectonic settings of the world (BABEL Working Group, 1991; Flack and Warner, 1990; Baird et al., 1995; Calvert et al., 1995; Eaton et al., 1995) and were interpreted as relic structures relating to ancient suture zones.

The dynamite data along line 9 corroborates the vibroseis information regarding the nature of the Moho reflection (Lucas et al., 1993; Hajnal et al., 1996). Two types of reflection are evident:

(1) a subhorizontal Moho at ~12-13 s marked by 1-2 s laterally coherent waveform patterns and an abrupt decrease in reflectivity below it (M1); and

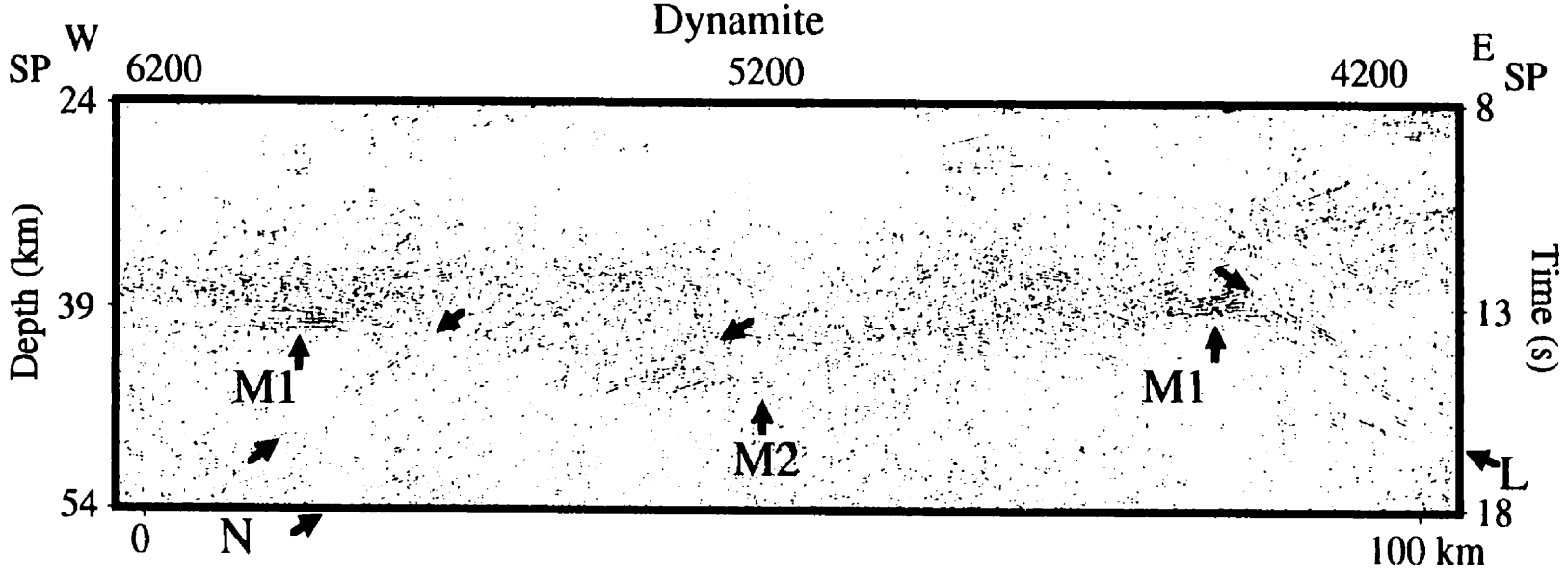

Fig. 3.5 Moho signature of the root segment of the dynamite profile (see Fig. 3.1 for location).

(2) gently-dipping to subhorizontal reflections that are not as bright as those defining the M1 Moho and do not form a distinct 1-2 s band, but rather appear to pass into overall lower crustal reflectivity (M2 and M3).

The relationship between the two types of Moho is indicated in several locations where subhorizontal reflections associated with the M1 Moho appear to cross-cut dipping reflections associated with older crustal structures the M2 and M3 Moho, thus indicating that the M1 Moho is younger than the M2 and M3 Moho.

Following Hajnal et al. (1996), the subhorizontal M1 Moho is interpreted in this thesis as a younger feature that was imposed on the older dipping crustal structure. An important new insight provided by the dynamite data is that not only does the M1 Moho and subhorizontal lower crustal fabric overprint dipping crustal structure, it also appears to overprint dipping mantle reflections (L and N, Fig. 3.5). On the COCORP line to the south of the US-Canada border (Nelson et al., 1993; Baird et al., 1995), vibroseis and dynamite reflection seismic surveys imaged moderately dipping reflections to 20 s; these reflections can be tied to crustal structures up-dip. Baird et al. (1995) propose that the Moho is actually at ~45 km (Hajnal et al., 1984; Morel-à-l'Hussier et al., 1987) and that the dipping sub-Moho reflective mantle represents eclogitized crust. This model is followed here, and it is suggested that the sub-Moho reflections emanate from eclogitized crust. The principal difference between the COCORP and LITHOPROBE images discussed in this study is the M1 Moho, which also appears to be superimposed on an earlier dipping crustal structure but is characterized by consistently strong reflectivity. The observation that the sub-Moho

reflections are parallel to those in the crust, which are interpreted as a collisional (1.83-1.80 Ga) fabric (Lucas et al., 1993; Lewry et al., 1994), suggests that the sub-Moho reflections may themselves be related to THO collisional tectonics. The origin of these reflections, however, is enigmatic. One possible model for the reflections beneath the Archean block coring the centre of the Reindeer Zone and culmination (Lucas et al., 1993), is that they were generated during imbrication of the underthrust Archean block (duplexing?), similar to stacking of slabs of North American crystalline basement beneath the Monashee culmination in the Omineca Belt of the Canadian Cordillera (Brown et al., 1992; Cook and Varsek, 1994). Alternatively, as evidenced by recent observation beneath the Urals (Knapp et al., 1996), these reflections could also represent a mantle shear zone developed during the assemblage of the oceanic and microcontinental terranes of the THO. It is possible, however, that these events are essentially sideswipes from adjacent crustal structures (Duren and Morris, 1992). It is worth pointing out, however, that evidence of mantle events does show up in the images obtained from the analysis of the refraction surveys in the region (Hajnal et al., 1997), as well as, on line S2C (Fig. 1.2) which runs normal to line 9.

Hajnal et al. (1996) interpreted the M1 reflections as being related to post collisional deformation of THO. An implication of this interpretation of the sub-Moho reflections and their association with the M2 Moho/crustal root is that the collisional structure is only locally preserved at the base of the crust and in the upper mantle where it has presumably been converted to eclogite. At this latitude in THO, post-collisional processes have been relatively effective in reshaping the lower crust/upper mantle. Hajnal et al. (1996) suggested that the principal process was ductile shear,

effectively transposing all earlier structures and utilizing the compositional/viscosity contrast (ie. granulite/eclogite) across the new Moho (M1) as a zone of detachment.

As with previous experiments the coincident vibroseis and dynamite surveys in the THO are complementary. Comparison of dynamite and vibroseis data from the 1991 THO seismic reflection survey demonstrates that the vibroseis data provide superior images of the crust to mid-crustal depths. However, the explosive data disclose more elaborate images of the lower crust and upper mantle despite its higher noise level due to the low survey fold. In particular, the lateral continuity of the Moho and the structural complexity of the previously identified crustal root are better imaged by the dynamite data. Furthermore, the extended traveltimes recorded during the dynamite survey permitted discovery of a number of significant mantle anomalies and improved migration of lower-crustal diffractions. These recent discoveries of the upper mantle structures may play a vital role in the reconstruction process of the tectonic evolution of the THO and are significant for the local diamond exploration industry who recently discovered the world's largest kimberlite field in the vicinity of the anomalous lithospheric structures (Leckie et al., 1997).

CHAPTER 4

VELOCITY EXTRACTION FROM REFLECTION DATA

Good knowledge of the velocity field is necessary for obtaining accurate images of the subsurface. The actual velocity distribution in the ground is implicitly contained within the acquired seismic traveltime data. The main objective in velocity work consists of extracting an estimate of the velocity distribution from the processed data through interval velocity estimation procedures. The natural output of most velocity schemes is an estimation of a macro-model describing the real medium as a series of layers separated by interfaces across which the velocity can vary discontinuously. There is considerable confusion, however, in relating the seismic velocity obtained from processing to the true propagation velocity. The abundance of different terminology illustrates this point. For example, the values of maximum coherency stacking velocities (V_{MCS} or simply V_S) are most of the time improperly substituted for the root-mean-square velocities (V_{RMS}) in the equation (Dix, 1955) establishing interval velocities (V_I). These derived interval velocities, almost without exception, are considered as simple average of propagation velocities (V_A) through the interval when, in fact, they are V_{RMS} in the interval (Al-Chalabi, 1994). Similarly, the velocities (V_{MIG}) obtained via pre-stack migration velocity analysis are quite unrepresentative of the velocity in the ground since they are

the measure of the horizontal (V_x) rather than the vertical component (V_z) of the velocity field (Deregowski, 1990). In addition, the normal moveout velocity (V_{NMO}) is almost invariably approximated with V_s stacking velocities.

There are several different approaches to the development of the velocity algorithms. When the estimation of reflector depth and velocity from seismic reflection data is formulated as a general inverse problem, tomographic techniques (Bishop et al., 1985; Stork and Clayton, 1991) provide a solution. Another related class of prestack velocity analysis techniques, generally called migration analysis, is based on optimizing the migration of the prestack data (Yilmaz and Chambers, 1984; Deregowski, 1990; Bancroft and Geiger, 1994).

The most commonly used velocity analysis is based on the use of some type of coherency measure between several seismic records taken with the time shift corresponding to a certain seismic signal's velocity (Taner and Koehler, 1969; May and Straley, 1979). Another approach has been realized in the different versions of slant stacking procedures (McMechan and Ottolini, 1980; Diebold and Stoffa, 1981; Schultz, 1982). In recent years, a significant number of new techniques (Key and Smithson, 1990; Katz, 1991; Jin and Madariaga, 1993; Thore et al., 1994) have been developed to obtain velocity information directly from reflection data.

The reliability of the seismic interpretation depends largely on the accuracy of the derived velocities. Thus, velocity estimation is incomplete without an uncertainty analysis of the results. The errors in these estimates can result from a number of factors, including indiscriminate substitution of V_s for V_{RMS}, limited validity of the moveout equations, static corrections, signal to noise (*S/N*) ratio, dipping reflectors, anisotropy,

and wavelet distortions at various stages of the acquisition and processing (Neidell and Taner, 1971; Al-Chalabi, 1974; 1994).

4.1 Traveltime equation and its approximations for horizontal layers

In order to achieve optimum focusing of the reflection data, velocity analysis algorithms assume some ideal conditions. The starting point for the derivation of the general traveltime and shot-receiver distance relationship for horizontally layered earth model are the parametric equations:

$$t_n(p) = 2\sum_{k=1}^{N} \frac{\Delta z_k / V_k}{\sqrt{1-(pV_k)^2}}, \tag{4.1}$$

$$x(p) = 2p\sum_{k=1}^{N} \frac{\Delta z_k V_k}{\sqrt{1-(pV_k)^2}} \tag{4.2}$$

where t_n is the total traveltime of the reflection from the nth layer, x is the offset, Δz_k is the thickness of layer k, V_k is the velocity in layer k, and N is the number of layers. The ray parameter is defined:

$$p = \frac{dt}{dx} = \frac{\sin i_k}{V_k} \tag{4.3}$$

where i_k is the angle of incidence.

Dürbaum (1954) illustrated that after expanding equation (4.1) in a Taylor series and inverting equation (4.2) for p as a function of x the traveltime equation can be expressed as:

$$t_n^2(x) = c_1 + c_2x^2 + c_3x^4 + c_4x^6 + \ldots \tag{4.4}$$

where the coefficients, c_1, c_2, c_3, ... are the functions of the layer parameters only. Introducing t_0, two-way vertical traveltime to layer N

$$t_0 = 2\sum_{k=1}^{N} \Delta\tau_k \tag{4.5}$$

where $\Delta\tau_k$ is the vertical transit time of layer k, and μ_j is the jth time-weighted moment of the velocity distribution

$$\mu_j = \frac{\sum_{k=1}^{N} \Delta\tau_k V_k^{\,j}}{\sum_{k=1}^{N} \Delta\tau_k} \tag{4.6}$$

the first four coefficients are (Taner and Koehler, 1969):

$$c_1 = t_0^{\,2}, \tag{4.7}$$

$$c_2 = \frac{1}{\mu_2} \approx \frac{1}{V_{RMS}^{\,2}}, \tag{4.8}$$

$$c_3 = \frac{\mu_2^{\,2} - \mu_4}{4t_0^{\,2}\mu_2^{\,4}}, \tag{4.9}$$

$$c_4 = \frac{2\mu_4^{\,2} - \mu_2\mu_6 - \mu_2^{\,2}\mu_4}{8t_0^{\,4}\mu_2^{\,7}}. \tag{4.10}$$

More coefficients of the series (4.4) are discussed by Marschall (1975). It is interesting to note that coefficients c_2, c_3 and c_4 have alternating signs ($c_2 > 0$, $c_3 < 0$, $c_4 > 0$) and the series (4.4) is rapidly convergent if the offset to depth (X/Z) ratio is small (Taner and Koehler, 1969; Al-Chalabi, 1973; Marschall, 1975). Strong oscillations occur when the ratio is high. The importance of terms higher than second-order is revealed in the numerical examples (Section 5.1).

Bolshix (1956) derived an alternate form of the moveout equation with an error in the sixth-order term. The corrected equation is provided by Castle (1994):

$$t_n(x) = t_0 + \frac{1}{2t_0\mu_2}x^2 - \frac{\mu_4}{8t_0^3\mu_2^4}x^4 + \left[\frac{\mu_4^2}{8t_0^5\mu_2^7} - \frac{\mu_6}{16t_0^5\mu_2^6}\right]x^6 + \ldots \tag{4.11}$$

If the first four terms of equation (4.11) are squared and the coefficients are compared with those of equation (4.4), equivalence of the two moveout equations is evident.

Assuming near vertical paths (i.e. relatively short shot-receiver offsets) Dix (1955) showed that the first two terms of equation (4.4) can be used to approximate the traveltime-distance relationship (omitting *n* subscripts from now on):

$$t^2(x) = t_0^2 + \frac{x^2}{V_{RMS}^2} \tag{4.12}$$

where V_{RMS} is defined by equation (4.8). This familiar hyperbolic equation has limited validity as a consequence of the truncation of the infinite series (Eq. 4.4). At larger offset to depth ratios (*X/Z*) the traveltime deviations from the hyperbolic trajectories become more evident and necessitate incorporation of higher order terms. Following Shah and Levin (1973), May and Straley (1979) suggested an alternative fourth-order equation derived through the use of orthogonal polynomials:

$$t^2(x) = c_1 + a_4(k_{42}k_{20} + k_{40}) + (c_2 + a_4k_{42})x^2 + a_4x^4 \tag{4.13}$$

where k_{ij} orthogonal coefficients are the function of the layer parameters and a_4 is the fourth-order coefficient. In case of $a_4 = 0$ equation (4.13) reduces to equation (4.12).

Assuming that if Bolshix's equation (Eq. 4.11) were extended to more terms, it would closely resemble Gauss's hypergeometric series, Malovichko (1978) derived the shifted hyperbola NMO equation:

$$t(x) = \tau_s + \sqrt{\tau_0^2 + \frac{x^2}{v^2}} \tag{4.14}$$

where

$$\tau_0 = \frac{t_0}{S}, \tag{4.15}$$

$$\tau_s = \tau_0(S-1), \tag{4.16}$$

$$v^2 = SV_{RMS}^2, \tag{4.17}$$

$$S = \frac{\mu_4}{\mu_2^2}. \tag{4.18}$$

Geometrically, this NMO equation describes a hyperbola that is symmetric about the t-axis and has asymptotes that intersect at (x = 0, t = τ_s). De Bazelaire (1988) demonstrated, using arguments from geometrical optics, that the shifted hyperbola is a more accurate NMO equation than the Dix NMO equation (Eq. 4.12). Moreover, Castle (1994) proved that equation (4.14) is exact through the fourth order in offset of equation (4.4). Castle (1994) gives the most general form of the shifted hyperbola NMO equation:

$$t(x) = \tau_s(x) + \sqrt{\tau_0^2(x) + \frac{x^2}{v^2(x)}} \tag{4.19}$$

where

$$\tau_s(x) = t_0\left[1 - \frac{1}{S(x)}\right], \tag{4.20}$$

$$\tau_0(x) = \frac{t_0}{S(x)}, \tag{4.21}$$

$$v(x) = \sqrt{S(x)}V_{SO}, \tag{4.22}$$

$$S(x) = \frac{\frac{x^2}{V_{SO}^2} - 2t_0(t - t_0)}{(t - t_0)^2}, \tag{4.23}$$

and V_{SO} is the small offset approximation of V_{RMS}. The simplest form of equation (4.23) is second order in offset:

$$S_2(x) = \frac{S + \alpha_1 x^2}{1 + \alpha_2 x^2} \tag{4.24}$$

where

$$\alpha_1 = \frac{\mu_2\mu_6 - 8\mu_4^2}{2\mu_2^5 t_0^2}, \tag{4.25}$$

$$\alpha_2 = -\frac{\mu_4}{4t_0^2\mu_2^3}. \tag{4.26}$$

Any more complicated *S(x)* function can be considered, as long as equation (4.19) fulfills the three requirements of a general NMO equation (Castle, 1994). Namely,

(1) the traveltime is an even function of the offset;

(2) the slowness (*dt/dx*) remains finite; and

(3) as the earth's velocity approaches a constant velocity (V_C) the NMO equation must approach the exact hyperbolic result (Eq. 4.12) with $V_{RMS} = V_C$.

4.2 Interval velocities derived from traveltimes

Dix (1955) derived a theoretical formula for near vertical angles, one that assumed horizontal layers, and a quadratic traveltime equation for a multilayered structure. Utilizing the quantities of equation (4.12), the interval velocity between the *n*th and *(n-1)*th reflectors is:

$$V_{I,n} = \left[\frac{V_{RMS,n}^2 t_n - V_{RMS,n-1}^2 t_{n-1}}{t_n - t_{n-1}} \right]^{1/2} \tag{4.27}$$

In case of the three-parameter moveout equation (4.14), de Bazelaire and Viallix (1992) derived a formula for estimating interval velocities:

$$V_{I,n} = \left[\frac{V_n^2 \tau_{p,n} - V_{n-1}^2 \tau_{p,n-1}}{\tau_{0,n} - \tau_{0,n-1}} \right]^{1/2} \tag{4.28}$$

Diebold and Stoffa (1981), and Schultz (1982) presented another technique that involves transformation from t - x space to τ - p space. These algorithms will be briefly discussed in Section 4.3. The main advantage of these methods is that they are valid at any offset and the predetermined V_{RMS} velocities are not needed.

Another approach is based on the inverse ray-tracing technique of Nowroozi (1990). The equation for interval velocities is the same as the one derived by Gonzalez-Serrano and Claerbout (1984), but Nowroozi (1990) uses geometrical consideration of two consecutive hyperbolic trajectories:

$$V_n^2 = \frac{\Delta x_i}{p_i \Delta t_i} \tag{4.29}$$

where

$$\Delta x_i = x_{n,i} - x_{n-1,i}, \tag{4.30}$$

$$\Delta t_i = t_{n,i} - t_{n-1,i}, \tag{4.31}$$

$$p_i = \frac{dt_{n,i}}{dx_{n,i}} = \frac{dt_{n-1,i}}{dx_{n-1,i}}. \tag{4.32}$$

The method can be used both numerically and graphically; thus it is possible to select regions of the traveltime where the *S/N* ratio is high. When p_i goes to zero at the limit, equation (4.29) equals equation (4.27). A similar graphical method was presented for

estimating interval velocities directly from diffraction patterns observed on common offset records by Cross and Knoll (1991).

All the above methods assume a stack of horizontal layers. For the general case of arbitrary curved interfaces, approximate formulas for interval velocities can be derived using wavefront curvature information (Hubral and Krey, 1980). The technique operates with the wavefront initiated at the reflection point. The inverse problem is solved by transferring the wavefront downward until it shrinks to zero reaching the reflection point.

4.3 Velocity analysis techniques

4.3.1 Coherency-based methods

Despite the fact that the second-order moveout equation (4.12) has limited validity, the most widely used velocity estimation method (Taner and Koehler, 1969) is based on this hyperbolic assumption. In this procedure moveout corrections are calculated as a function of vertical traveltime and offset for each trial stacking velocity, and then the coherence along this trajectory is measured. Several measures of coherence are discussed by Neidell and Taner (1971). Their preference is the semblance $S(t_0, V_S)$ measure that denotes the ratio of total energy of the stack of M traces within a gate length Δt to M times the sum of the energy of the component traces within the same time gate:

$$S(t_0, V_S) = \frac{\sum_{t=t_0-\Delta t/2}^{t_0+\Delta t/2} \left(\sum_{i=1}^{M} a_{ti} \right)^2}{M \sum_{t=t_0-\Delta t/2}^{t_0+\Delta t/2} \sum_{i=1}^{M} \left(a_{ti}^2 \right)} \tag{4.33}$$

where a_{ti} is the amplitude of the ith channel at time t. The locations of the peaks of the $S(t_0, V_S)$ are used to estimate interval velocities through the Dix formula. As the two-

term moveout equation becomes inaccurate for large offsets and heterogeneous velocity structures, May and Straley (1979) implemented a velocity analysis technique based on the fourth-order moveout equation (4.13). Unfortunately, the family of the polynomials they chose to determine the three parameters independently did not correspond exactly to the maxima in the velocity spectra, thus imposing lengthy iterations. Some improvements of the NMO corrections and the higher velocity resolution compared with those of the second-order method compensate for the increased computational time associated with this iterative velocity analysis.

Implementing the three-parameter equation (4.14) requires a double scanning, of τ_s and v, as functions of τ_0. In practice, it is obviously much faster to scan τ_s as a function of τ_0 for each segment of constant v, in order to take advantage of the fact that the NMO corrections are now static (de Bazelaire and Viallix, 1994). The computation time for this analysis, which seemed excessive (May and Straley, 1979), is now not much longer than that for the standard velocity spectrum calculation. Interval velocities can be computed with increased accuracy since the three-term equation parameters are independent of the maximum offset. Thus, the transformation of V_s velocities to V_{RMS} velocities is removed. Additional benefits include increased stacking energy and the broadened bandwidth (Thore et al., 1994).

It is important to note that the coherency-based velocity analysis techniques have high time resolution and noise suppression, but their resolution in the velocity domain is low. Despite the fact that these methods assume horizontally layered structures they exhibit limited success in handling velocity estimation for more realistic geologic models, i.e.

dipping layers, zones with velocity gradient and simple structures for which the raypaths remain close to symmetric.

4.3.2 Slant-stack methods

In the x - t domain the traveltime trajectory of a single layer is a hyperbola, but for a multilayered structure, they are pseudo-hyperbolae. In τ - p space the traveltime trajectories change into an ellipse for a single layer and ellipsoids for a multilayered structure. For a single layer, intersections of the ellipse with the p and τ axes give the inverse of the interval velocity and vertical two-way time, respectively. Shultz (1982) suggested a two-step technique, implemented in the τ - p domain, which directly estimates interval velocities. In the first step, a search for maximum coherence along various elliptical trajectories is performed. This is the same scanning operation as the velocity spectrum calculation in t - x space:

$$\frac{[\tau(p)-\tau_{n-1}(0)]^2}{[\tau_n(0)-\tau_{n-1}(0)]^2}+p^2V_n^{\,2}=1 \tag{4.34}$$

where $\tau_{n-1}(0)$ is the intercept time estimated for the previous layer.

Once the highest semblance-valued event (τ_n, V_n) is picked, a coordinate transformation is implemented so that the next trajectory conforms to a true elliptical shape. This second step is simply redefinition of intercept time τ:

$$\Delta\tau(p)=[\tau_n(0)-\tau_{n-1}(0)][1-\sqrt{1-p^2V_n^{\,2}}] \tag{4.35}$$

This two-step process of layer stripping continues until all velocities and intercept times are found. Diebold and Stoffa (1981) proposed a recursion formulation using the known

parameters of the first layer for initiation. The advantages of these techniques are that they utilize wide-angle energy and the predetermined V_{RMS} are not needed.

Linear techniques for velocity analysis are characterized by time resolution as high as the input records, their velocity resolution and the reliability of the results are lower than those of the coherency-based velocity analysis.

4.3.3 Tomography

Seismic tomography is usually formulated as an iterative Gauss-Newton algorithm that produces a velocity-depth model which minimizes the difference between traveltimes generated by tracing rays through the model and traveltimes measured from the data (Bishop et al., 1985; Stork and Clayton, 1991). Traveltime picking, however, is difficult in geologically complex areas and introduces the possibility of bias into what is selected. Tarantola (1984) proposed another approach through an iterated Born waveform inversion method. This technique requires a source estimate and extensive forward modeling. Tomographic techniques are most successful in handling significant lateral velocity changes but they are beset with velocity-reflector depth ambiguity problems.

4.3.4 Migration velocity analysis

The main advantages of using migrated data are that they do not require traveltime picking, knowledge of the source wavelet, and expensive computation of synthetic waveform data to assess the degree of data-model fit. Doherty and Claerbout (1976) introduced the wave equation to velocity estimation. The main principle is that a large

portion of the effect of reflector dip or curvature on the stacking velocity can be removed approximately by migrating common-offset panels with a first-guess velocity function, and then recalculating the stacking velocity in the migrated CMP gathers. Common-offset migration preserves the midpoint-offset structure of the data and hence enables the backing out of the implicit model-dependent NMO for each trace. Either dip moveout (DMO) or depth migration is applied to the prestack data. Conceptually, DMO requires the specification of accurate NMO corrections. However, the use of approximate velocities, followed by removal of the corresponding NMO, contributes to remove reflector point dispersal and to improve lateral resolution. Deregowski (1990) suggested integral or Kirchoff algorithms that are free to map arbitrary trace gathers into a migrated image by using accurately computed traveltimes from a velocity model. For each iteration, the velocity model is updated, and the iteration stops when the measured degree of similarity between the redundant images of the subsurface reaches a predetermined threshold level. The energy focusing (Yilmaz and Chambers, 1984) is a commonly used measure of similarity. Al-Yahya (1989) suggested another criterion to measure the flatness of reflectors in common-receiver panels. Similar to the semblance calculation, reflector curvatures are computed and then used to update the velocity field.

It is also possible to generate a prestack migrated data volume by migration of shot records (e.g. Van der Schoot et al., 1989). However, such migrations do not allow precise removal of the implicit model-dependent normal moveout after migration. The undue sensitiveness to the selected depth model makes these techniques not particularly suitable for post-migration velocity analysis. Bancroft and Geiger (1994) suggested another approach to sort the prestack data into common reflection point (CRP) gathers.

A CRP gather is a collection of all the traces that migrate into the CRP location and is sorted by the equivalent offset (h_e) concept. In the t-h_e space the traveltime trajectories remain pseudo-hyperbolic and are not affected by dip. Since the fold and the offsets of the CRP gathers are much greater than the CMP gathers, the focusing of the velocity energy on the semblance plots is improved.

4.3.5 Anisotropic velocity estimation

The mathematical foundation of the anisotropic traveltime-distance relationship was laid by Thomsen (1986) and Schoenberg and Muir (1989). Using Thomsen's (1986) notation, three parameters (V_{P0}, ε and δ) are needed to characterize the kinematics of P-waves in transversely isotropic media with vertical symmetry axis. Work on anisotropic traveltime inversion of reflection data has been done for laterally homogeneous subsurface models (Byun and Corrigan, 1990; Tsvankin and Thomsen, 1995). As shown in Tsvankin and Thomsen (1995), P-wave moveout from horizontal reflectors is insufficient to recover the three Thomsen parameters, even if long spreads (e.g. twice the reflector depth) are used. Additional information in the form of vertical velocity from check shots, well logs or S-wave data acquisition are required. Alkhalifah and Tsvankin (1995) demonstrated, however, that there is redundancy in Thomsen's three-parameter representation, and two parameters (V_{NMO} and η) are sufficient for all time-related processing (including nonhyperbolic moveout correction, if necessary). They also showed that these two parameters can be obtained solely from surface P-wave data. The inversion techniques were extended to media with dipping reflectors (Tsvankin, 1995),

horizontal transverse isotropy (Tsvankin, 1997) and vertically inhomogeneous transverse isotropy (Alkhalifah, 1997).

4.3.6 Other velocity extraction techniques

In recent years, a significant number of more advanced techniques have been developed to obtain velocity information directly from reflection data. Yilmaz (1989) presented a method to estimate proper velocity-stack gathers without amplitude smearing seen in conventional velocity-stack gathers. The conventional velocity-stack gather consists of constant-velocity CMP stacked traces. The method involves t^2-stretching of the CMP data in the offset space, followed by Fourier transforming along the stretched axis. Each Fourier component is then used in a least-squares minimization to compute the corresponding Fourier-component of the velocity-stack gather. Finally, inverse Fourier transform and 'unstretching' yield the improved velocity-stack. Removal of the amplitude smearing increases velocity resolution, thus allowing better separation of primaries from multiples.

Key and Smithson's (1990) method is based on the eigenstructure of the sampled data covariance matrix. This decomposition is carried out within hyperbolic windows (N time samples and M traces) that are moved through CMP data. In order to reduce computation cost the analysis window is partitioned into groups of adjacent traces which are stacked together resulting M' traces. Eigenvalues of the data covariance matrix (order of M') allow simultaneous estimation of the signal to noise energy ratio present within each window:

$$(S/N)=\frac{\left[\lambda_1-\frac{1}{M'-1}\sum_{i=2}^{M'}\lambda_i\right]}{\frac{1}{M'-1}\sum_{i=2}^{M'}\lambda_i} \tag{4.36}$$

where λ_i is the ith eigenvalue of the M'-order covariance matrix. An additional weighting factor is introduced to give strong discrimination in the presence of signal. It is defined as M'th power of the log-generalized likelihood ratio for the equality of the eigenvalues:

$$W_c = N \ln^{M'}\left[\frac{\left(\frac{1}{M'}\sum_{i=1}^{M'}\lambda_i\right)^{M'}}{\prod_{i=1}^{M'}\lambda_i}\right] \tag{4.37}$$

Finally, the covariance measure, C_c defined as the product of W_c and the previously defined *S/N* estimate:

$$C_c = W_c(S/N) \tag{4.38}$$

Key and Smithson (1990) illustrate through several synthetic and real examples that the covariance measure provides higher resolution than the second-order semblance technique. The mathematical relationship between the semblance and eigenstructure velocity estimators is derived by Kirlin (1992).

The asymptotically linear velocity estimation method was introduced by Katz (1991). It is based on the joint use of a linear velocity analysis technique and a penalty function, defined as a non-decreasing function of the *S/N* ratio estimate calculated in a moving time window. Consequently, the method takes advantage of the high noise suppression and time resolution of the semblance based velocity analysis and the high velocity resolution of the slant stacking techniques.

A scanless velocity analysis technique was proposed by Tieman (1993). In this procedure, two stacks with different weighting functions are generated after NMO corrections with a trial velocity. One set of the weights is chosen to emphasize the near offsets and the other one is to emphasize the far offsets. Cross correlation of the two stacks is used to update the velocity field. The convergence rate is fast; usually it requires only one or two iteration steps.

Recently, a number of non-linear methods have been proposed to provide accurate background velocity model for prestack depth migration/inversion of seismic data. Landa et al.'s (1989) coherency inversion is based on the assumptions that the reflectors zero-offset times are known and the velocity in each layer may vary laterally. Inversion, performed iteratively layer after layer, consists of finding a velocity-depth model which maximizes a semblance function calculated for all prestack gathers in a time window along traveltime trajectories generated by ray tracing. The method uses the generalized simulated annealing technique for updating the velocity field. At each iteration step, time-to-depth conversion is performed. Jin and Madariaga (1993) separated the inverse problem into linear and non-linear domains. A fast ray-tracing technique is used to retrieve the short wavelength features of the velocity field. The background velocity is inverted using a non-linear genetic algorithm applied to an objective functional defined in the migrated data space. Jervis et al. (1996) employed a very fast simulated annealing algorithm to estimate velocities. Their objective function measures the lateral consistency of reflectors between adjacent migrated shot records.

4.4 Velocity estimation for crustal data

The velocity estimation becomes more robust and accurate when longer offset (e.g. expanding spread data or refraction data) seismic data are incorporated. When larger offsets are included and wide-angle arrivals are processed, conventional velocity analysis techniques, based on the hyperbolic moveout assumption, have limited offset validity. Moreover, normal incident reflection coefficients in the earth's crust are usually small. The advantages of the long-offset data acquisition include increased event detection ability in low *S/N* environment, and availability of sufficient moveout to improve velocity resolution especially for larger depths. The NMO and differential NMO (DNMO) curves, calculated as the differences from the reference NMO curves with the lowest V_{NMO} in that particular group, for two crustal reflections are shown on Fig. 4.1. For an easier overview, Table 4.1 contains the necessary minimum offsets for two predetermined NMO and DNMO values. For example, the data acquisition should be extended to a minimum offset of 28 km to observe 50 ms time difference between any two velocities in the given range for a lower-crustal reflection (t_0= 12 s).

Table 4.1 Offsets for which NMO and DNMO exceeds predetermined levels

t_0(s)	velocity [km/s]	X_{NMO} [km] *NMO*=500 ms	X_{NMO} [km] *NMO*=1000 ms	X_{DNMO} [km] *DMNO*=50 ms	X_{DNMO} [km] *DNMO*=100 ms
4	5.8-6.7	14	21	15	23
8	6.0-6.9	20	29	21	31
12	6.3-7.2	26	36	28	40

Several authors have investigated the problems associated with crustal velocity estimation (e.g. Carrion, 1988; Trappe and Bittner, 1989; McBride et al., 1993; Brittan

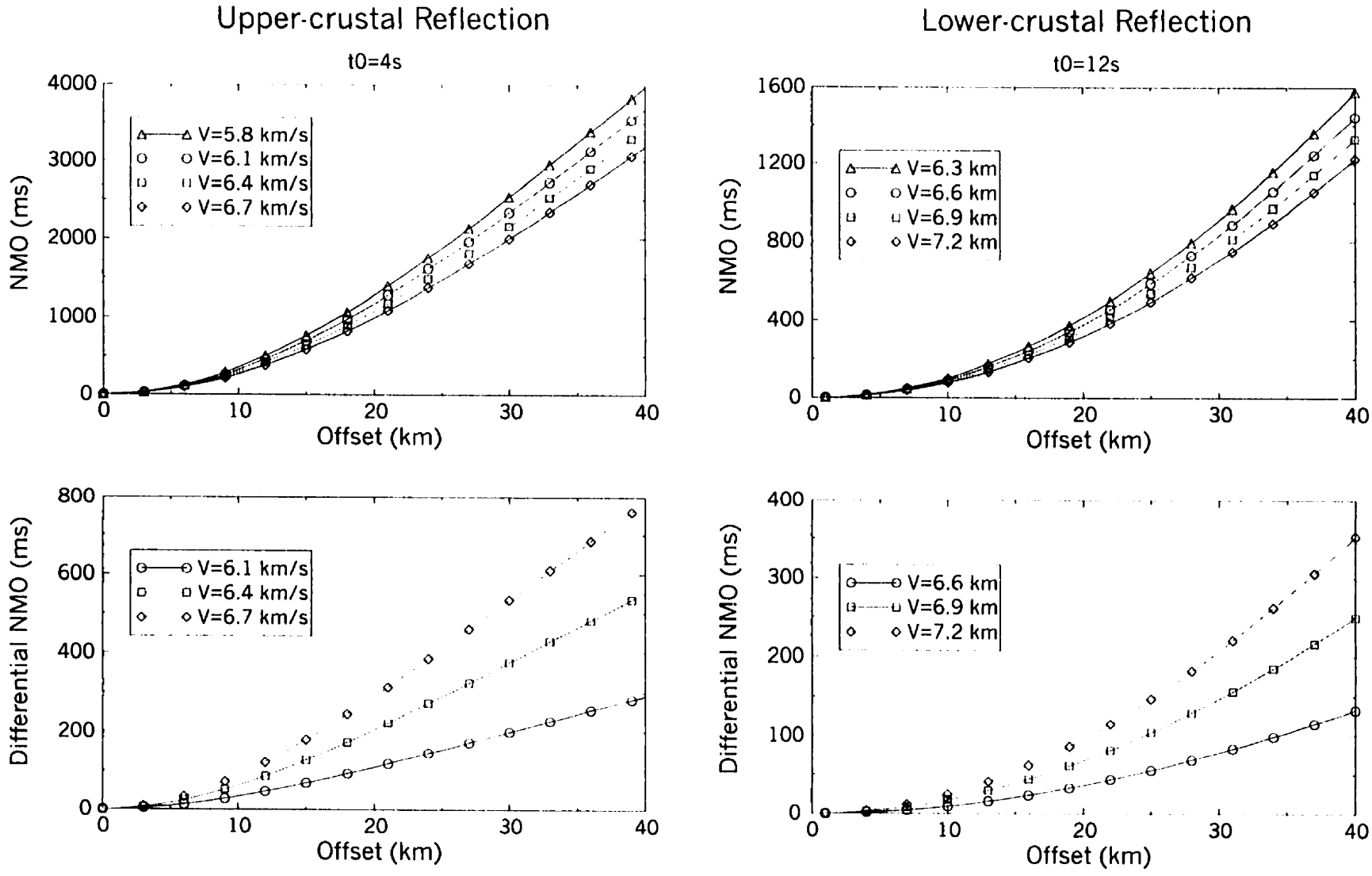

Fig. 4.1 NMO and DNMO curves for two crustal reflections with various velocities. DNMO curves were calculated as the differences from the NMO curve with the minimum velocity in that particular group.

and Warner, 1996). The main issues include how to establish optimal recording geometry for different crustal target zones, what velocity extraction method should be implemented, and why discrepancies between velocity models derived from near-vertical and wide-angle data exist. As one of the most commonly employed procedures to establish more accurate and detailed velocity information, the acquisition of expanding spread profiles was described in Section 2.1.2.

4.5 Traveltime ambiguity and uncertainties of the derived velocities

The accuracy of derived models is critical for imaging techniques such as migration and inversion. Therefore, the reliability of seismic interpretation is strongly dependent on the accuracy of these models. The factors affecting velocity determinations broadly fall into two categories:

(1) factors whose effect has a magnitude that can be estimated and a sense that can be established; and

(2) factors whose sense cannot be readily established although an estimate of the magnitude can be usually worked out (to a varying degree of accuracy), e.g. random noise and other random effects and qualitative effects such as those affecting resolution.

A description of factors of both categories has been given by Al-Chalabi (1979).

The use of the Dix formula for interval velocity calculation can lead to severe errors due to substitution of stacking velocities for V_{RMS} velocities without compensating for errors of the spread length or dipping reflectors. Shah and Levin (1973) pointed out that as the spread length increases, the V_{RMS} velocities determined from a seismic record differ

from those given by equation (4.8). Al-Chalabi (1974) developed a number of mathematical relationships between V_{RMS}, V_A, V_S, and V_I velocities and showed that V_S velocities are biased estimates of the V_{RMS} velocities. The bias is related to the spread length and the inhomogeneity factor of the medium, defined as:

$$g = \frac{1}{D^2} \sum_{k=1}^{N-1} h_k \sum_{j=k+1}^{N} h_j \frac{(V_k - V_j)^2}{V_k V_j} \tag{4.39}$$

where h_k is the thickness of layer k, and D is the depth of lower boundary of layer N. Other quantitative estimations of the errors of the interval velocities was carried out by Késmárky (1977) and Hajnal and Sereda (1981). The first author applied a statistical approach and established that the estimation of interval velocities is less influenced by the errors of static correction noise than by the uncorrelated noise. Uncorrelated noise is defined when the measurement errors are uncorrelated for successive horizons; static noise is defined when they are equal for all horizons. Moreover, he showed that the velocity estimation for thin layers becomes more erroneous with increasing depth. Hajnal and Sereda (1981) derived the maximum uncertainty of interval velocities due to the errors in V_{RMS} velocities and traveltimes:

$$\Delta V_{I,n} = \left(\frac{1}{ac}\right)^{1/2} \left[V_{RMS,n} t_n |\Delta V_{RMS,n}| + V_{RMS,n-1} t_{n-1} |\Delta V_{RMS,n-1}|\right]$$

$$+ \frac{1}{2}\left(\frac{b^2}{a^3 c}\right)^{1/2} \left[t_n |\Delta t_{n-1}| + t_{n-1} |\Delta t_n|\right] \tag{4.40}$$

where

$$a = t_n - t_{n-1}, \tag{4.41}$$

$$b = V_{RMS,n}^2 - V_{RMS,n-1}^2, \tag{4.42}$$

$$c = V_{RMS,n}^2 t_n - V_{RMS,n-1}^2 t_{n-1}. \tag{4.43}$$

This may sometimes be an overestimate because there is a negative correlation between velocity estimates in two successive layers. For example, if there is a large error in an estimated velocity for the *(n-1)*th layer, the error in the velocity for the *n*th layer will be the opposite sign, and will partly compensate the previous error that the velocity uncertainty in the *(n+1)*th layer might be small.

The appropriate expression for velocity uncertainties for dipping layers was obtained by Yanovsky et al. (1982). They showed that the error in velocity estimation is weakly dependent upon the form of the interfaces: when the dip changed from 10 to 40 degrees the value of the error increased only by 20 percent.

Landa et al. (1991) provided a robust and reliable method for uncertainty analysis of velocity estimates derived by coherency inversion. The uncertainties can be calculated using the combination of a quadratic approximation of the semblance coherency function around the global maximum and the Dix equation (4.27). The technique takes into account the local errors which are connected only to the reflection event under consideration, primarily to *S/N* ratio, and the global errors that are related to the uncertainties of the overburden.

The velocity-depth ambiguity in seismic traveltime data is an active area of research (Krey, 1989; Bickel, 1990; Lines, 1993; Ross, 1994; Sorin, 1994; Tieman, 1994). Factors that control the occurrence of velocity-depth ambiguity include the effective width of potential velocity anomaly, i.e. its spatial wavelength, its height above a reflector, and its thickness. Bickel (1990) showed that time structures that have a wavelength of about 2.7 times the average depth cannot be resolved into velocity and depth components using either traveltime or stacking velocity information. Ross (1994)

gives a mathematical treatment of not only whether a velocity perturbation can be distinguished from depth perturbation but also what aspects of each are determinable.

CHAPTER 5

MODELING

5.1 Traveltime equations

Modeling using ray-tracing (Zelt and Smith, 1992) was employed to estimate the offset range within which each traveltime approximation may be implemented. The parameters of Marschall's (1975) shallow model and two crustal models are listed in Table 5.1.

Table 5.1 Model parameters

	Marschall's Model		Crustal Models 1 and 2		
layer	Thickness	velocity[km/s]	thickness [km]	Velocity [km/s]	
1	1	2	2.9	5.8	4.0
2	1.5	3	9.3	6.2	5.8
3	2	4	12.8	6.4	6.6
4	2.5	5	13.4	6.7	7.3
Inhomogeneity factor		1.02 E-01		1.709 E-03	2.585 E-02

Calculations of traveltime deviations between the actual and the series expansion (Eq. 4.4) truncated beyond c_2, c_3, c_4 (Eqs. 4.8, 4.9 and 4.10) and c_5 respectively were carried

out (Figs. 5.1 and 5.2). The threshold value (ε) is defined as one-third of the period of the dominant wavelets to assure constructive interference of the stacked signals:

$$\varepsilon = \frac{1}{3f_D} \tag{5.1}$$

where f_D, the lower limit of the dominant frequency, is estimated as a function of depth (z) according to:

$$f_D = 80e^{-0.05756z} \tag{5.2}$$

The first reflections (layer 1) truly confirm the hyperbolic moveout; consequently these are not plotted. Although the higher than second-order traveltimes deviate to a greater extent from actual traveltimes at large offsets for the second reflections due to the significant contribution of the higher-order offset terms, their validity is better than that of the second-order approximation. The superiority of the higher-order traveltime equations becomes much clearer for the third and the fourth reflection. It is interesting to note that the traveltime approximations, at any given offset, exhibit an oscillatory nature which is proportional to X/Z ratios. The offsets ($X_{(k)}$) to which the calculated higher-order [denoted with (k) subscript] traveltime approximations are within a threshold (ε) of the actual traveltimes and the corresponding offset to depth ratios ($X_{(k)}/Z$) are tabulated in Table 5.2.

The most significant relative offset range extension is between $X_{(2)}$ and $X_{(4)}$ while the incorporation of higher order terms provides diminishing improvements. For clearer comparison, only the differences between the second- and the fourth-order approximations and the exact traveltimes for the two crustal models (Table 5.1) are displayed in Figure 5.3. The second-order approximation is valid to X/Z ratio of ~3.5 which translates to distances of 45, 92 and 119 km for the upper-, mid- and lower-

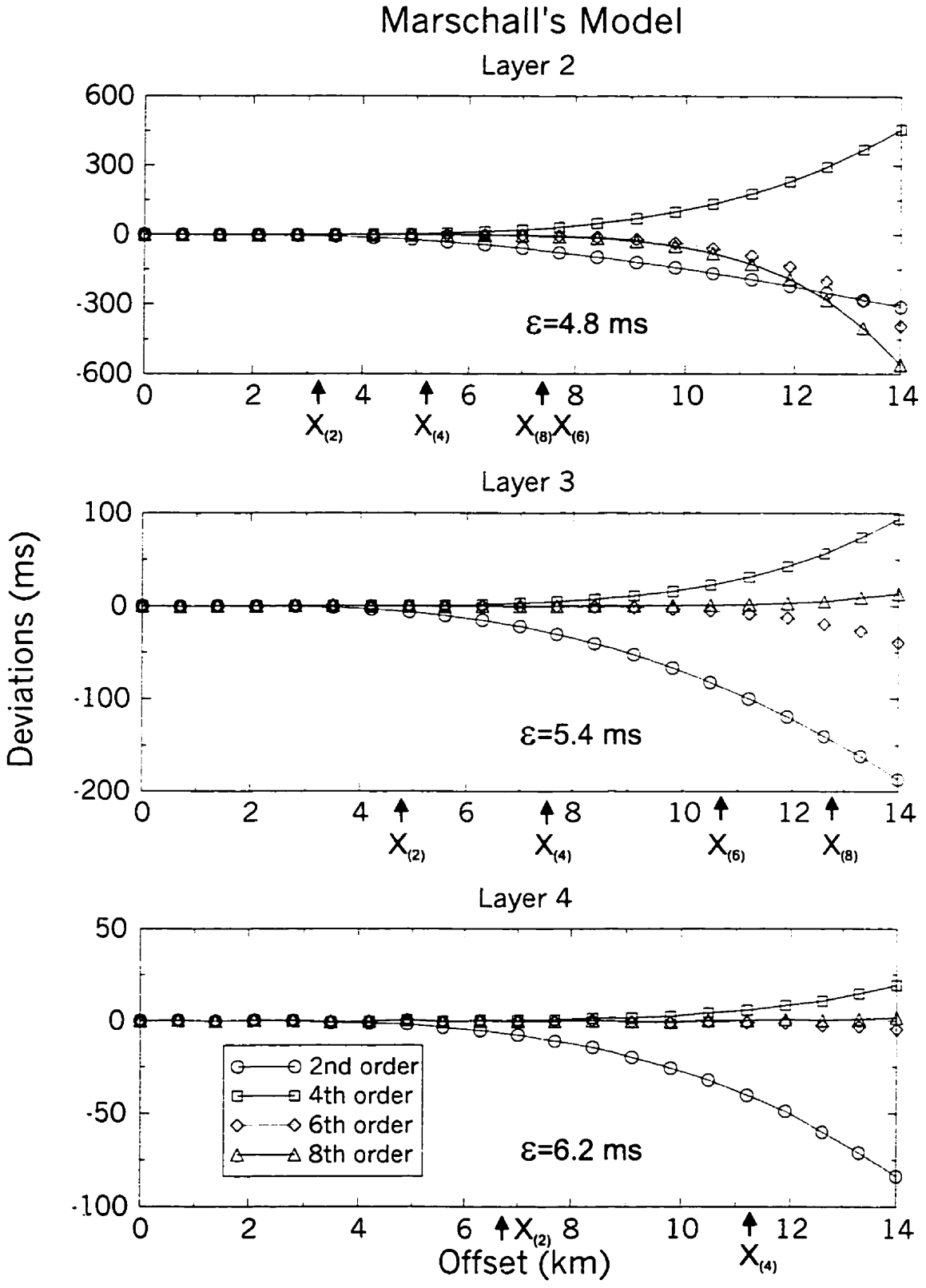

Fig. 5.1 Traveltime deviations between higher-order approximations and actual arrival times for Marschall's model (Table 5.1).

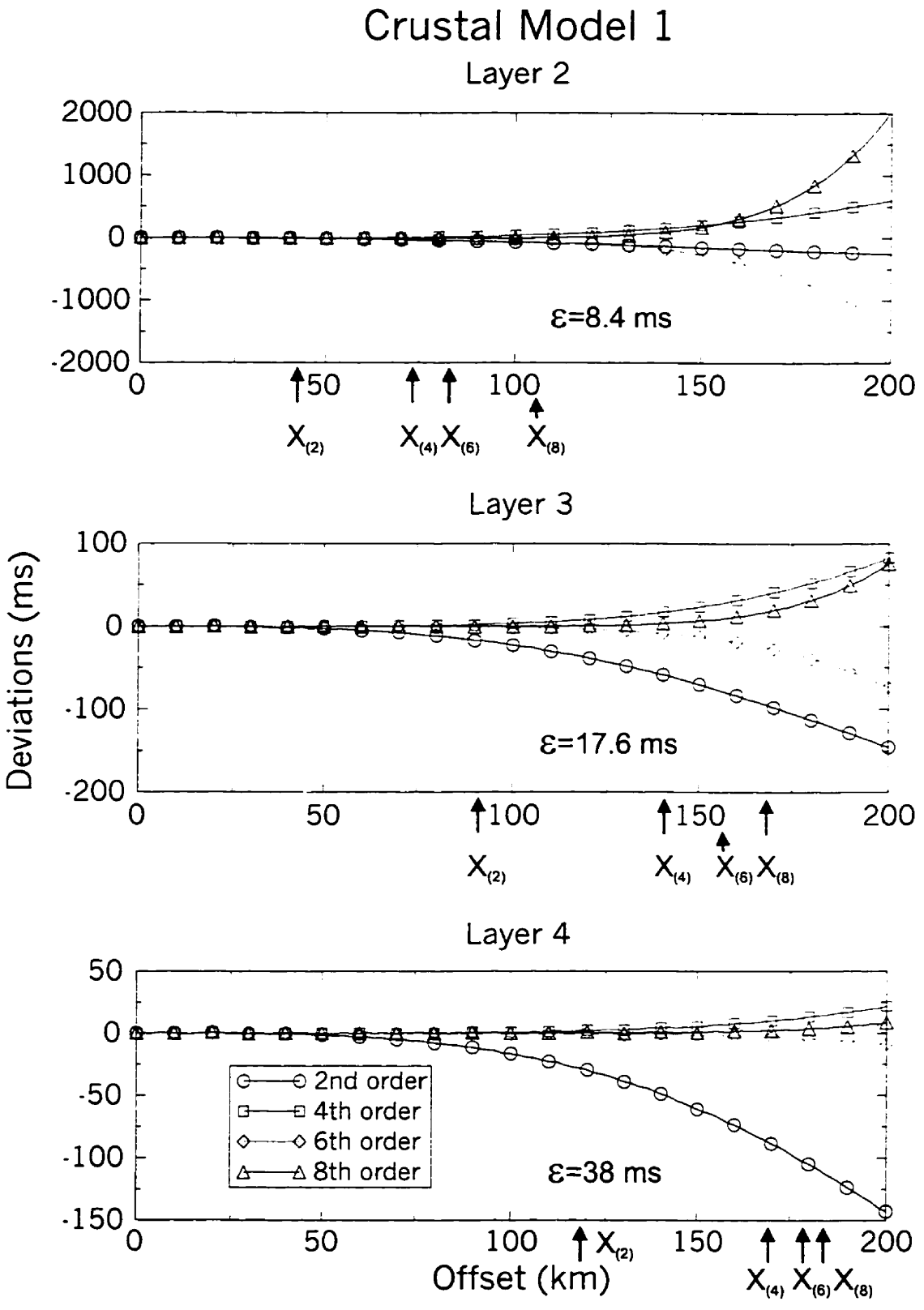

Fig. 5.2 Traveltime deviations between higher-order approximations and actual arrival times for crustal model 1 (Table 5.1).

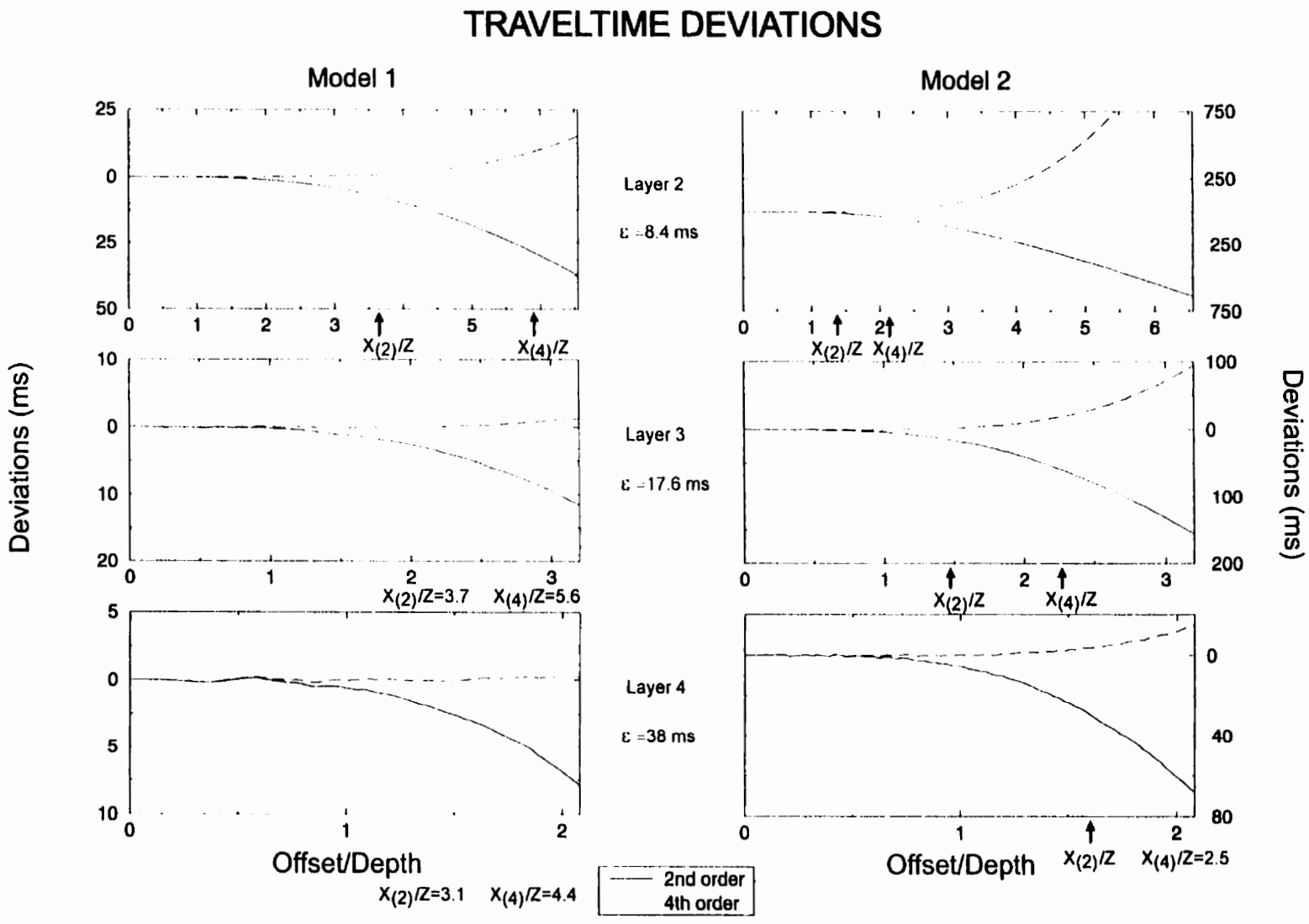

Fig. 5.3 Traveltime deviations of the second- and fourth-order approximations from actual arrival times for the crustal models in Table 5.1. 'ε' denotes one-third of the time period of the dominant wavelet. The maximum offset is 80 km in each plot.

crustal reflections of model 1. The equivalent offsets for model 2 are 17, 37, and 63 km, respectively with an average X/Z ratio of 1.5. The significant differences in $X_{(2)}$ offsets of models 1 and 2 emphasize that the validity of the second-order equation is mainly governed by an inhomogeneity factor defined for the medium (Eq. 4.39). In the constant-thickness models, the greater velocity variance in model 2 resulted in a higher inhomogeneity factor (Table 5.1). This, in turn, contributed to larger departures from actual traveltimes. Figure 5.3 also demonstrates that the fourth-order moveout equation exhibit less departure from the actual traveltimes than the second-order approximation.

Table 5.2 Maximum offsets and offset to depth ratios for which $abs\ [\ t - t_{(k)}\ ] < \varepsilon$

Marshall's Model									
layer	ε [ms]	$X_{(2)}$	$X_{(2)}/Z$	$X_{(4)}$	$X_{(4)}/Z$	$X_{(6)}$	$X_{(6)}/Z$	$X_{(8)}$	$X_{(8)}/Z$
2	4.8	3.2	1.28	5.3	2.12	7.6	3.04	7.3	2.92
3	5.4	4.7	1.04	7.6	1.69	10.6	2.35	12.6	2.80
4	6.2	6.7	0.96	11.3	1.61	14.6	2.08	16.2	2.31
Crustal Model 1									
layer	ε [ms]	$X_{(2)}$	$X_{(2)}/Z$	$X_{(4)}$	$X_{(4)}/Z$	$X_{(6)}$	$X_{(6)}/Z$	$X_{(8)}$	$X_{(8)}/Z$
2	8.4	45	3.69	71	5.82	85	6.96	107	8.77
3	17.6	92	3.68	140	5.6	157	6.28	167	6.68
4	38	119	3.10	167	4.35	179	4.66	183	4.76
Crustal Model 2									
layer	ε [ms]	$X_{(2)}$	$X_{(2)}/Z$	$X_{(4)}$	$X_{(4)}/Z$	$X_{(6)}$	$X_{(6)}/Z$	$X_{(8)}$	$X_{(8)}/Z$
2	8.4	17	1.39	26	2.13	32	2.62	38	3.11
3	17.6	37	1.48	56	2.24	66	2.64	70	2.8
4	38	63	1.64	96	2.5	108	2.81	111	2.89

Therefore, applying the fourth-order approximation in velocity analysis, the offset range can be extended to distances of 26, 56, and 96 km for reflections of model 2. Consequently, in the case of seismic reflection investigations utilizing larger offsets, especially over heterogeneous subsurface, more accurate velocity spectra can be obtained through the use of higher-order approximations.

5.2 Velocity analysis techniques

In this section the performance of the standard second-order semblance, the τ - p (Schultz, 1982) and the covariance (Key and Smithson, 1990) velocity estimators adapted to crustal environment will be examined (see Sections 4.3.2 and 4.3.6). The velocity analysis was carried out on crustal models listed in Table 5.1. Uniform 16 Hz Ricker wavelets and the same number of traces (M = 120) were employed for all offsets. In the τ-p analysis the trace spacing (Δx) was reduced to avoid spatial aliasing according to formula:

$$\Delta x \leq \frac{V_{\min}}{2 f_{\max}} \tag{5.3}$$

where V_{min} is the minimum velocity; and

f_{max} is the maximum frequency.

Alternatively, low-pass filtering can be applied to the data prior to the τ - p transform. To ensure that the resulting number of traces would be equal or comparable to the number used in the other two methods, an appropriate ray parameter sampling (Δp = 1.4 E-06) was selected.

In the covariance velocity estimation, the key issue is the proper selection of M' (Eqs.

4.36 and 4.37). The primary objective of the data reduction scheme is to reduce computation cost and also to improve *S/N* ratios of the input gathers. The degree of partial stacking must be governed by the moveout characteristics of the reflections. In order to avoid data degradation only traces with differential moveouts less than one-third of the period of dominant wavelet can be stacked. The following formula has been used to calculate the minimum theoretically allowable value of M':

$$M'(t) = 3Mf_D(\Delta t)_{\max} \tag{5.4}$$

where $(\Delta t)_{max}$ is the moveout at maximum offset in s/trace.

However, equation (5.4) results in significant overestimation of value of M' since it precludes even minimal signal distortions at the maximum offsets. Figure 5.4 reveals that when M' = 40, which is half of the value calculated using Eq. (5.4), the velocity estimation remains reliable for layer 4. In the numerical examples considered here as well as the tests on field data, M' was kept constant (M' = 60). This value not only minimizes signal distortions but also results in comparable computational time to that of the semblance algorithm. It is important to note that execution time increases ~10 fold when M' is increased from 60 to 120. Additional advantage of the partial stacking is that interfering events with differing moveouts are partially cancelled.

Key and Smithson (1990) in their analysis used typical M' values between 4 and 10 and they also suggested the weighting factor (W_c) as the log-generalized likelihood (LGL) ratio to be raised to the power M' (Eq. 4.37). The original formula, proposed in the underwater passive listening domain by Ligget (1972) on "heuristic" grounds, does not contain this power. It appears that raising LGL to the power M' is an effective tool to stretch the dynamic range of W_c (Eq. 4.36). In crustal velocity analysis the

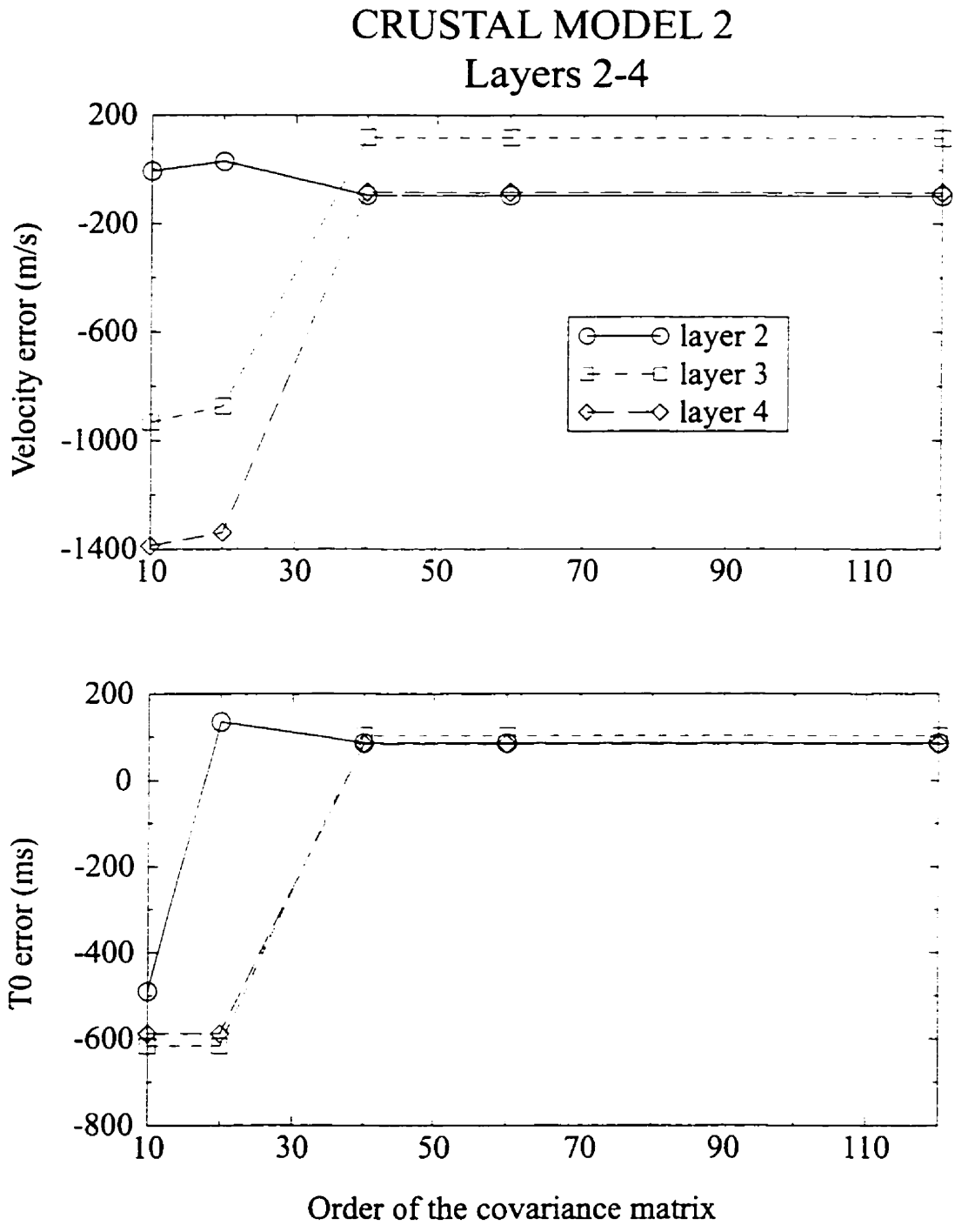

Fig. 5.4 Covariance velocity estimation for layer 4 of model 2 with various orders of the covariance matrix. Offset = 42 km.

range of M' usually varies between 40 and 60, which results in significant dynamic range of the velocity spectra. This amplitude stretch can lead to marginal recognition or disappearance of lesser-pronounced peaks even if AGC or other amplitude balancing has been applied to the data prior to the velocity analysis (Fig. 6.4). Consequently, it is suggested that the power (P) of the LGL and the order of the covariance matrix (M') should be uncoupled and that Eq. (4.37) have the most general form:

$$W_c = N(t)\ln^P\left[\frac{\left(\frac{1}{M'(t)}\sum_{i=1}^{M'(t)}\lambda_i\right)^{M'(t)}}{\prod_{i=1}^{M'(t)}\lambda_i}\right] \tag{5.5}$$

Key and Smithson (1990) have already indicated the potential benefit of adaptive changes of the number of time samples [$N(t)$]; however, it is of greater importance in crustal studies. The time variant window dimension would accommodate changing wavelet duration. It is defined either with some empirical function similar to that of Eq. 5.2 or with time-frequency pairs established by spectrum analysis. The control of $M'(t)$ can be achieved in similar fashion. The above changes have been incorporated in the algorithm, but in the following numerical examples constant M', N and P (= 2) values were used in order to allow clearer comparison with the performances of the other two techniques.

In the conventional second-order semblance velocity analysis large, offsets containing wide-angle reflection and refraction events are muted out. In the slant-stack method of Schultz (1982) both sets of data along with precritical reflections are utilized. This technique directly estimates interval velocities in a two-step process

(Section 4.3.2). Consequently, these are more stable than those derived through the Dix equation (Eq. 4.27) which are sensitive to V_{RMS} and t_0 picks of the investigated and the previous layers. Enhanced resolution and estimation accuracy are achieved because previously neglected wide-angle arrivals make a significant contribution in the estimation procedure. In view of ESP recording geometry (Section 2.1.2), however, only precritical reflections were included in the modeling studies.

Figure 5.5 indicates that the τ - p analysis provided the most robust parameter estimation for layer 2 of model 2 while the covariance method resulted in the largest V_1 and t_0 errors up to a maximum offset of 24 km. Beyond this offset the semblance calculation based on a hyperbolic moveout assumption cannot be implemented. Considering the 16-Hz wavelet instead of the 40 Hz one used in Table 5.2, the $X_{(2)}$ offset would be extended to 22.5 km (Fig. 5.3). While the τ - p and semblance amplitudes can be directly compared (since these employ the same coherence measure), the covariance values are normalized to the maximum value. It is important to note that for upper-crustal reflections, even short spread length results in a reliable estimation process, and that there is no additional improvement beyond the maximum offset of 12 km.

The benefit of incorporation of larger offsets is more evident in the parameter estimation for layer 4 of model 2 (Figs. 5.6 to 5.8). While all three methods exhibit small t_0 errors, even with small spreads, reliable velocity estimation requires maximum offsets of 18 km. The τ - p amplitudes monotonously increase with the offset and the amplitudes in the other two methods define an optimum offset range of $18 - 30$ km.

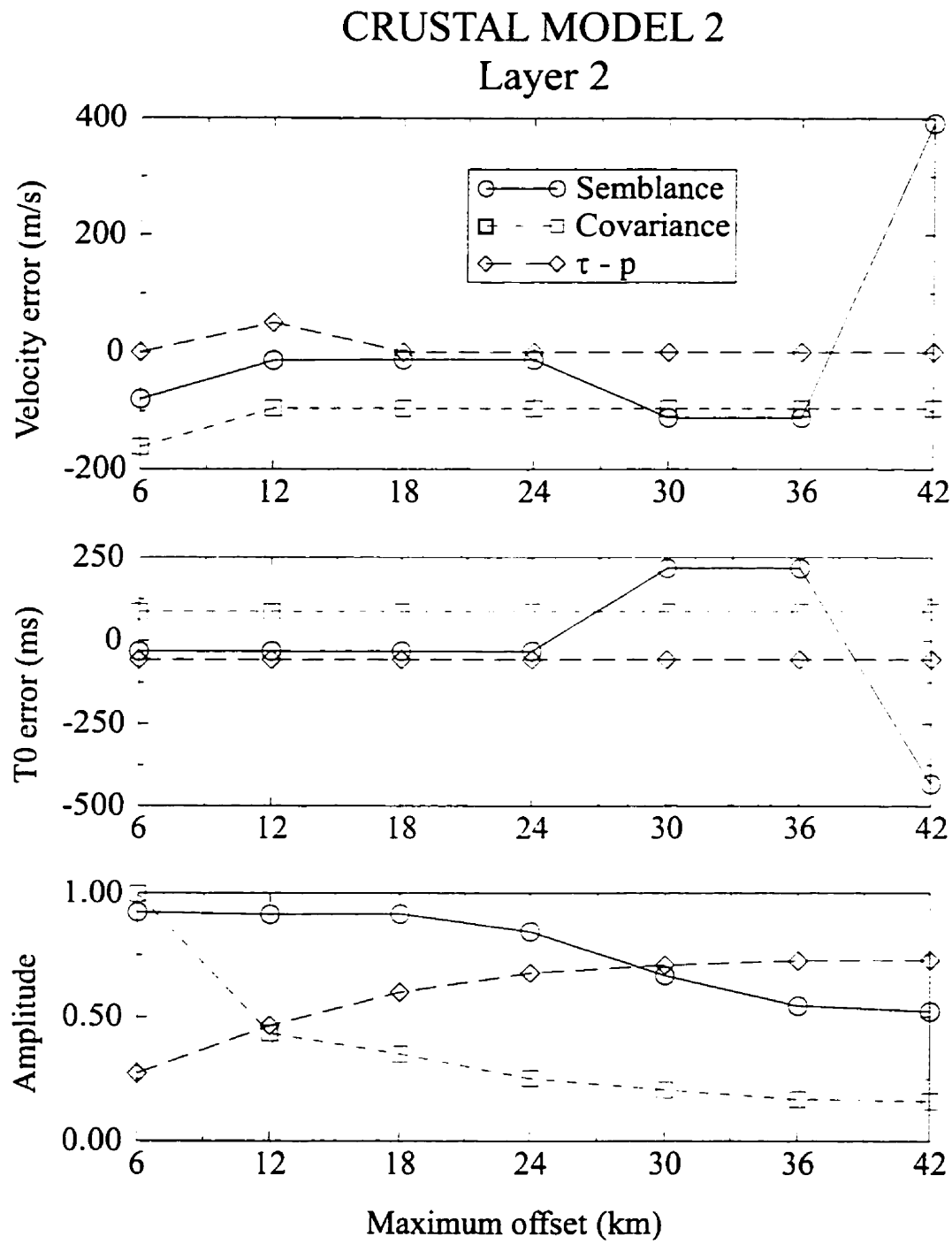

Fig. 5.5 Various velocity estimators for layer 2 of model 2.

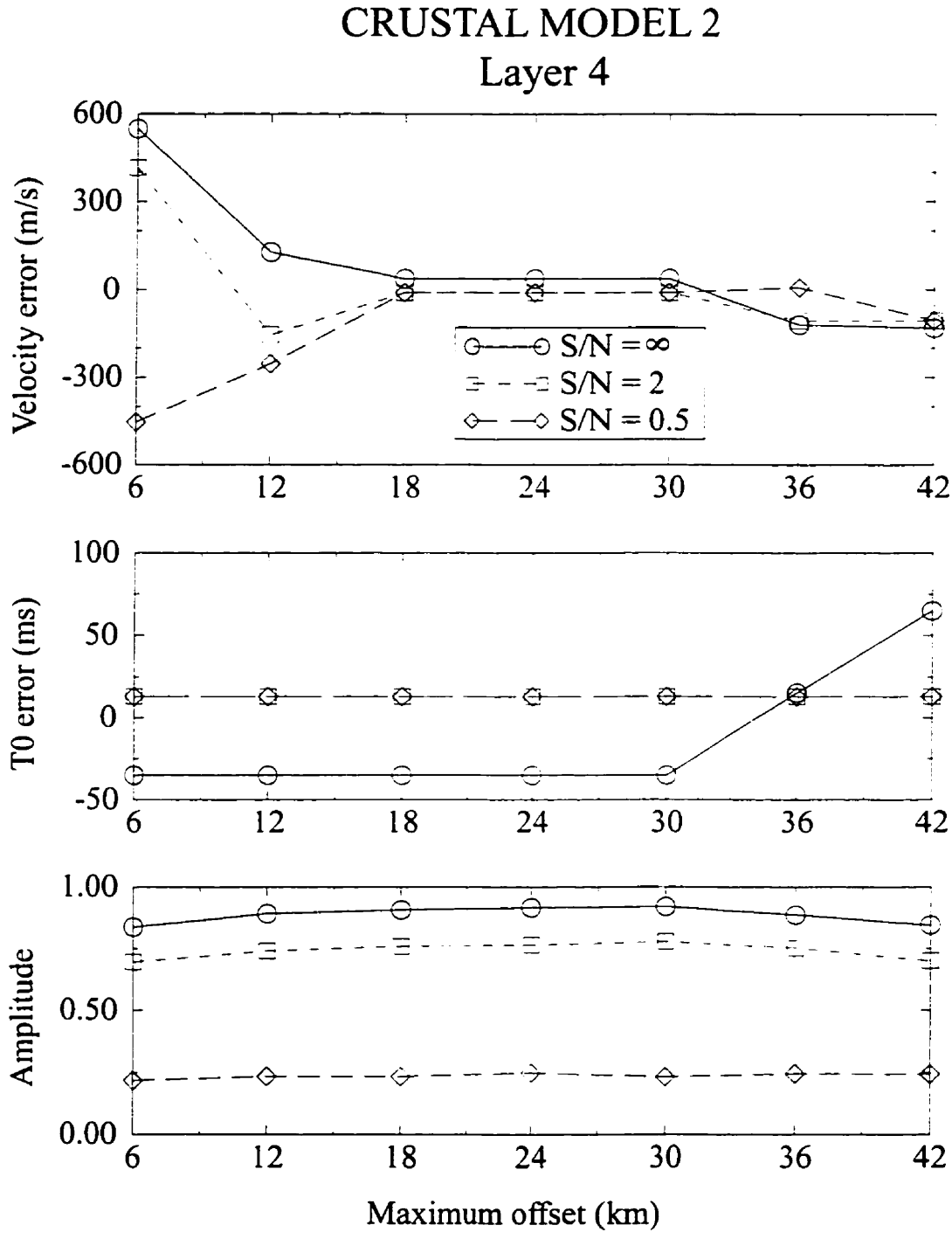

Fig. 5.6 Second-order semblance velocity estimation for layer 4 of model 2 with various S/N.

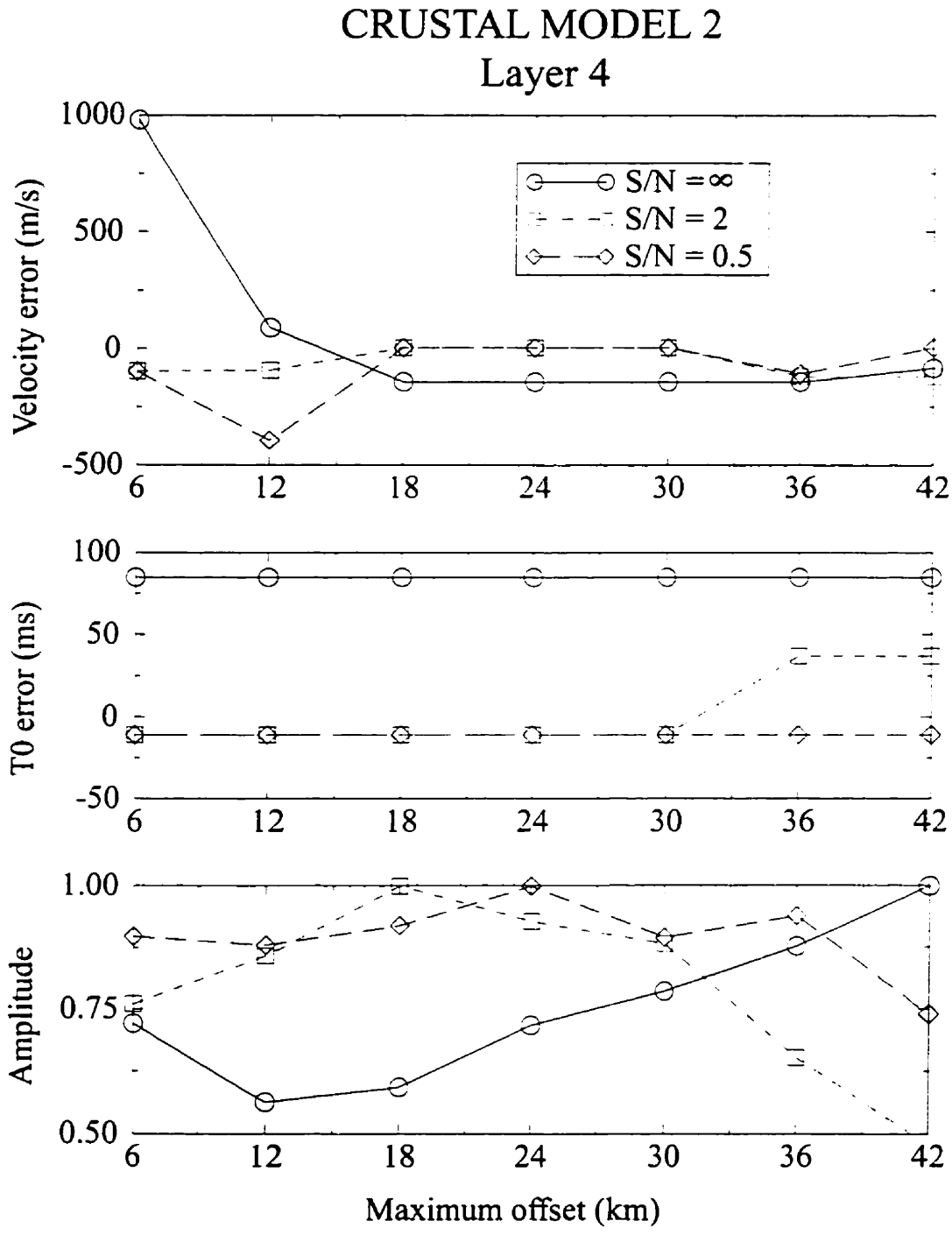

Fig. 5.7 Covariance velocity estimation for layer 4 of model 2 with various S/N.

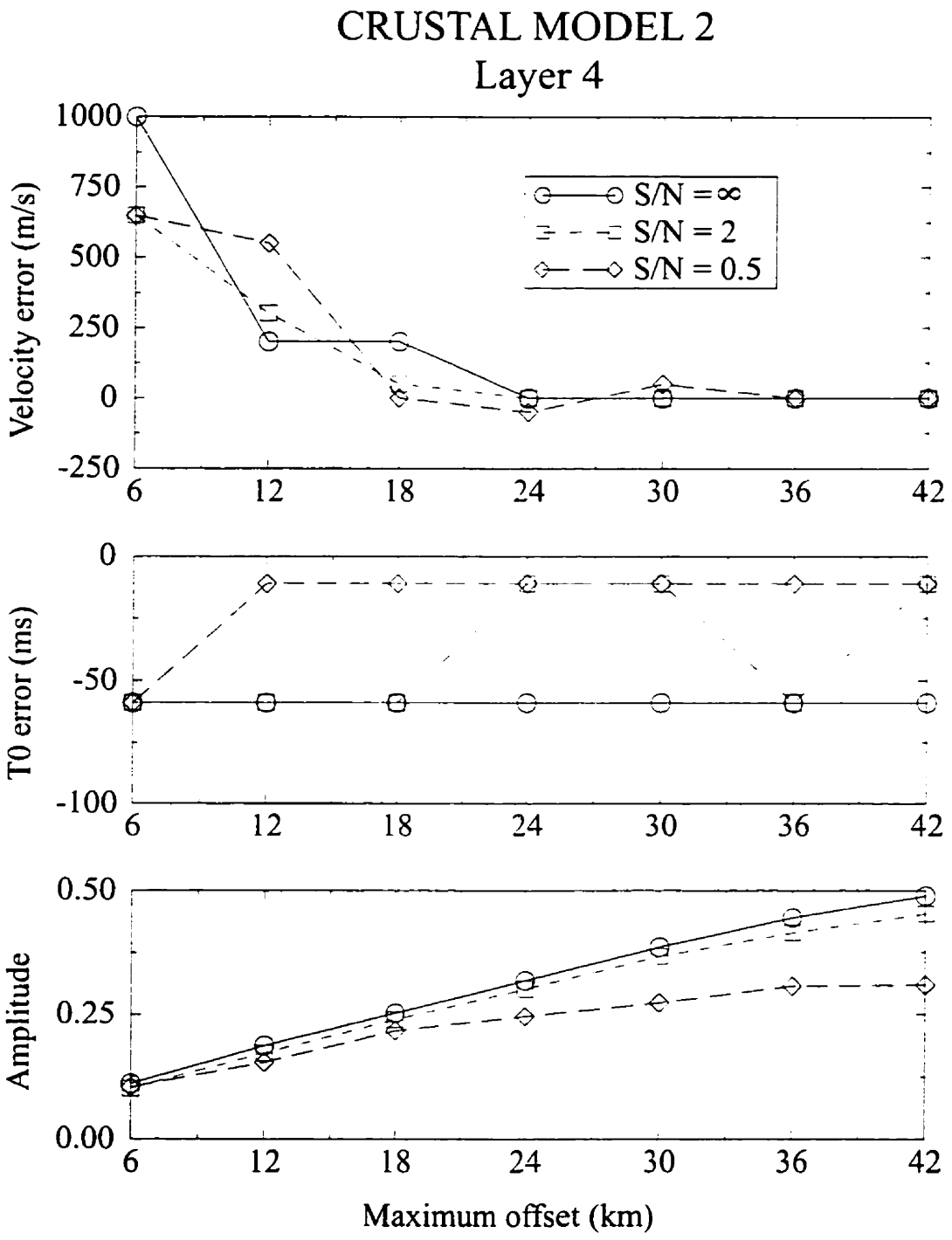

Fig. 5.8 τ-p velocity estimation for layer 4 of model 2 with various S/N.

Having established the optimum offset range based on the errors of the estimated parameters, the resolution of each technique was investigated (Figs. 5.9 to 5.13). To compare the relative performance of the methods at three different offsets each series of plots was normalized to its maximum value and contoured with the same threshold level (with the exception of Fig. 5.13). Figures 5.9 and 5.10 reveal that the covariance method exhibits the highest and the τ - p the lowest resolution. The resolution of the semblance estimator for a maximum offset of 36 km is equal to that of the covariance method with a corresponding offset of 18 km. At greater depth the velocity resolution has decreased as a consequence of a smaller *X/Z* ratio and less pronounced moveouts, but the covariance technique still outperforms the other two (Figs. 5.11 and 5.12). This comparative advantage, however, disappears when the *S/N* ratio is decreased (Fig. 5.13).

Based on the amplitude of the peaks of the velocity spectra and the associated velocity resolution and errors, at least 18 km maximum offset is recommended for crustal seismic reflection studies. The performance of the covariance velocity analysis is expected to exceed that of the semblance and τ - p methods when the *S/N* ratios are high.

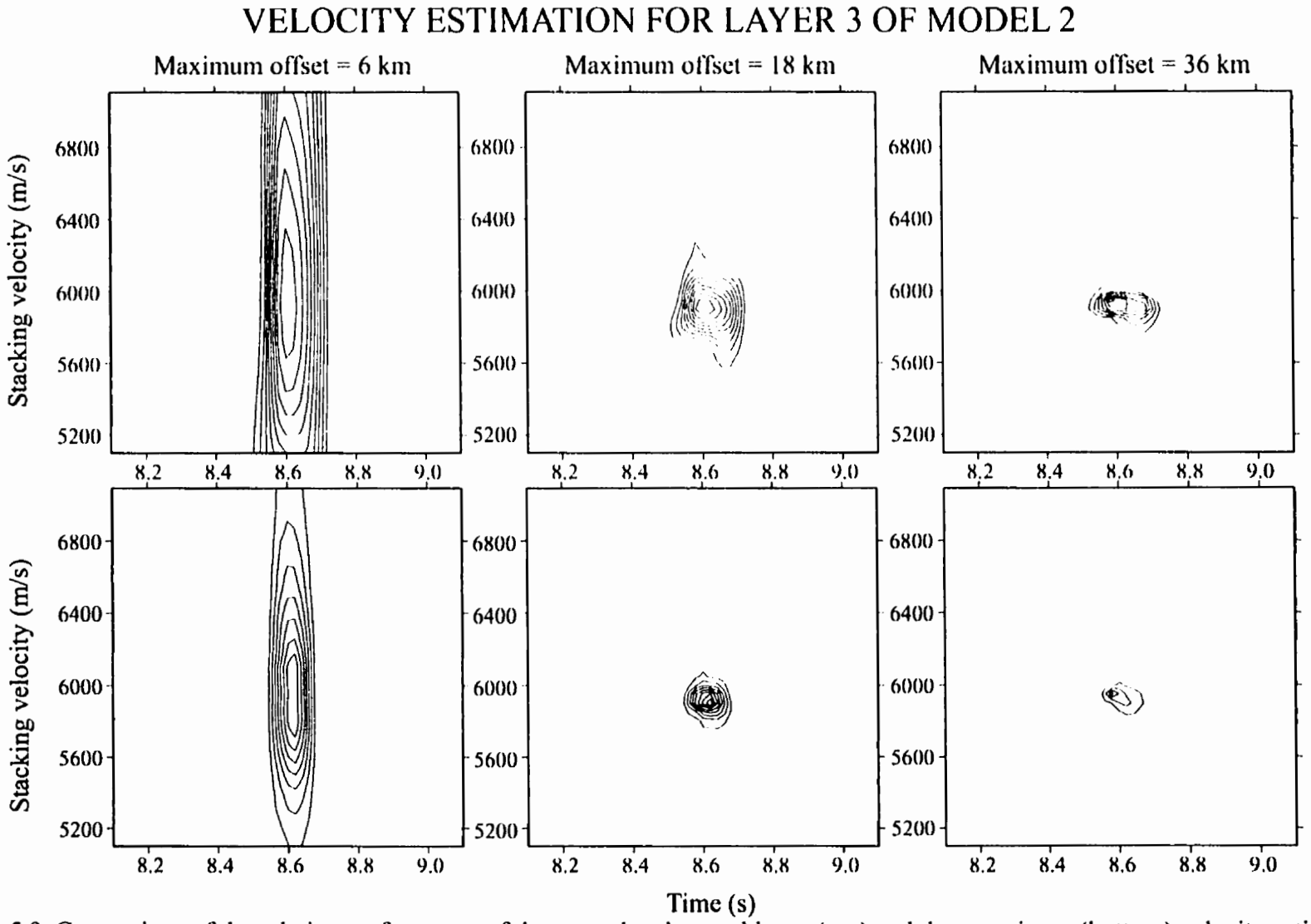

Fig. 5.9 Comparison of the relative performance of the second-order semblance (top) and the covariance (bottom) velocity estimators for layer 3 of model 2 (S/N = 2). Each series of plots is normalized to its maximum value. Threshold = 0.15; C.I. = 0.1.

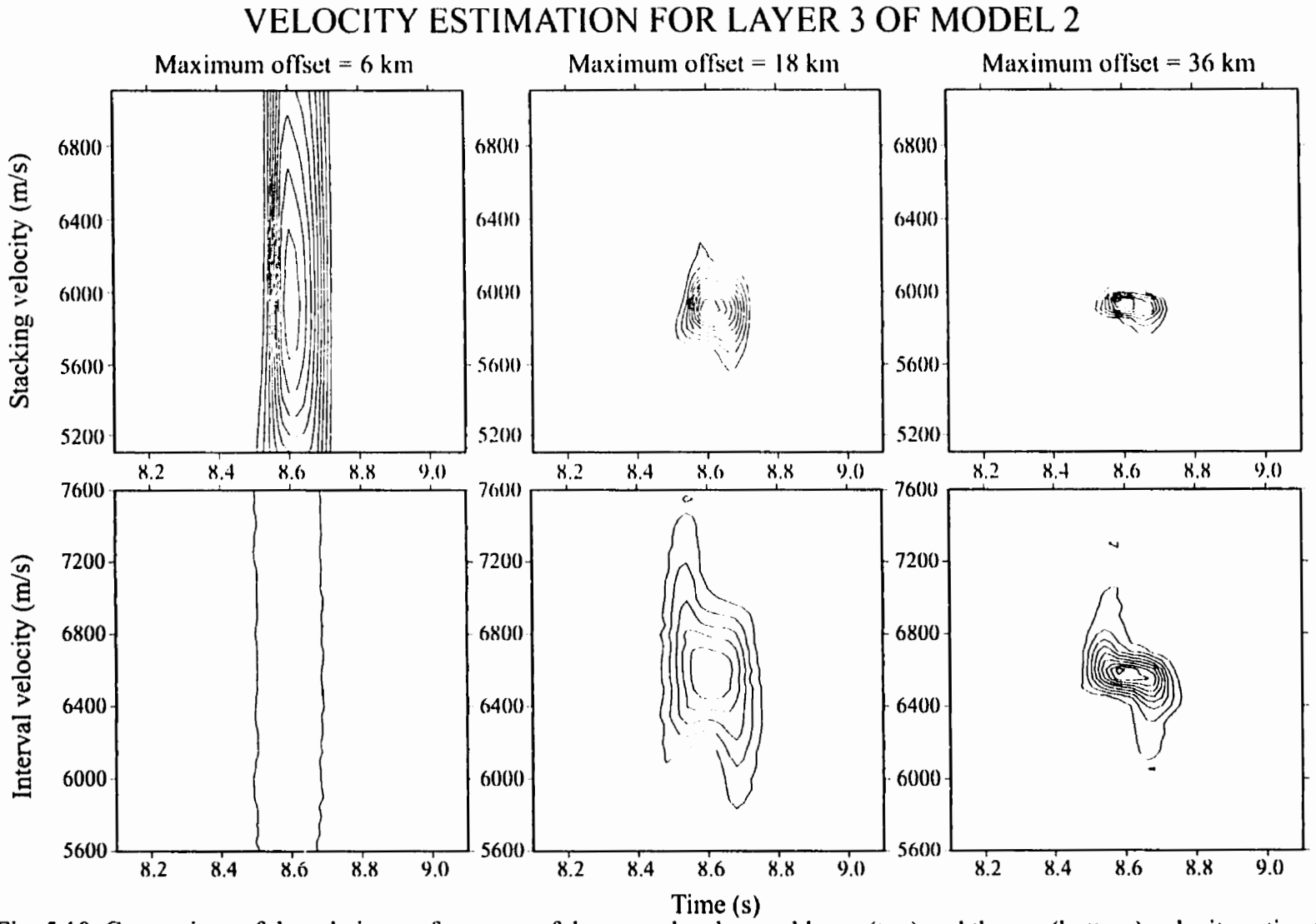

Fig. 5.10 Comparison of the relative performance of the second-order semblance (top) and the τ-p (bottom) velocity estimators for layer 3 of model 2 (S/N = 2). Each series of plots is normalized to its maximum value. Threshold = 0.15; C.I. = 0.1.

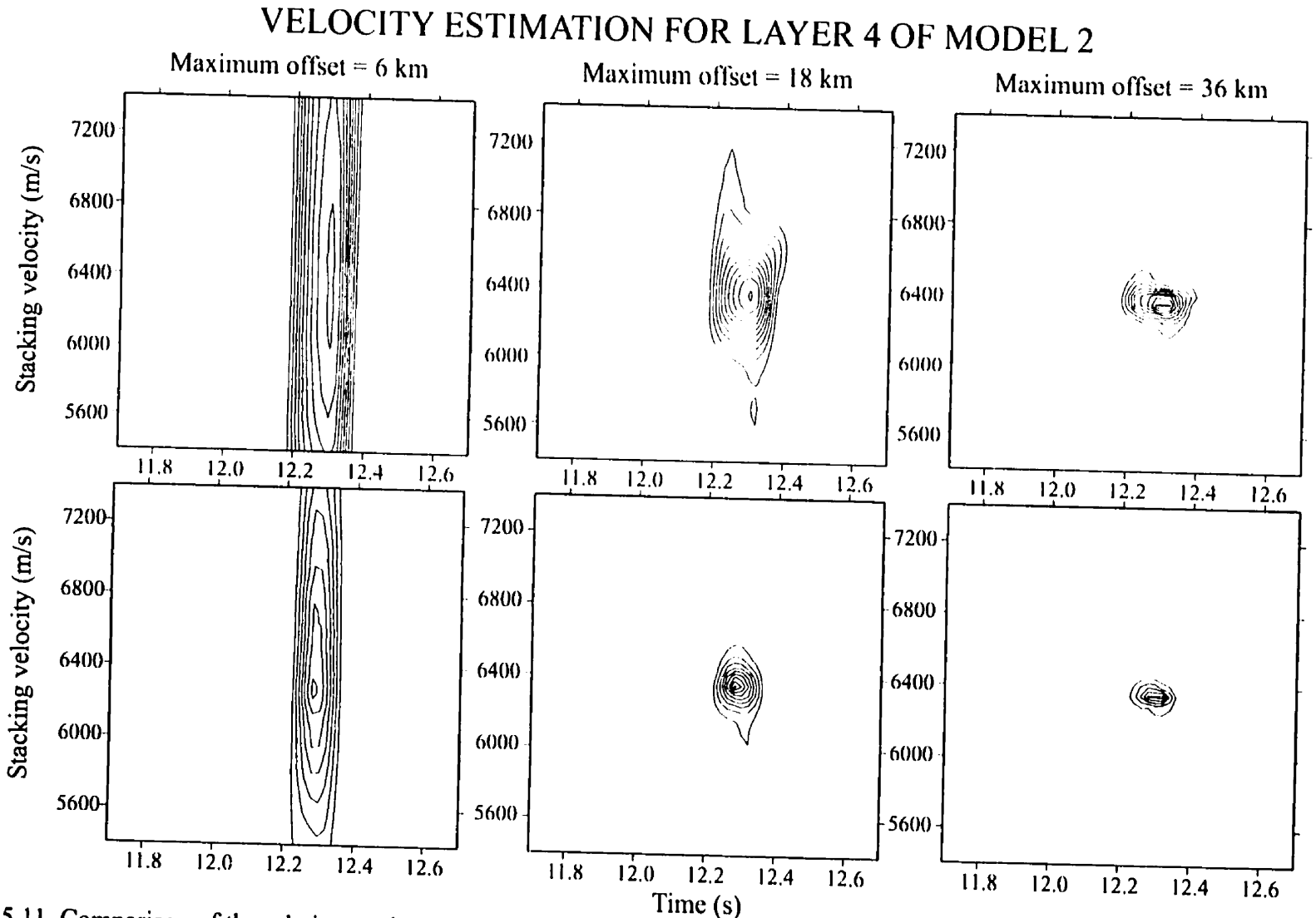

Fig. 5.11 Comparison of the relative performance of the second-order semblance (top) and the covariance (bottom) velocity estimators for layer 4 of model 2 (S/N = 2). Each series of plots is normalized to its maximum value. Threshold = 0.15; C.I. = 0.1.

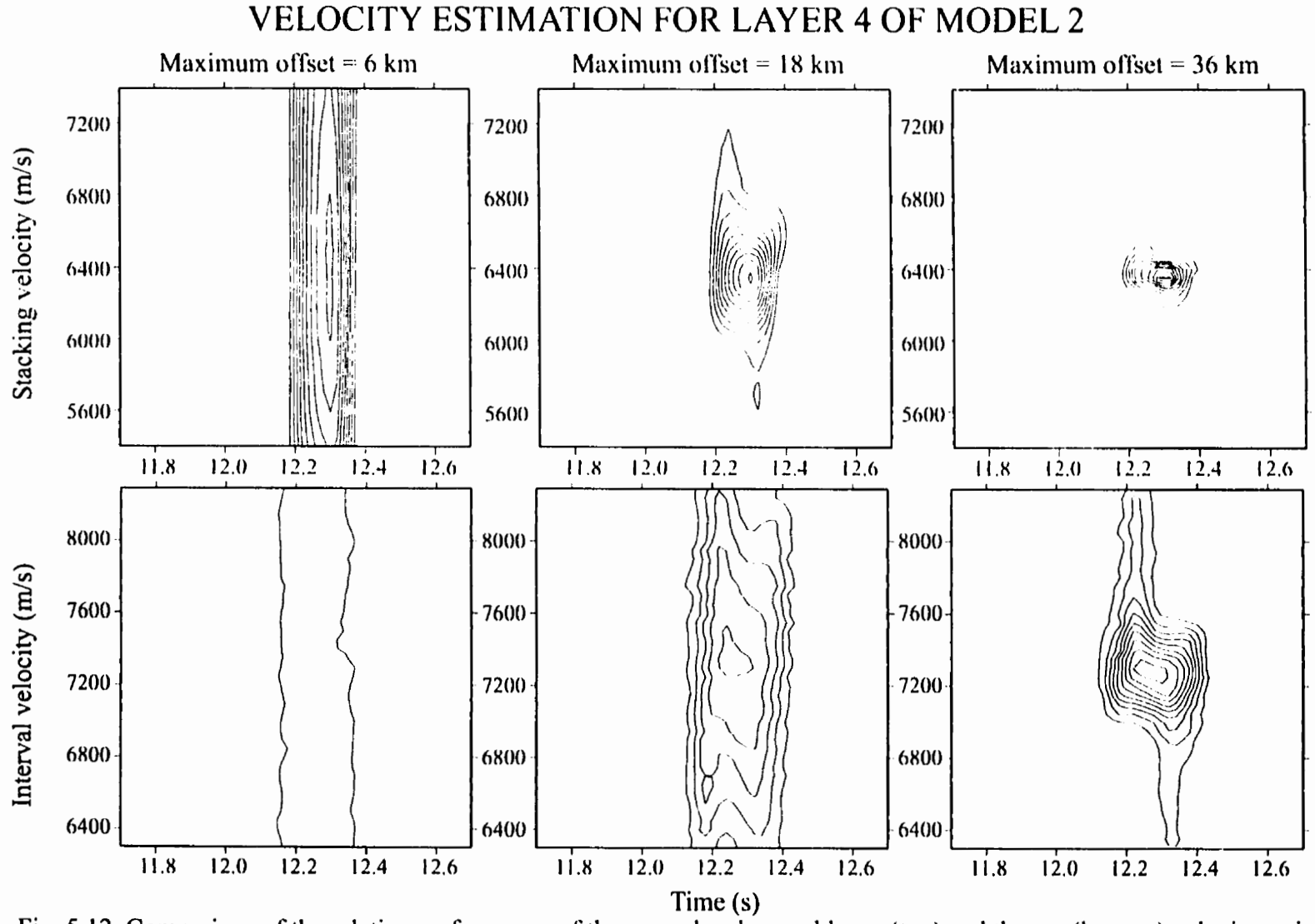

Fig. 5.12 Comparison of the relative performance of the second-order semblance (top) and the τ-p (bottom) velocity estimators for layer 4 of model 2 (S/N = 2). Each series of plots is normalized to its maximum value. Threshold = 0.15; C.I. = 0.1.

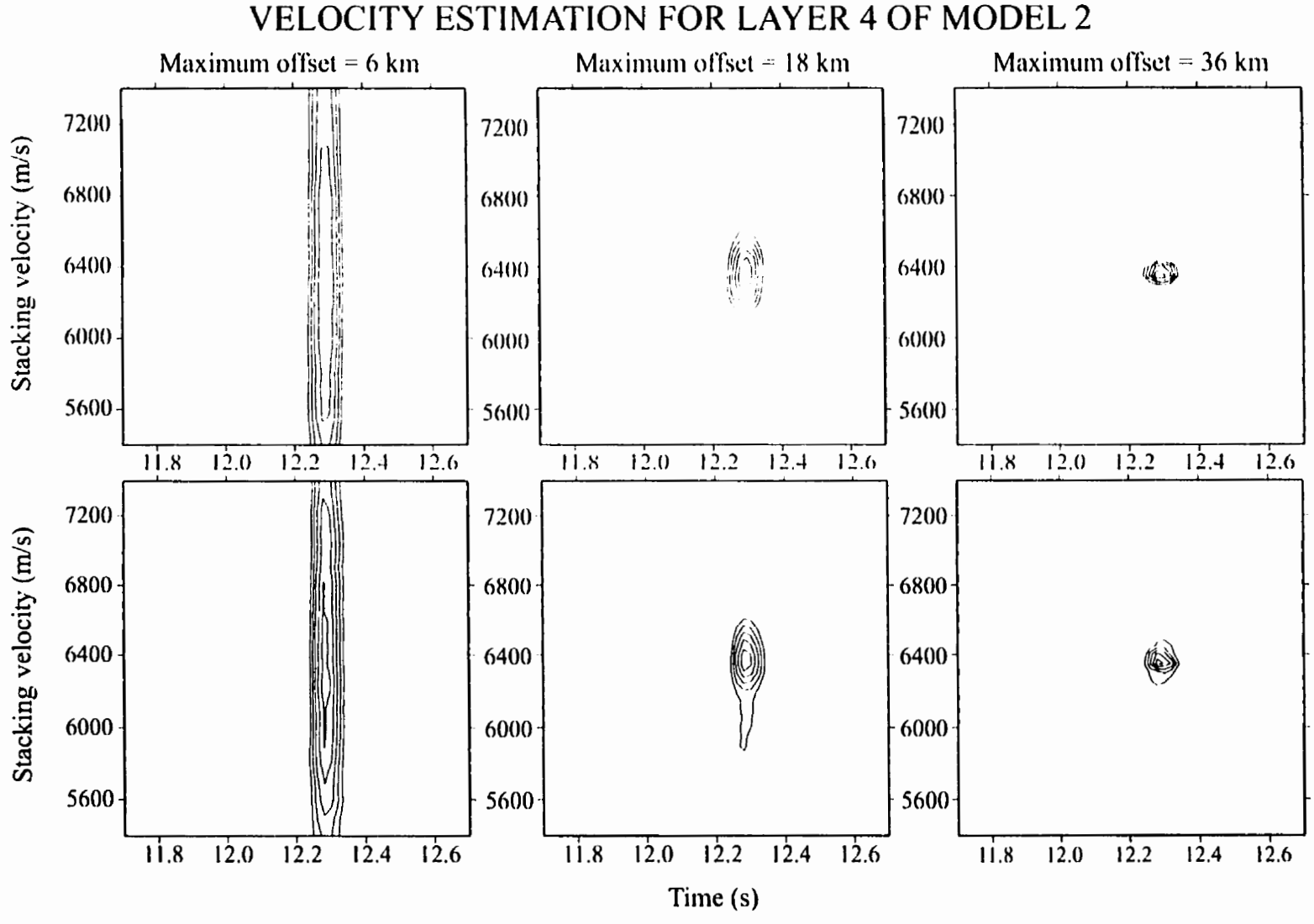

Fig. 5.13 Comparison of the relative performance of the second-order semblance (top) and the covariance (bottom) velocity estimators for layer 4 of model 2 (S/N = 0.5). Each series of plots is normalized to its maximum value. Threshold = 0.5; C.I. = 0.1.

CHAPTER 6

VELOCITY ANALYSIS AND INTERPRETATION OF EXPANDING SPREAD PROFILES

6.1 Velocity analysis

Velocity analysis was carried out in the CMP domain. In order to improve *S/N* ratios, four adjacent CMP gathers were summed together creating super CMP gathers. In addition, effective velocity analysis was also achieved in the common offset stack (COS) domain (Figs. 6.1 and 6.2). Traces were binned by source-receiver separation and then stacked to create COS gathers. Despite a somewhat large lateral averaging of 6 km, a pattern showing events with well defined moveout characteristics and high continuity (B and M1 Fig. 6.1; C and M1 Fig. 6.2), together with zones of strong reflectivity is clearly evident. Velocity spectra calculated at the same CMP location of the ESP and the regional vibroseis survey are shown in Figure 6.3. Velocity resolution is clearly improved when longer offset traces were included, confirming their relatively greater contribution to velocity analysis and their greater ability to influence semblance values. Figure 6.3 also reveals that the shorter spread length results in unrealistically high velocity picks at Moho-level reflections. An additional advantage of the velocity analysis of ESP data over conventionally recorded data is that, due to

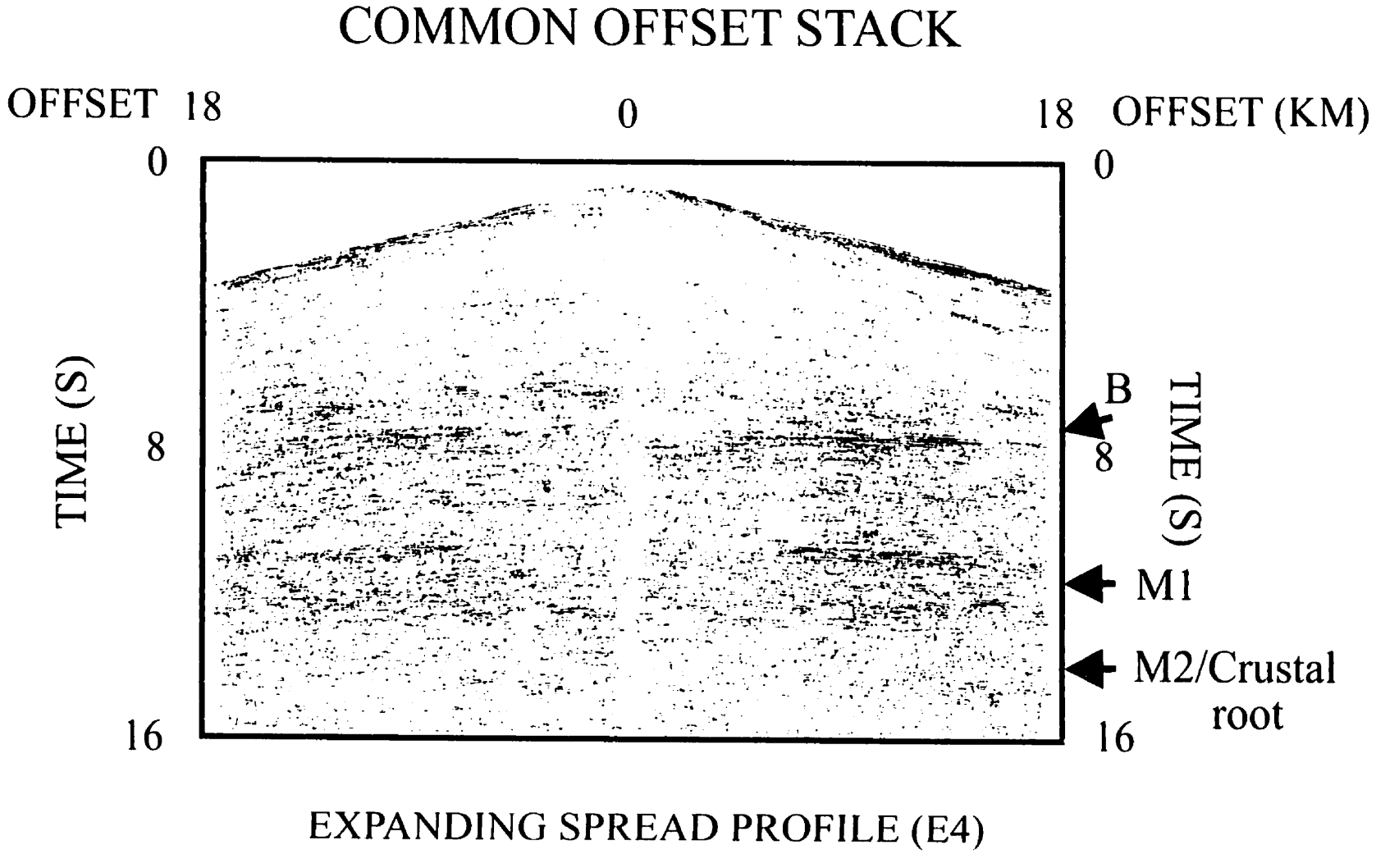

Fig. 6.1 Common offset stack of expanding spread profile E4.

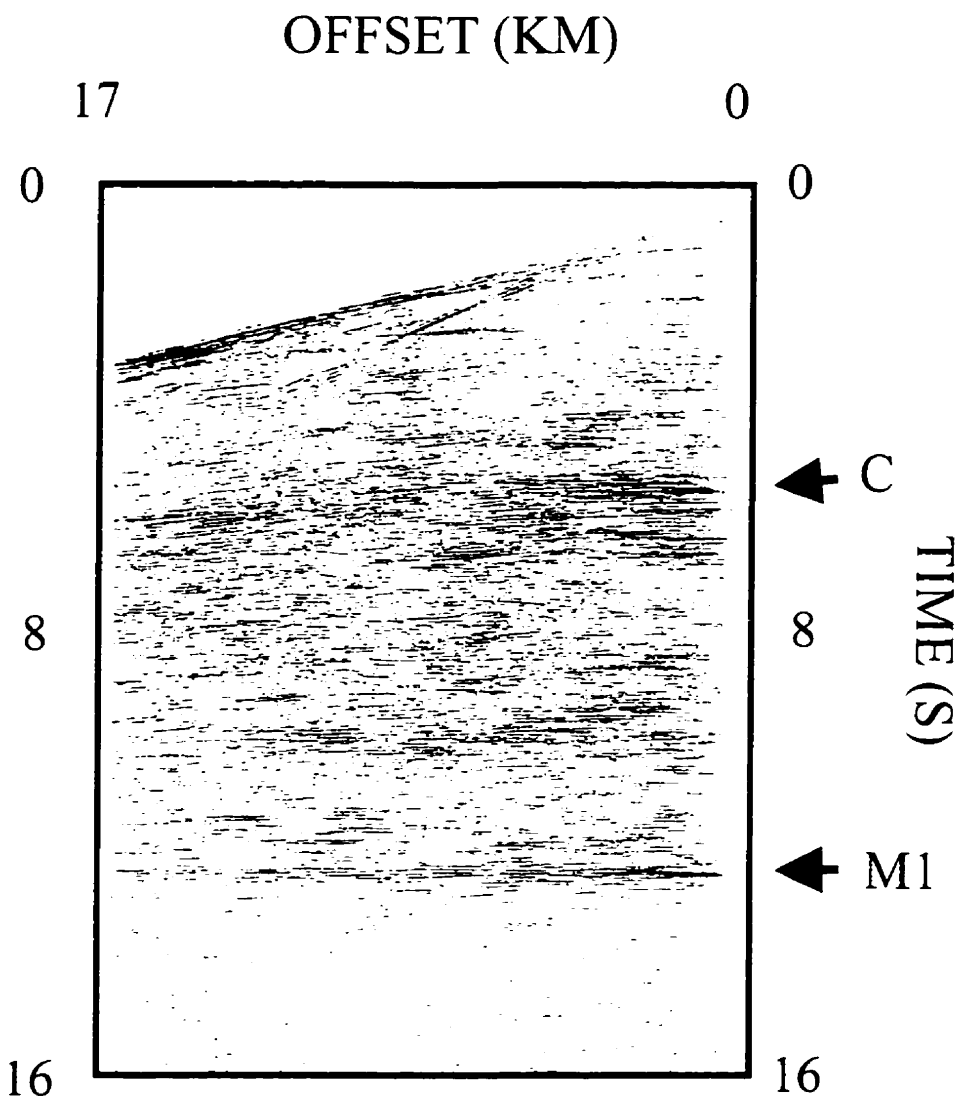

Fig. 6.2 Common offset stack of expanding spread profile E3.

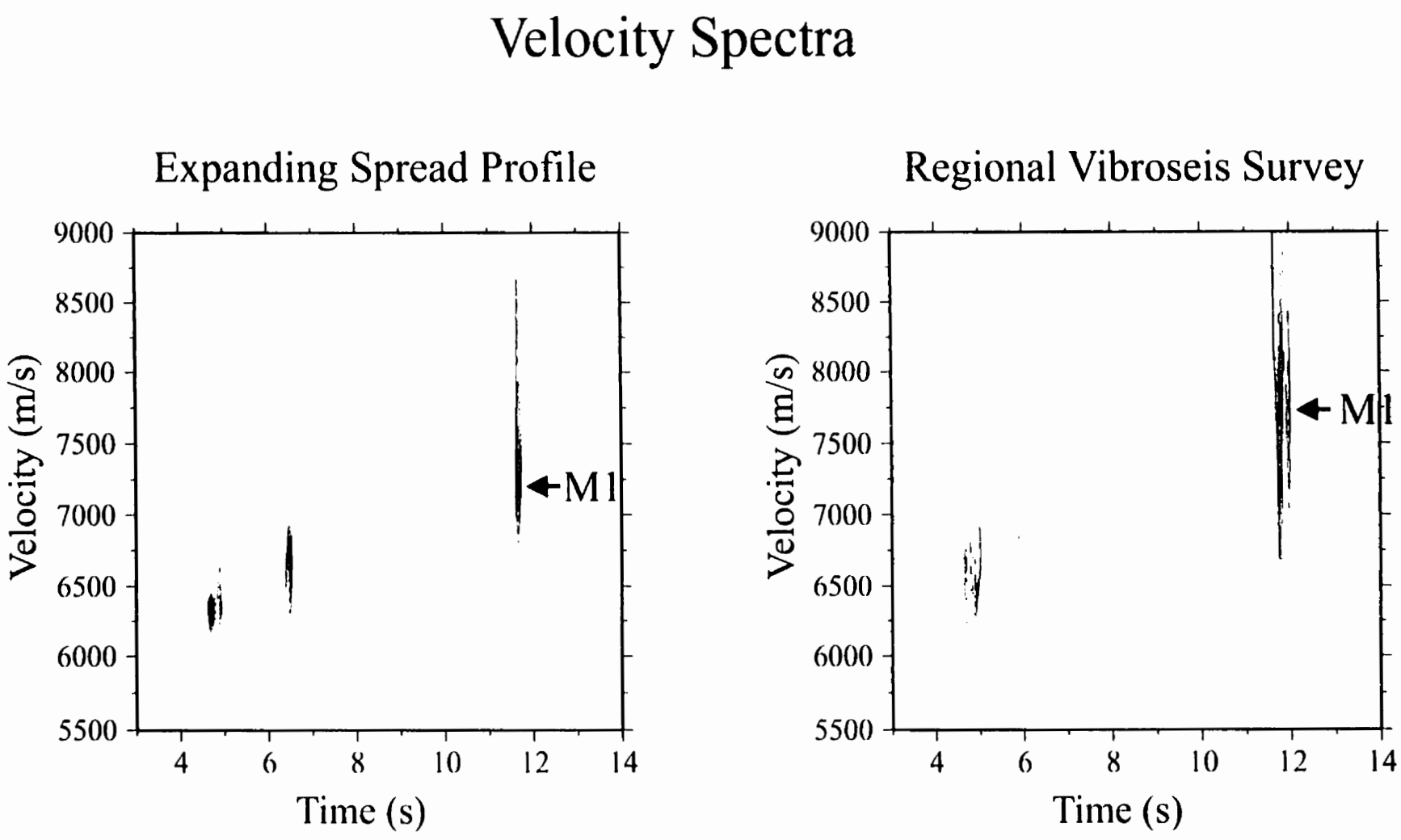

Fig. 6.3 Second-order semblance velocity analysis at the same CMP location of E4 and the regional vibroseis survey. Each plot is normalized to its maximum value. Threshold = 0.3; and C.I. = 0.1.

their recording geometry, the ESP data is less contaminated by direct wave and air-wave coupled ground roll patterns.

All three velocity estimators (Section 5.2) were applied to ESP data. Due to its iterative nature the τ-p analysis was attempted only on selected locations. In order to stabilize the τ-p transformation, composite super CMP gathers were created covering the entire offset range. In general, the covariance method provided the best resolution, especially for lower-crustal events (Fig. 6.4). The value of P was usually in the range of 30 – 60 and $M' = 60$ was used throughout the study. There is a trade-off between high resolution (i.e. large P values) and non-detection of lesser-pronounced peaks (B Fig. 6.4). When a large-amplitude blurred peak dominates the velocity spectra, the value of P had to be further reduced in order to recognize other peaks (Fig. 6.5). It must be noted that the covariance technique did not provide reliable velocity estimation in a low S/N environment even if the semblance method was able to resolve the velocity-depth function.

The τ-p method demonstrates excellent upper- and mid-crustal resolution but reliability of the picks diminishes with greater depth (Fig. 6.6). The resulting velocity-depth structure, however, exhibits excellent correlation with the values derived through semblance analysis (Table 6.1).

Due to its design the ESP data provided an excellent opportunity to take advantage of large offsets for velocity analysis in the different domains. The detailed velocity information arrived in this section was used to stack the ESP data presented in the next section.

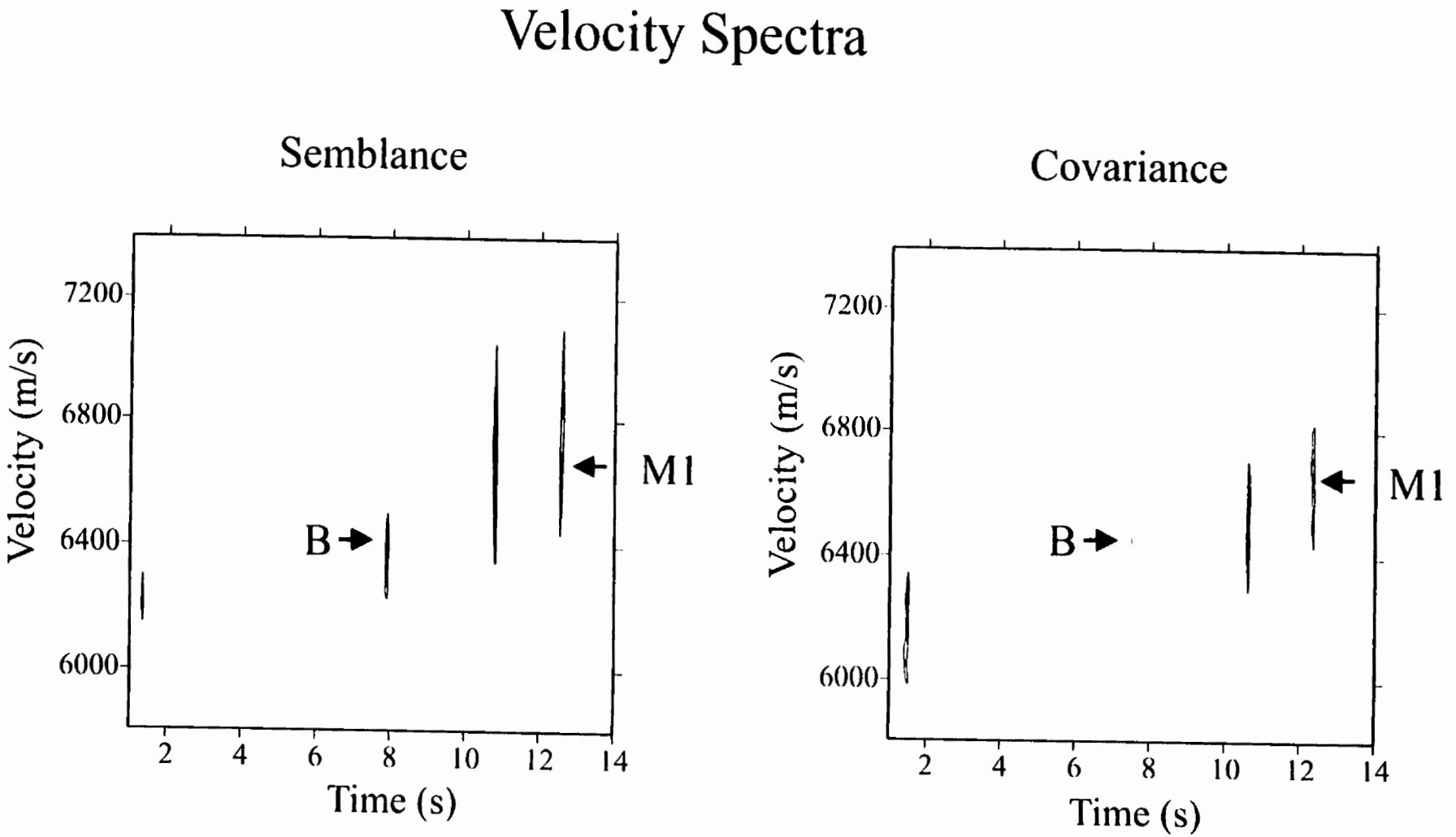

Fig. 6.4 Second-order semblance (left) and covariance (right) velocity analysis at the same super CMP location of E4. Each plot is normalized to its maximum value. Threshold = 0.6; C.I. = 0.1; and P = 60.

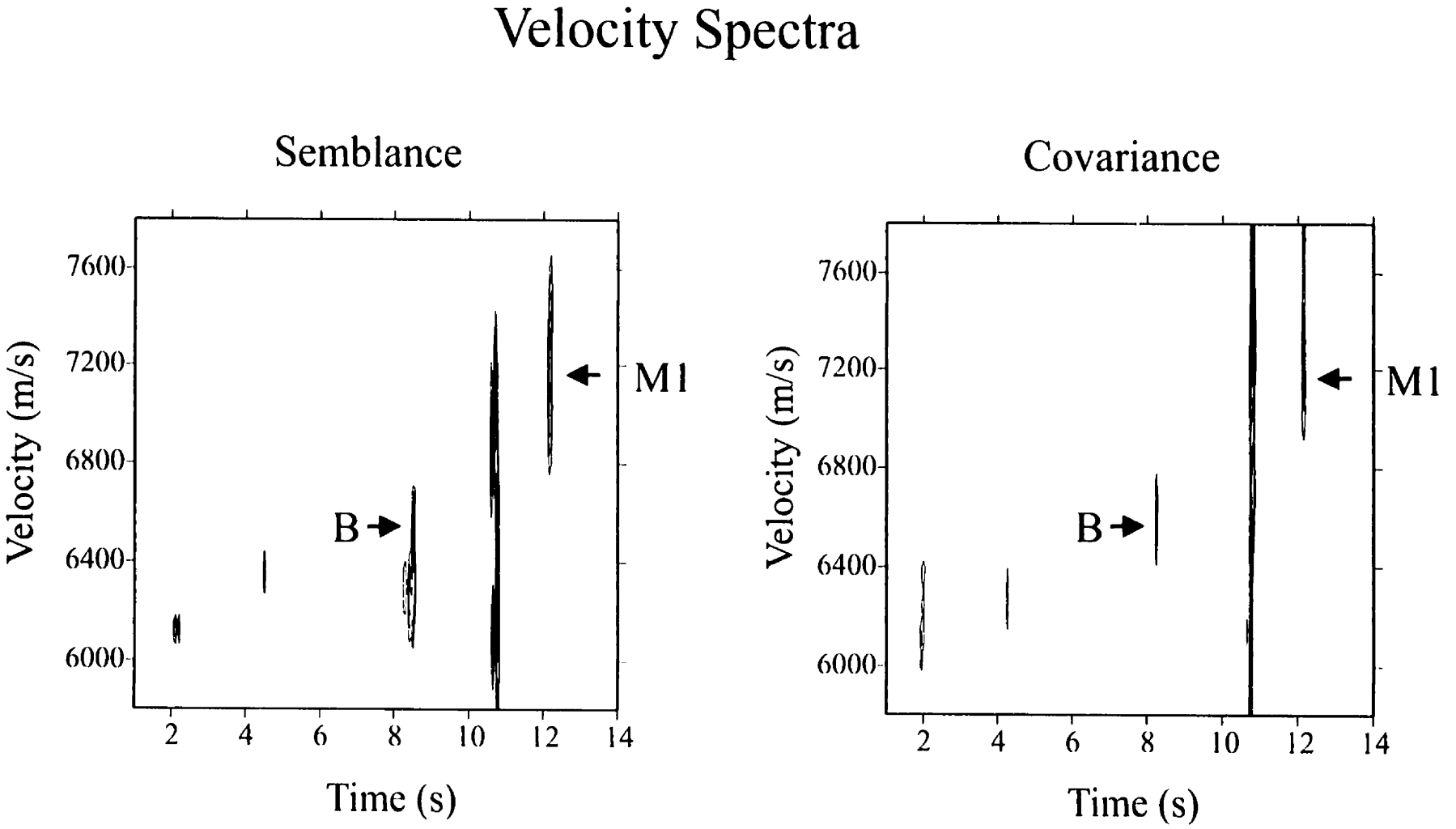

Fig. 6.5 Second-order semblance (left) and covariance (right) velocity analysis at the same super CMP location of E4. Each plot is normalized to its maximum value. Threshold = 0.6; C.I. = 0.1; and P = 15.

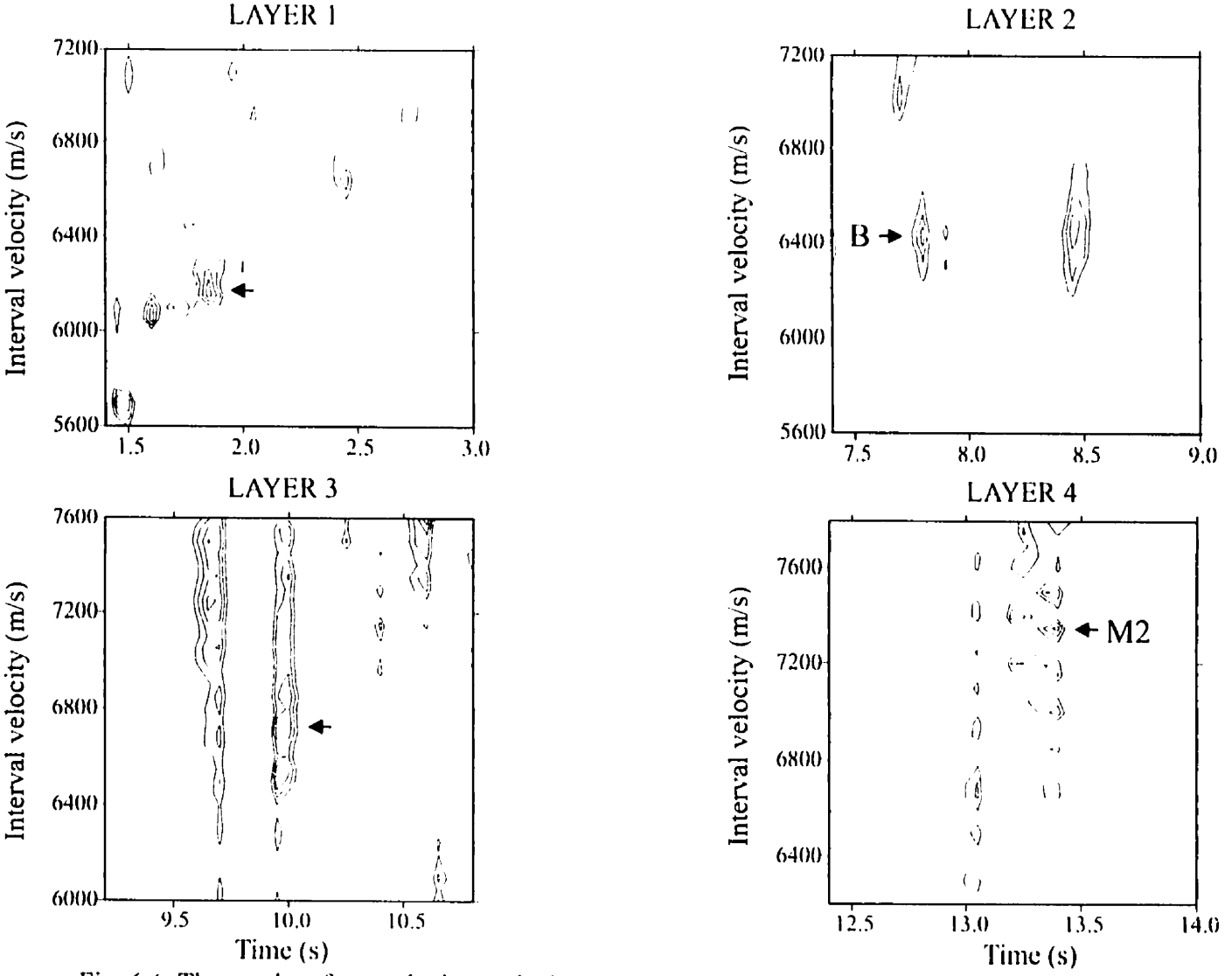

Fig. 6.6 The results of τ-p velocity analysis on a composite super CMP gather of E4 (Table 6.1). Each plot is normalized to its maximum value. Threshold = 0.7; C.I. = 0.1.

Table 6.1 Inversion results of a composite super CMP gather of E4

	Semblance		τ-p	
layer	depth [m]	velocity [m/s]	depth [m]	velocity [m/s]
1	5731	6150	5633	6150
2	25005	6476	24906	6450
3	32163	6627	32142	6700
4	44109	7319	44682	7325

6.2 Interpretation of the expanding spread profiles

Comparing the stacked sections (Figs. 6.7 to 6.10) reveals that, mainly due to the more severe mutes and the special array pattern, the ESP generated reflectivity is less focussed down to 6 s TWT. Below this time, however, the special survey data, under properly selected survey configurations, provides comparable or better images than the regional survey (Bezdan and Hajnal, in press). The continuity and strength of the dominant reflections (e.g. B, N Fig. 6.7; C, M1 Fig. 6.8) are greater on the ESP derived sections. The overall superior quality of the 47-fold E3 (Fig. 6.8) emphasizes the importance of the longer offset recording over higher multiplicity (fold) of the regional survey. In the zone of E4 two types of reflection Moho (see Section 3.2) are evident and these are better imaged on the ESP data (M1 and M2 Fig. 6.7). An additional important contribution of the data from profile E4, collected at the western edge of the recently discovered crustal root (M2 Fig. 6.7) (Lucas et al., 1993), lies in providing clear support for the existence of lithospheric mantle reflections (N Fig. 6.7). These mantle events were first identified by the analysis of an experimental explosive-source based data set (Bezdan and Hajnal, 1996). The clarity of the Moho

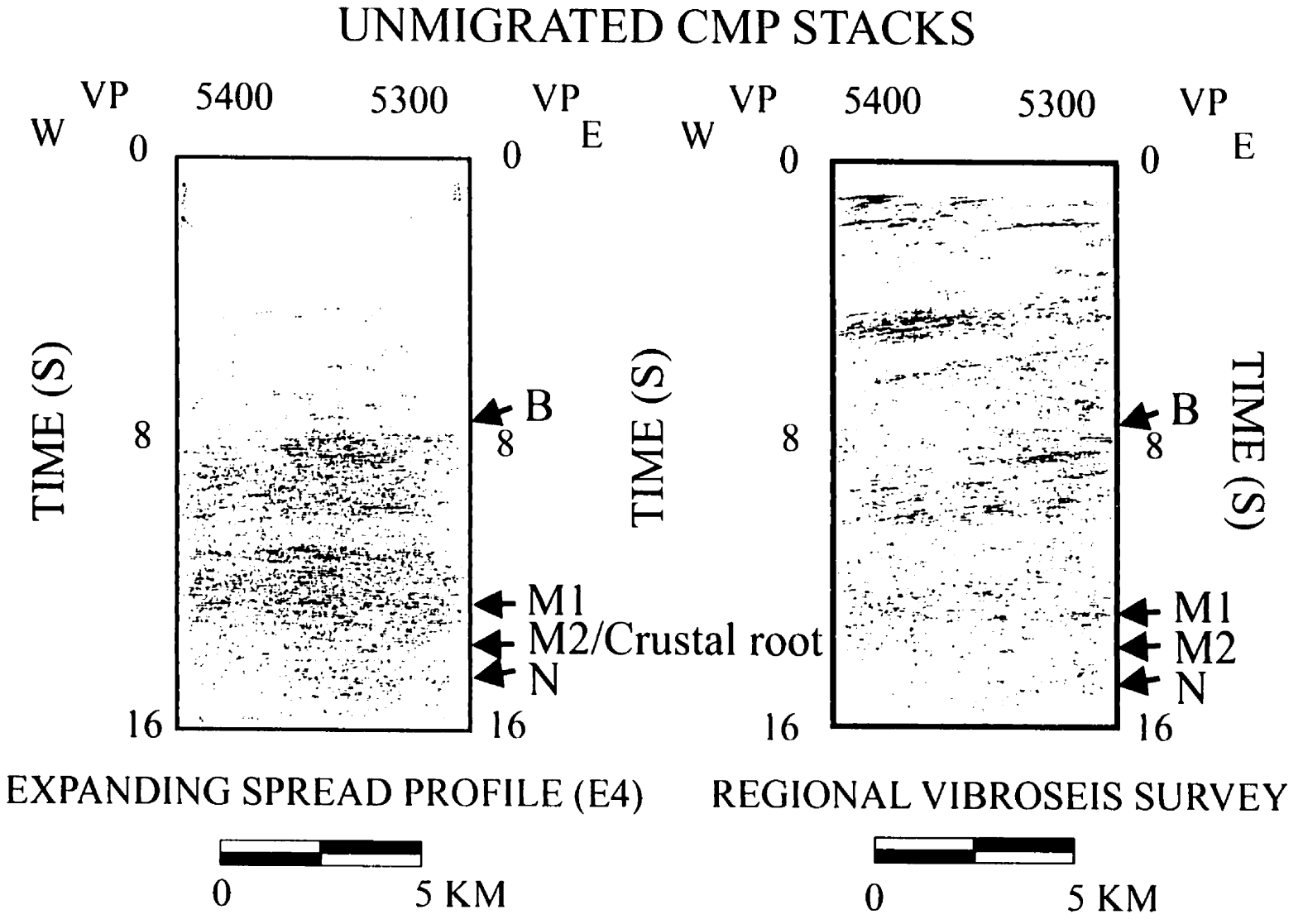

Fig. 6.7 Unmigrated CMP stacks of expanding spread profile E4 and the regional survey (line 9).

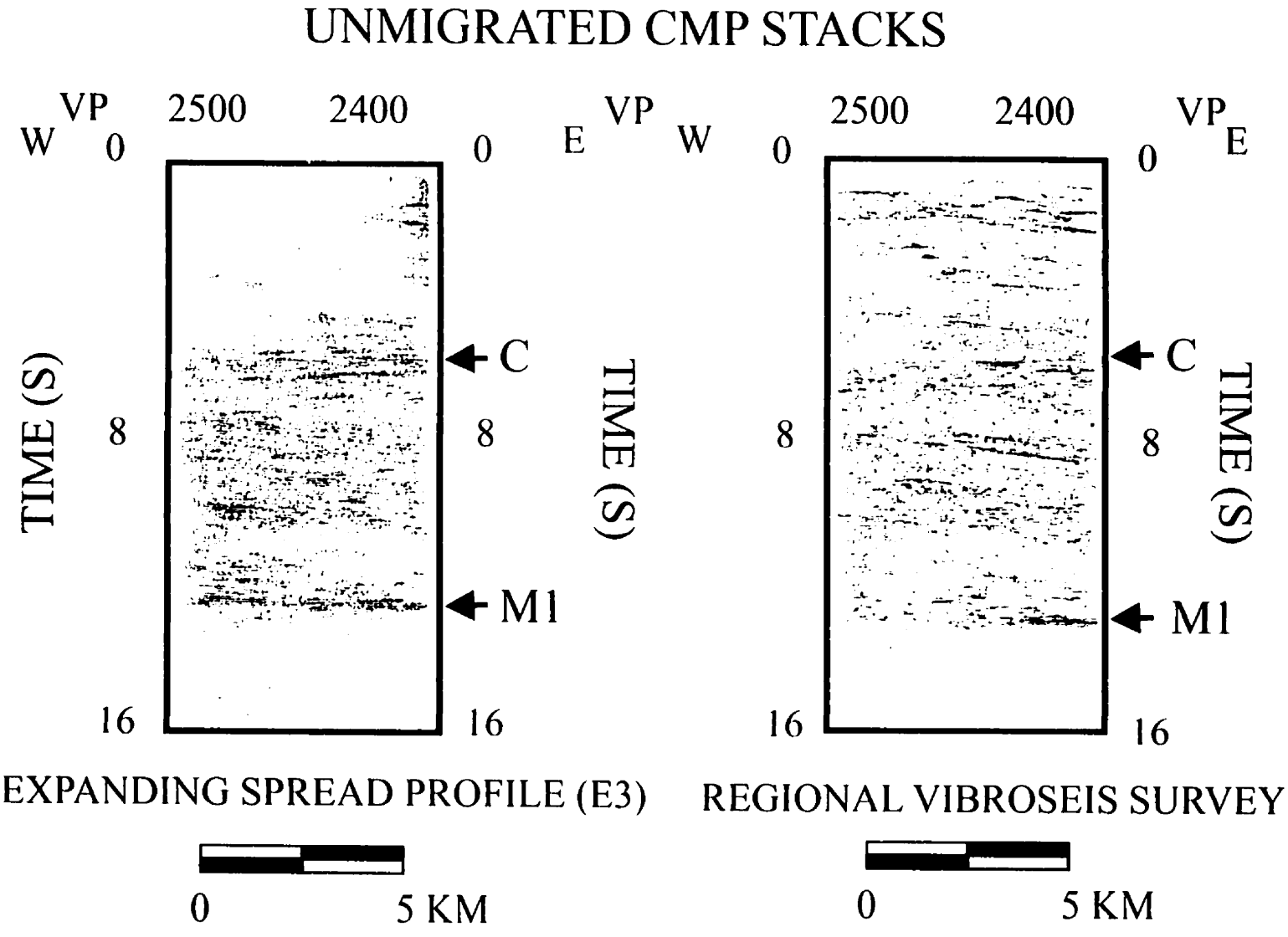

Fig. 6.8 Unmigrated CMP stacks of expanding spread profile E3 and the regional survey (line 9).

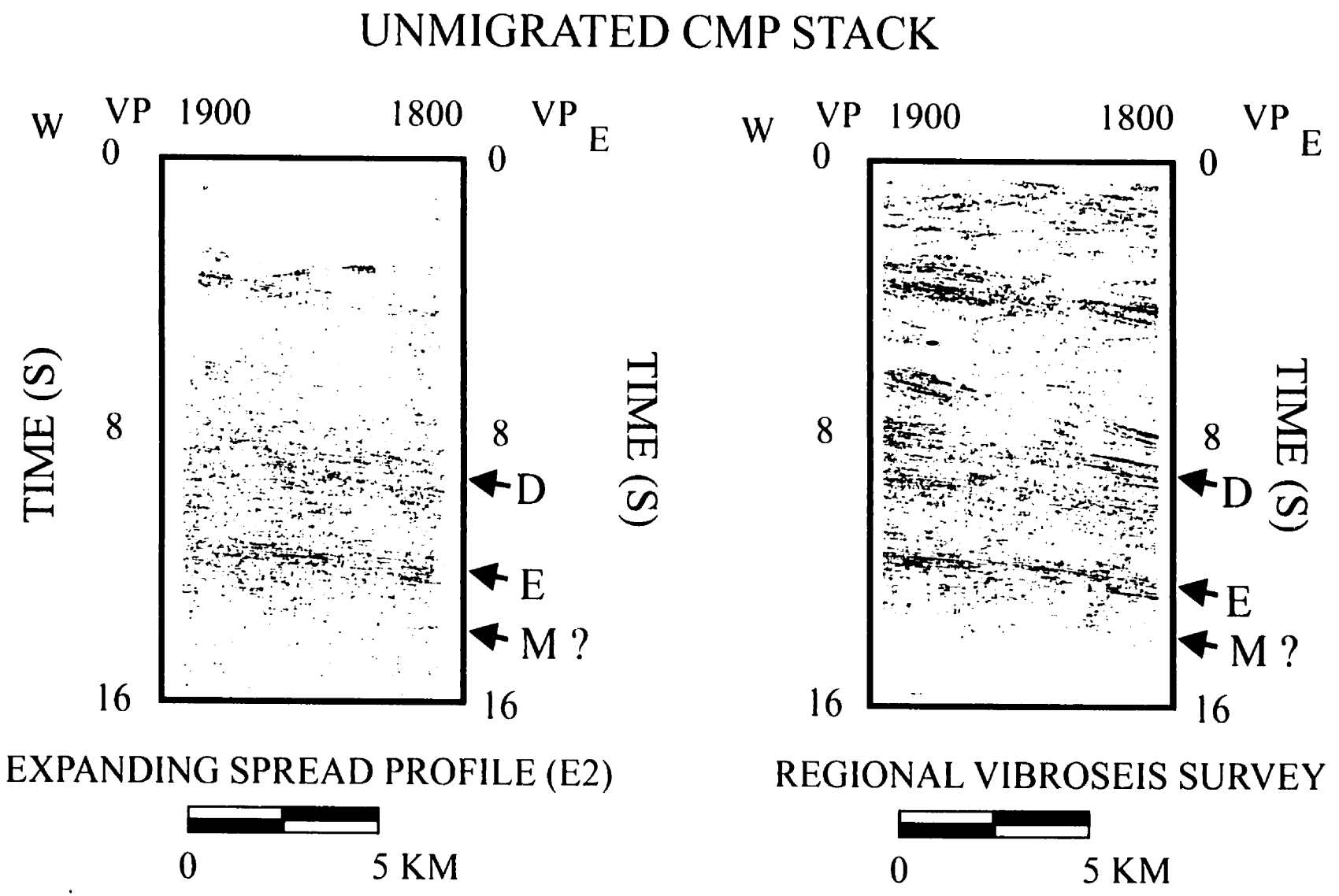

Fig. 6.9 Unmigrated CMP stacks of expanding spread profile E2 and the regional survey (line 3).

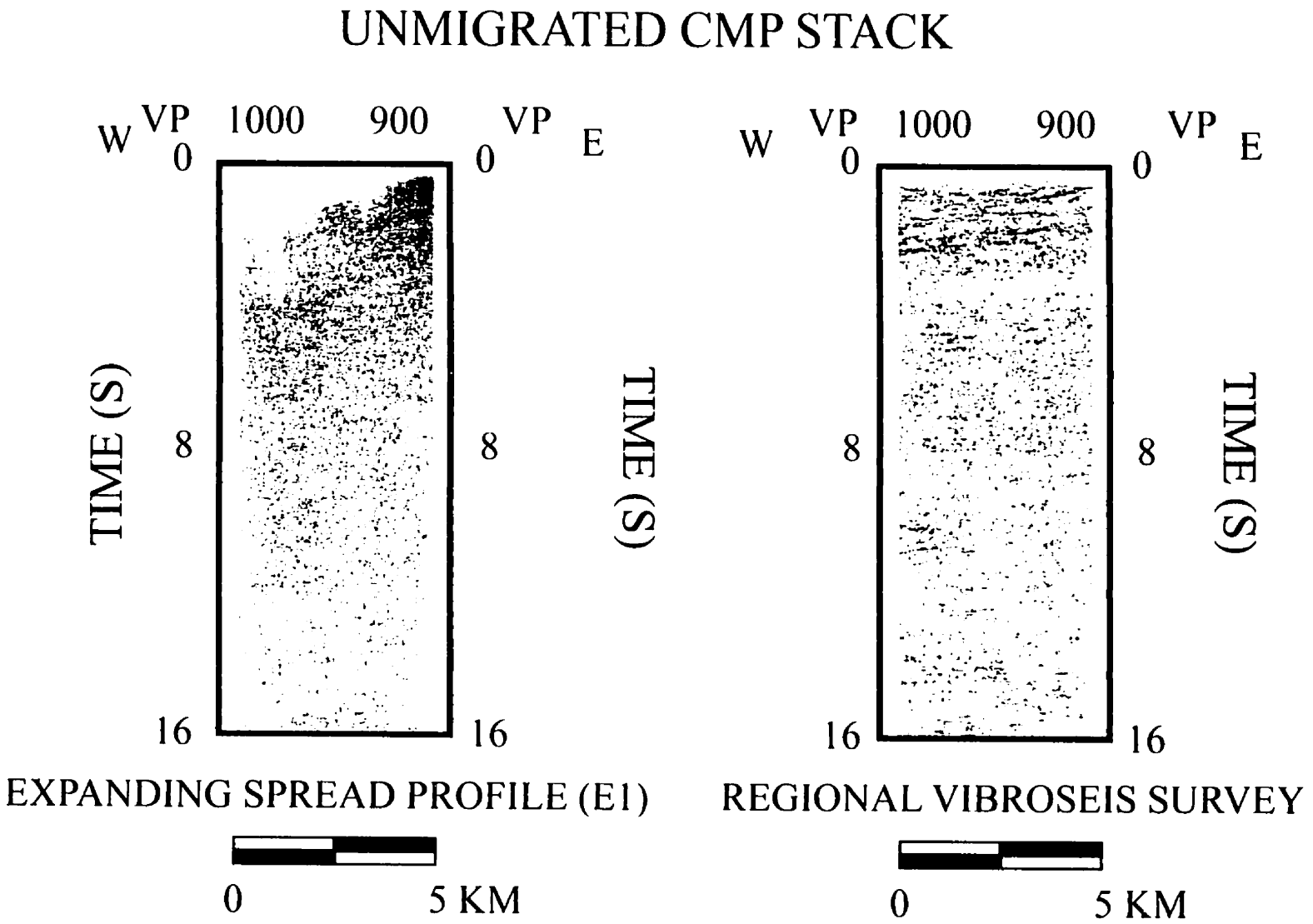

Fig. 6.10 Unmigrated CMP stacks of expanding spread profile E1 and the regional survey (line 2).

reflectivity zones of profiles E3 and E4 again demonstrates the regional variability of the crust-mantle contact along the central region of the Reindeer Zone. They support the suggestion based upon the refraction results (Hajnal et al., 1997) that the lithosphere beneath the collisional belt was an active participant of the tectonic process.

At the intersection of the regional lines 3 and 4 the high amplitude east-dipping zones of reflectivity (D and E Fig. 6.9) dominate both regional and the ESP sections. The Moho reflections were projected below 16 s TWT by the earlier investigations (White et al., 1994). Wide-angle reflection studies show (Németh et al., 1996) that the Moho has a regional reflectivity signature and is dipping to the east (<14 s). This observation is supported by the E2 data (M Fig. 6.9).

The one-sided E1 (Fig. 6.10) was located at the western margin of the Superior craton. The general reflectivity properties of the crust is marginal (White et al., 1994). However, the vibroseis section at the locality of the E1 spread reveals somewhat more coherent reflectivity than the ESP data. These marginal seismic signatures of the E1 profile are a consequence of poor selection of the survey location. The expanding spread was selected in a rather crooked segment of the line which caused unacceptably large scattering of the CMP points leading to great difficulty in stacking the data. In this segment of the LITHOPROBE investigation, Moho was not recognizable by any of the seismic studies. Both the upper- and lower-crust are devoid of coherent reflections.

Comparison of ESP and regional vibroseis data from the 1991 THO seismic reflection survey demonstrates that the ESP data provide more detailed images of the

crust below 6 s TWT. The more accurate velocity model and the contribution of the far-offset traces significantly improve reflection images, especially in the lower crust and upper mantle. Consequently longer offset recording, (e.g. up to 18 km), even at the expense of some reduction of survey fold, may be expected to provide enhancements in the images obtained by standard crustal seismic experiments.

CHAPTER 7

SUMMARY

Comparison of dynamite and vibroseis data from the 1991 THO seismic reflection survey demonstrates that the vibroseis data provide superior images of the crust to mid-crustal depths. However, the explosive data disclose more elaborate images of the lower crust and upper mantle despite its higher noise level due to the low survey fold. In particular, the lateral continuity of the Moho and the structural complexity of the previously identified crustal root are better imaged by the dynamite data. Numerous sub-Moho reflections have been identified on the dynamite based section, mainly in the vicinity of the crustal root of the Archean cored antiform. The advantages of the dynamite source include deeper signal penetration and mapping of a number of previously unrecognized subcrustal reflections. Moreover, the dynamite data also indicate that diffraction patterns, detected at lower crustal and Moho depths, have large apertures and extend to greater two-way traveltimes than were recorded in the vibroseis data. Thus, proper migration of lower crustal reflections requires recording greater traveltimes than were recorded during the 1991 LITHOPROBE vibroseis acquisition program.

Modeling results reveal that velocity estimation becomes more robust and accurate when crustal seismic surveys utilize longer offsets than commonly implemented by standard practice. The covariance method yielded the highest resolution followed by the semblance and the τ - p methods. The resolution of the semblance estimator for a maximum offset of 36 km is equal to that of the covariance method with a corresponding offset of 18 km. At greater depth the velocity resolution has decreased as a consequence of a smaller X/Z ratio and less pronounced moveouts, but the covariance technique still outperforms the other two. This comparative advantage, however, disappears when the S/N ratio is decreased.

The advantages provided by the long-offset data acquisition include increased S/N ratio and a greater number of traces with sufficiently large moveouts which improve velocity resolution, especially below mid-crustal depths. To achieve similar advantages in a regional crustal reflection survey would require the adoption of longer spread lengths than those presently implemented in standard data acquisition procedures.

References:

Alabi, A.O., Camfield, P.A. and Gough, D.I., 1975. The North American Central Plains conductivity anomaly. Geophys. J. R. astr. Soc., 43: 815-833.

Al-Chalabi, M., 1973. Series approximation in velocity and traveltime computations. Geophys. Prosp., 21: 783-795.

Al-Chalabi, M., 1974. An analysis of stacking, average, and interval velocities over a horizontally layered ground. Geophys. Prosp., 22: 458-475.

Al-Chalabi, M., 1979. Velocity determination from seismic reflection data. Developments in Geophysical Exploration Methods-1. A.A. Fitch (ed.), Applied Science Publishers, Barking: pp. 1-68.

Al-Chalabi, M., 1994. Seismic velocities-a critique. First Break, 12: 589-596.

Alkhalifah, T., 1997. Seismic data processing in vertically inhomogeneous TI media. Geophysics, 62: 662-675.

Alkhalifah, T. and Tsvankin, I., 1995. Velocity analysis for transversely isotropic media. Geophysics, 60: 1550-1566.

Al-Yahya, 1989. Velocity analysis by iterative profile migration. Geophysics, 54: 718-729.

BABEL Working Group, 1991. Evidence for Early Proterozoic plate tectonics from seismic reflection profiles in the Baltic shield. Nature, 348: 34-38.

Baird, D.J., Knapp, J.H., Steer, D.N., Brown, L.D. and Nelson, K.D., 1995. Upper mantle reflectivity beneath the Williston basin, phase change Moho, and the origin of intracratonic basins. Geology, 23: 431-434.

Bancroft, J.C. and Geiger, H.D., 1994. Equivalent offset CRP gathers. SEG Extended Abstracts, Los Angeles: 672-675.

Baragar, W. R.A. and Scoates, R.F.J., 1981. The Circum-Superior belt: a Proterozoic plate margin. In: A. Kroner (ed.) Precambrian Plate Tectonics. Elsevier, Amsterdam: pp. 297-330.

Barnes, A.E., 1994. Moho reflectivity and seismic signal penetration. In: R.M. Clowes and A.G. Green (eds.), Seismic Reflection Probing of the Continents and their Margins. Tectonophysics, 232: 299-307.

Bezdan, S. and Hajnal, Z., 1996. Coincident vibroseis and dynamite surveys across the western flank of the Trans-Hudson Orogen. In: D.J. White, J. Ansorge, T.J. Bodoky and Z. Hajnal (eds.), Seismic Reflection Probing of the Continents and their Margins. Tectonophysics, 264: 101-110.

Bezdan, S. and Hajnal, Z., Expanding spread profiles of the Trans-Hudson Orogen. In: W. Mooney and S. Klemperer (eds.), Deep Seismic Profiling of the Continents. Tectonophysics (in press).

Bickel, S.H., 1990. Velocity-depth ambiguity of reflection traveltimes. Geophysics, 55: 266-276.

Bickford, M.E., Collerson, K.D., Lewry, J.F., Van Schmus, W.R. and Chiarenzellli, 1990. Proterozoic collisional tectonism in the Trans-Hudson Orogen, Saskatchewan. Geology, 18: 14-18.

Bishop, T.N., Bube, R.T., Cutler, R.T., Langan, R.T., Love, P.L., Resnick, J.R., Shuey, R.T., Spindler, D.A. and Wyld, H.W., 1985. Tomographic determination of velocity and depth in laterally varying media. Geophysics, 50: 903-923.

Bolshix, C.F., 1956. Approximate model for the reflected wave traveltime curve in multilayered media. Applied Geophysics, 15: 3-14 (in Russian).

Brittan, J. and Warner, M., 1996. Seismic velocity, heterogeneity, and the composition of the lower crust. In: D.J. White, J. Ansorge, T.J. Bodoky and Z. Hajnal (eds.), Seismic Reflection Probing of the Continents and their Margins. Tectonophysics, 264: 249-259.

Brown, R.L., Carr, S.D., Johnson, B.J., Coleman, V.J., Cook, F.A. and Varsek, J.L., 1992. The Monashee decollement of the southern Cordillera: A crustal-scale shear zone linking the Rocky Mountain Foreland belt to lower crust beneath accreted terranes. In: K.R. McClay (ed.), Thrust Tectonics. Chapman and Hall, London: pp. 357-364.

Byun, B.S. and Corrigan, D., 1990. Seismic traveltime inversion for transverse isotropy. Geophysics, 55: 192-200.

Calvert, A.J., Sawyer, E.P., Davis, W.G. and Ludden, J.N., 1995. Archean subduction inferred from seismic images of a mantle suture in the Superior Province. Nature, 375: 670-674.

Carrion, P.M., 1988. Velocity analysis from large offset seismic records. Pure and Applied Geophys., 126: 1-26.

Castle, R.J., 1994. A theory of normal moveout. Geophysics, 59: 983-999.

Collerson, K.D., Lewry, J.F., Bickford, M.E. and Van Schmus, W.R., 1990. Crustal evolution of the buried Precambrian of southern Saskatchewan: implications for diamond exploration. In: L.S. Beck and C.T. Harper (eds.), Modern Exploration Techniques. Sask. Geol. Soc. Spec. Pap., 10: 150-165.

Cook, F.A. and Varsek, J.L., 1994. Orogen-scale decollements. Reviews of Geophysics, 32: 37-60.

Cross, G.M. and Knoll, M.D., 1991. Diffraction-based velocity estimates from optimum offset seismic data. Geophysics, 56: 2070-2079.

Damotte, B. and Bois, C., 1990. Near-vertical vibroseis versus large-offset dynamite seismic reflection profiling: example of the ECORS northern France profile. In: J.H. Leven, D.M. Finlayson, C. Wright, J.C. Dooley and B.L.N. Kennett (eds.), Seismic Reflection Probing of the Continents and their Margins. Tectonophysics, 173: 95-106.

de Bazelaire, E., 1988. Normal moveout revisited-Inhomogeneous media and curved interfaces. Geophysics, 53: 142-158.

de Bazelaire, E. and Viallix, J.R., 1992. Normal moveout in focus. 54th Ann. Mtg., Eur. Assoc. Exp. Geophys., Expanded Abstracts: 174-175.

de Bazelaire, E. and Viallix, J.R., 1994. Normal moveout in focus. Geophys. Prosp., 42: 477-499.

DEKORP Research Group, represented by Flueh, E.R., Klaeschen, D. and Meissner, R., 1990. Wide-angle vibroseis data from the western Rhenish Massif. In: J.H. Leven, D.M. Finlayson, C. Wright, J.C. Dooley and B.L.N. Kennett (eds.), Seismic Reflection Probing of the Continents and their Margins. Tectonophysics, 173: 83-93.

Deregowski, S.M., 1990. Common-offset migrations and velocity analysis. First Break, 8: 225-234.

Diebold, J.B. and Stoffa, P.L., 1981. The travel-time equation, τ - p mapping and inversion of common mid-point data. Geophysics, 46: 238-254.

Dix, C.H., 1955. Seismic measurement from surface measurements. Geophysics, 20: 68-86.

Doherty, S.M. and Claerbout, J.F., 1976. Structure independent velocity analysis. Geophysics, 41: 850-881.

Duren, R.E. and Morris, S.V., 1992. Sideswipe removal via null steering. Geophysics, 57: 1623-1632.

Dürbaum, H., 1954. Zur Bestimmung von Wellengeschwindigkeiten aus reflexions-seismischen Messungen. Geophys. Pros., 1: 125-139.

Eaton, D.W., Milkereit, B., Ross, G.M., Kanasewich, E.R., Geis, W., Edwards, D.J., Kelsch, L. and Varsek, J., 1995. Lithoprobe basin-scale seismic profiling in central Alberta: influence of basement on the sedimentary cover. Bull. of Can. Petroleum Geology, 43: 65-77.

Flack, C. and Warner, M., 1990. Three-dimensional mapping of seismic reflections from the crust and upper mantle, northwest of Scotland. Tectonophysics, 173: 469-481.

Fowler, S.R., White, R.S., Spence, G.D. and Westbrook, G.K., 1989. The Hatton Bank continental margin-II. Deep structure from two-ship expanding spread profiles. Geophysical Journal, 96: 295-309.

González-Serrano, A. and Claerbout, J.F., 1984. Wave-equation velocity analysis. Geophysics, 49: 1432-1456.

Green, 1981. Results of a sesimic reflection survey across the fault zone between the Thompson nickel belt and the Churchill tectonic province northern Manitoba. Can. J. Earth Sci., 18: 13-25.

Green, A.G., Hajnal, Z. and Weber, W., 1985. An evolutionary model of the Churchill Province and the western margin of the Superior Province in Canada and the north-central United States. Tectonophysics, 116: 281-322.

Hajnal, Z. and Sereda, I.V., 1981. Maximum uncertainty of interval velocity estimates. Geophysics, 46: 1543-1547.

Hajnal, Z., Fowler, C.M.R., Mereu, R.F., Kanasewich, E.R., Cumming, G.L., Green, A.G. and Mair, A., 1984. An initial analysis of the Earth's crust under the Williston Basin. J. Geophys. Res., 89: 9381-9400.

Hajnal, Z., Lucas, S., White, D., Lewry, J., Bezdan, S., Stauffer, M.R. and Thomas, M.D., 1996. Seismic reflection images of high-angle faults and linked detachments in the Trans-Hudson Orogen. Tectonics, 15: 427-439.

Hajnal, Z., Németh, B., Clowes, R.M., Ellis, R.M., Spence, G.D., Burianyk, M.J.A., Asudeh, I., White, D.J. and Forsyth, D.A., 1997. Mantle involvement in lithospheric collision: Seismic evidence from the Trans-Hudson Orogen, western Canada. Geophys. Res. Lett., 24: 2079-2082.

Hoffman, P., 1989. Precambrian geology and tectonic history of North America In: A.W. Bally and A.R. Palmer (eds.), The geology of North America - An overview. Geol. Soc. Am., Boulder, Colorado: pp. 447-512.

Hubral, P. and Krey, T., 1980. Interval velocities form seismic reflection time measurement. Society of Exploration Geophysicists: 203 p.

Jervis, M., Sen, M.K. and Stoffa, P.L., 1996. Prestack migration velocity estimation using non-linear methods. Geophysics, 60: 138-150.

Jin, S. and Madariaga, R., 1993. Background velocity inversion with a genetic algorithm. Geophys. Res. Lett., 20: 93-96.

Kanasewich, E.R., Hajnal, Z., Green, A.G., Cumming, G.L., Mereu, R.F., Clowes, R.M., Morel-à-l'Hussier, P., Chiu, S., Macrides, C.G., Shahriar, M. and Congram, A.M., 1987. Seismic studies in the crust under the Williston Basin. Can. J. Earth Sci., 24: 2160-2171.

Katz, S., 1991. Asymptotically linear velocity analysis with high resolution in time domain. Geophysics, 56: 1840-1848.

Késmarky, I., 1977. Estimation error of interval velocities and the geological model. Geophys. Trans., 24: 63-74.

Key, C.S. and Smithson, S.B., 1990. New approach to seismic-reflection event detection and velocity determination. Geophysics, 55: 1057-1069.

Kirlin, L., 1992. The relationship between semblance and eigenstucture velocity estimators. Geophysics, 57: 1027-1033.

Klasner, J.S. and King, E.R., 1986. Precambrian basement geology of North and South Dakota. Can. J. Earth Sci., 23: 1083-1102.

Krey, T.C., 1989. The non-uniqueness of interval velocities from moveout velocities. Geophysics, 54: 1209-1211.

Landa, E., Beydoun, W. and Tarantola, A., 1989. Reference velocity estimation from prestsack waveforms: Coherency optimization by simulated annealing. Geophysics, 54: 984-990.

Landa, E., Thore, P., Sorin, V. and Koren, Z., 1991. Interpretation of velocity estimates from coherency inversion. Geophysics, 56: 1377-1383.

Leckie, D.A., Kjarsgaard, B.A., Bloch, J., McIntyre, D., McNeil, D., Stasiuk, L. and Heaman, L., 1997. Emplacement and reworking of cretaceous, diamond-bearing, crater facies kimberlite of central Saskatchewan, Canada. GSA Bulletin, 109: 1000-1020.

Lewry, J.F., 1981. Lower Proterozoic arc-microcontinent collisional tectonics in the western Churchill Province. Nature, 294: 69-72.

Lewry, J.F. and Collerson, K.D., 1990. The Trans-Hudson Orogen: extent, subdivisions and problems. In: J.F. Lewry and M.R. Stauffer (eds.), The Early Proterozoic Trans-Hudson Orogen of North America. Geol. Assoc. Can. Spec. Pap., 37: 1-14.

Lewry, J.F. and Stauffer, M.R. (eds.), 1990. The Early Proterozoic Trans-Hudson Orogen of North America. Geol. Assoc. Can. Spec. Pap., 37: 505p.

Lewry, J.F.,Thomas, D.J., Macdonald, R. and Chiarenzelli, J., 1990. Structural relations in accreted terranes of the Trans-Hudson Orogen, Saskatchewan: telescoping in a collisional regime? In: J.F. Lewry and M.R. Stauffer (eds.), The Early Proterozoic Trans-Hudson Orogen of North America. Geol. Assoc. Can. Spec. Pap., 37: 75-94.

Lewry, J.F., Hajnal, Z., Green, A., Lucas, S.B., White, D., Stauffer, M.R., Ashton, K. E., Weber, W. and Clowes, R., 1994. Structure of a Paleoproterozoic continent-continent collision zone: a LITHOPROBE seismic reflection profile across the Trans-Hudson Orogen, Canada. In: R.M. Clowes and A.G. Green (eds.), Seismic Reflection Probing of the Continents and their Margins. Tectonophysics, 232: 143-160.

Ligget, W.S., 1972. Passive sonar: Fitting models to multiple time series. In: Proc. NATO ASI Signal Processing, Loughborough, England: pp. 327-345.

Lines, L., 1993. Ambiguity in analysis of velocity and depth. Geophysics, 58: 596-597.

Lucas, S.B., Green, A., Hajnal, Z., White, D., Lewry, J., Ashton, K., Weber, W. and Clowes, R., 1993. Deep seismic profile across a Proterozoic collision zone: surprises at depth. Nature, 363: 339-342.

Lucas, S.B., White, D., Hajnal, Z., Lewry, J., Green, A., Clowes, R., Zwanzig, H., Ashton, K., Scheidewitz, D., Stauffer, M., Norman, A., Williams, P.F. and Spence, G., 1994. Three-dimensional structure of the Trans-Hudson Orogen, Canada. In: R.M. Clowes and A.G. Green (eds.), Seismic Reflection Probing of the Continents and their Margins. Tectonophysics, 232: 161-167.

Malovichko, A.A., 1978. A new representation of the traveltime curve of reflected waves in horizontally layered media. Applied Geophysics, 91: 47-53 (in Russian).

Marschall, R., 1975. Einige Probleme bei der Benutzung grosser Schuss-Geophon-Abstnde und deren Anwendung auf Unter-schiessungen: Ph.D. thesis, Leoben.

May, B.T. and Straley, D.K., 1979. Higher-order moveout spectra. Geophysics, 44: 1193-1207.

McBride, J.H., Lindsey, G.A., Hobbs, R.W., Snyder, D.B. and Totterdell, I.J., 1993. Some problems in velocity analysis for marine deep seismic profiles. First Break, 11: 345-356.

McMechan, G.A. and Ottolini, R., 1980. Direct observation of a p - τ curve in a slant stacked wave field. Bull. of Seis. Soc. Am., 70: 775-789.

Minshull, T.A., White, R.S., Mutter, J.C., Buhl, P., Detrick, R.S., Williams, C.A. and Morris, E., 1991. Crustal structure at the Blake Spur fracture zone from expanding spread profiles. J. Geophys. Res., 96: 9955- 9984.

Morel-à-l'Hussier, P., Green, A.G. and Pike, C.J., 1987. Crustal refraction surveys across the Trans-Hudson Orogen/Williston basin of south central Canada. J. Geophys. Res., 92: 6403-6420.

Musgrave, A.W., 1962. Application of the expanding reflection spread. Geophysics, 27: 981-993.

Nelson, K.D., Baird, D.J., Walters, J.J., Hauck, M., Brown, L.D., Olivier, J.E., Ahern, J.L., Hajnal, Z., Jones, A.G. and Sloss, L.L., 1993. Trans-Hudson Orogen and Williston Basin beneath northeastern Montana and northern North Dakota: New COCORP deep profiling results. Geology, 21: 447-450.

Németh, B., Hajnal, Z. and Lucas, S.B., 1996. Moho signature from wide-angle reflections: preliminary results of the 1993 Trans-Hudson Orogen refraction experiment. In: D.J. White, J. Ansorge, T.J. Bodoky and Z. Hajnal (eds.), Seismic Reflection Probing of the Continents and their Margins. Tectonophysics, 264: 111-121.

Neidell, N.S. and Taner, M.T., 1971. Semblance and other coherency measures for multi-channel data. Geophysics, 36: 482-497.

Nowroozi, A.A., 1990. Interpretation of seismic reflection records: direct calculation of interval velocities and layer thicknesses from traveltimes. Pure and Applied Geophys., 133: 103-115.

Ross, W.S., 1994. The velocity-depth ambiguity in seismic travel-time data. Geophysics, 59: 830- 843.

Sheriff, R.E., 1991. Encyclopedic dictionary of exploration geophysics. Society of Exploration Geophysicists: 376 p.

Schoenberg, M. and Muir, F., 1989. A calculus for finely layered anisotropic media. Geophysics, 54: 581-589.

Schultz, P.S., 1982. A method for direct estimation of interval velocities. Geophysics, 47: 1657-1671.

Shah, M.P. and Levin, F.K., 1973. Gross properties of time-distance curves. Geophysics, 38: 643-656.

Sorin, V., 1994. Nonuniqueness of velocity determination for one type of layered model. Geophysics, 59: 161-164.

Stauffer, M.L., 1984. Manikewan: an early Proterozoic ocean in central Canada, its igneous history and orogenic closure. Precambrian Res., 25: 257-281.

Steer, D.N., Brown, L.D., Knapp, J.H. and Baird, D.J., 1996. Comparison of explosive and vibroseis source energy penetration during COCORP deep seismic profiling in the Williston Basin (COCORP explosive-vibroseis comparison). Geophysics, 61: 211-221.

Stoffa, P.L. and Buhl, P., 1979. Two-ship multichannel seismic experiments for deep crustal studies: expanded spread and constant offset profiles. J. Geophys. Res., 84: 7645-7660.

Stoffa, P.L., Wood, W.T., Shipley, T.H., Moore, G.F., Nishiyama, E., Botelho, M.A.B., Taira, A., Tacoma, H. and Sahara, K., 1992. Deepwater high-resolution expanding spread profiles in the Nancy Trough. J. Geophys. Res., 97: 1687-1713.

Stork, C. and Clayton, R.W., 1991. Linear aspects of tomographic velocity analysis. Geophysics, 56: 483-495.

Taner, M.T. and Koehler, F., 1969. Velocity spectra-digital computer derivation and application of velocity functions. Geophysics, 34: 859-881.

Tarantola, A., 1984. Inversion of seismic reflection data in acoustic approximation. Geophysics, 49: 1259-1266.

Thomas, M.D., Sharpton, V.L. and Grieve, R.A.F., 1987. Gravity patterns and Precambrian stucture in the North American Central Plains. Geology, 15: 489-492.

Thomsen, L., 1986. Weak elastic anisotropy. Geophysics, 51: 1954-1966.

Thore, P.D., de Bazelaire, E. and Ray, M.P., 1994. A three-parameter equation: An efficient tool to enhance the stack. Geophysics, 59: 297-308.

Tieman, H.J., 1993. Description of a scanless method of stacking velocity analysis. Geophysics, 58: 1596-1606.

Tieman, H.J., 1994. Investigating the velocity-depth ambiguity of reflection traveltimes: Geophysics, 59: 1763-1773.

Trappe, H. and Bittner, R., 1989. Estimation of interval velocities within the Earth's crust. Tectonophysics, 157: 59-68.

Tsvankin, I., 1995. Normal moveout from dipping reflectors in anisotropic media. Geophysics, 60: 268-284.

Tsvankin, I., 1997. Reflection moveout and parameter estimation for horizontal transverse isotropy. Geophysics, 62: 614-629.

Tsvankin, I. and Thomsen, L., 1995. Nonhyperbolic reflection moveout in anisotropic media. Geophysics, 59: 1290-1304.

Valasek, P., Mueller, St., Frei, W. and Hollinger, K., 1991. Results of NFP seismic reflection profiling along the Alpine section of the European Geotraverse (EGT). Geophys. J. Int., 105: 85-102.

Van der Schoot, A., Romijn, R., Larson, D.E. and Berkhout, A.J., 1989. Prestack migration of shot record inversion and common depth point stacking: a case study. First Break, 7: 293-304.

Van Schmus, W.R., Bickford, M.E., Lewry, J.F. and Macdonald, R., 1987. U-Pb geochronology in the Trans-Hudson, northern Saskatchewan, Canada. Can. J. Earth Sci., 24: 407-424.

White, D.J., Lucas, S.B., Hajnal, Z., Green, A.G., Lewry, J.F., Weber, W., Bailes, A.H., Syme, E.C. and Ashton, K., 1994. Paleo-Proterozoic thick-skinned tectonics: Lithoprobe seismic reflection results from the eastern Trans-Hudson Orogen. Can. J. Earth Sci., 31: 458-469.

Wright, C., Barton, T., Goleby, B.R., Spence, A.G. and Pfister, D., 1990. The interpretation of expanding spread reflection profiles: examples from central and eastern Australia. Tectonophysics, 172: 73-82.

Yanovsky, A., Bogolubsky, A., Sorin, V. and Krilov, H., 1982. Accuracy of interval velocity calculation in structural interpretation. Applied Geophysics, 95: 20-31 (in Russian).

Yilmaz, O. and Chambers, R., 1984. Migration velocity analysis by wavefield extraplolation. Geophysics, 49: 1664-1674.

Yilmaz, O., 1989. Velocity-stack processing. Geophys. Prosp., 37: 357-382.

Zelt, C.A. and Smith, R.B., 1992. Seismic traveltime inversion for 2-D crustal velocity structures. Geophys. J. Int., 108:16-34.

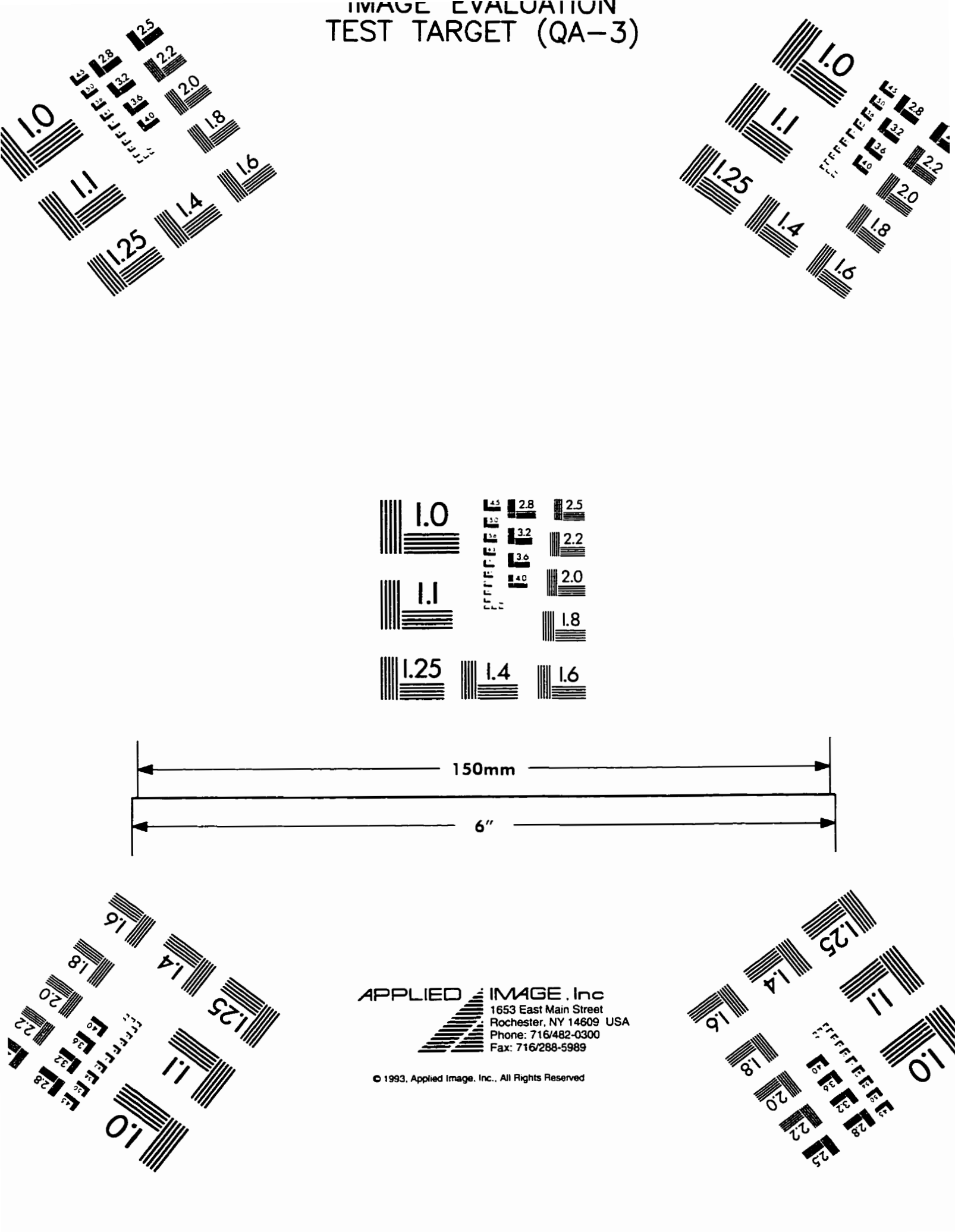
IMAGE EVALUATION
TEST TARGET (QA-3)
1.0
1.1
1.25
1.4
1.6
1.8
2.0
2.2
2.5
2.8
3.2
3.6
4.0
150mm
6"
APPLIED IMAGE, Inc
1653 East Main Street
Rochester, NY 14609 USA
Phone: 716/482-0300
Fax: 716/288-5989
© 1993, Applied Image, Inc., All Rights Reserved